$$\varepsilon_{eff} = \varepsilon_0 + 3N\varepsilon_0 \frac{\varepsilon_M - \varepsilon_0}{\varepsilon_M + 2\varepsilon_0}$$

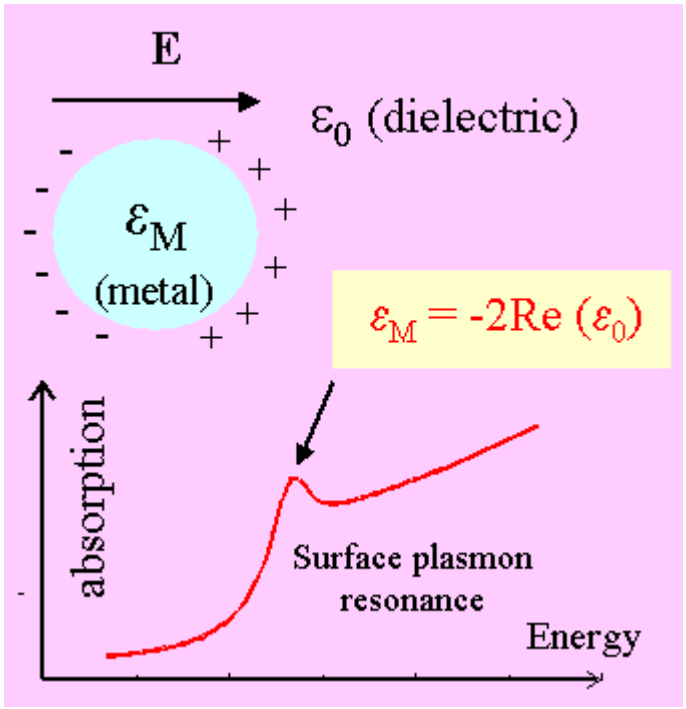

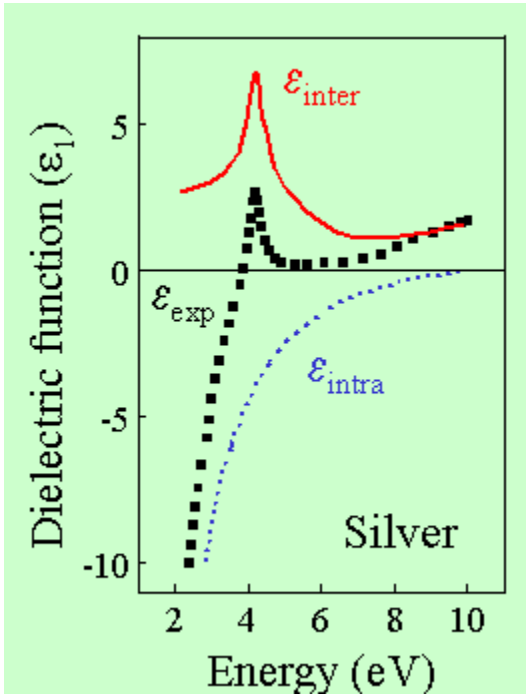

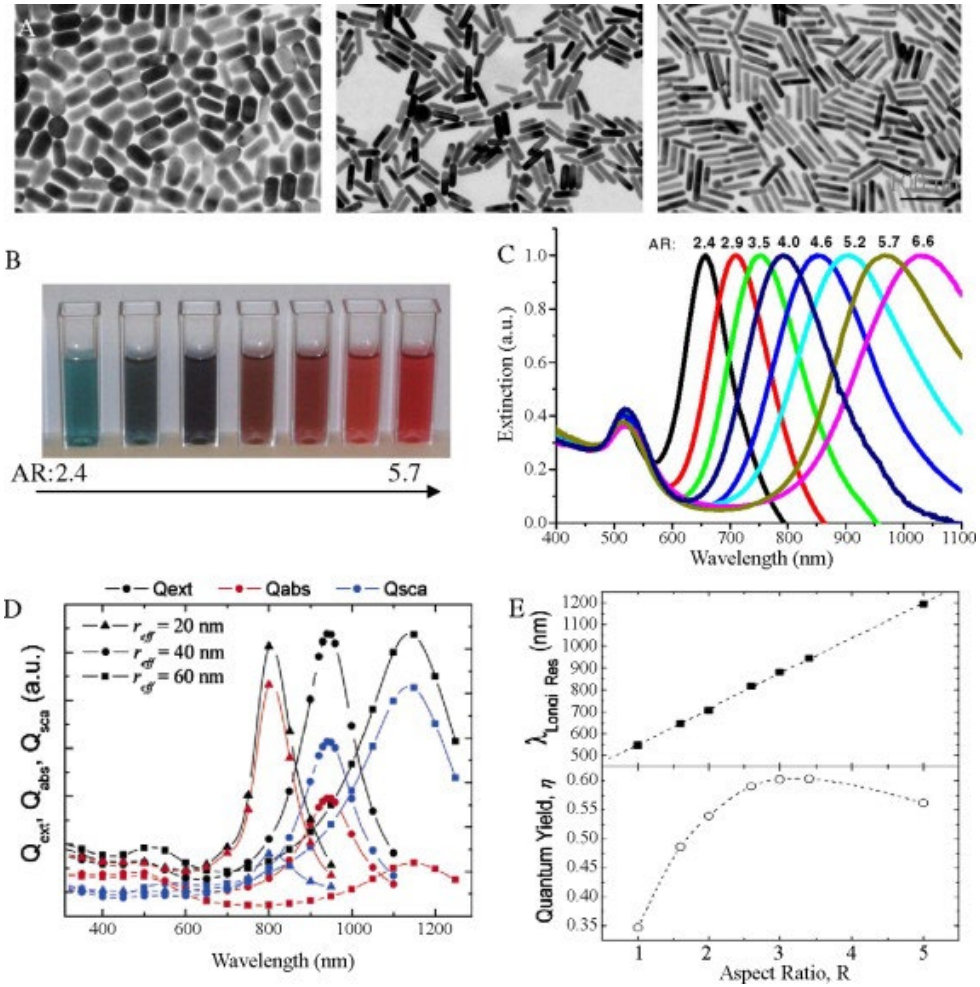
A
B
AR:2.4
5.7
C
AR: 2.4 2.9 3.5 4.0 4.6 5.2 5.7 6.6
Extinction (a.u.)
Wavelength (nm)
D
Qext
Qabs
Qsca
r_{eff} = 20 nm
r_{eff} = 40 nm
r_{eff} = 60 nm
Q_{ext}, Q_{abs}, Q_{sca} (a.u.)
Wavelength (nm)
E
$\lambda_{Longi\ Res}$ (nm)
Quantum Yield, η
Aspect Ratio, R

Synthesis of Quantum Dots

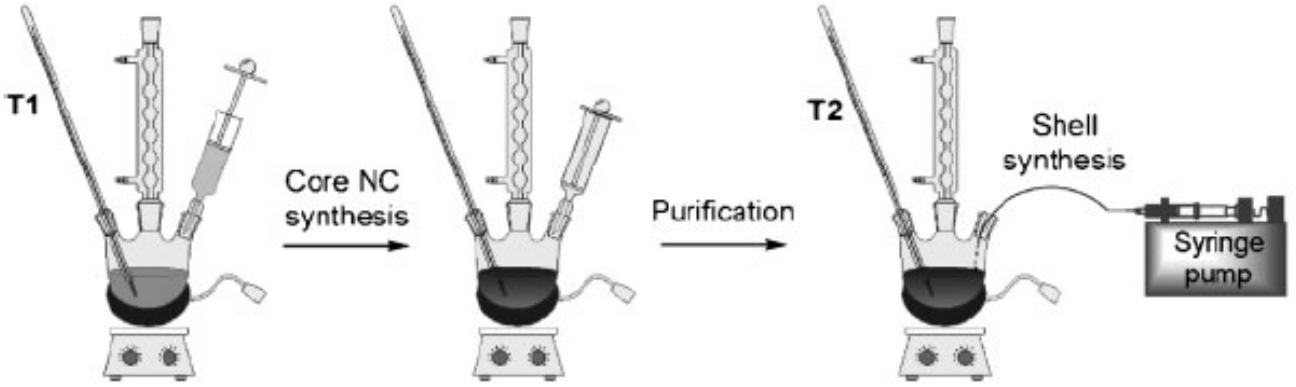

Figure 2. Two–step synthesis of core/shell nanocrystals.

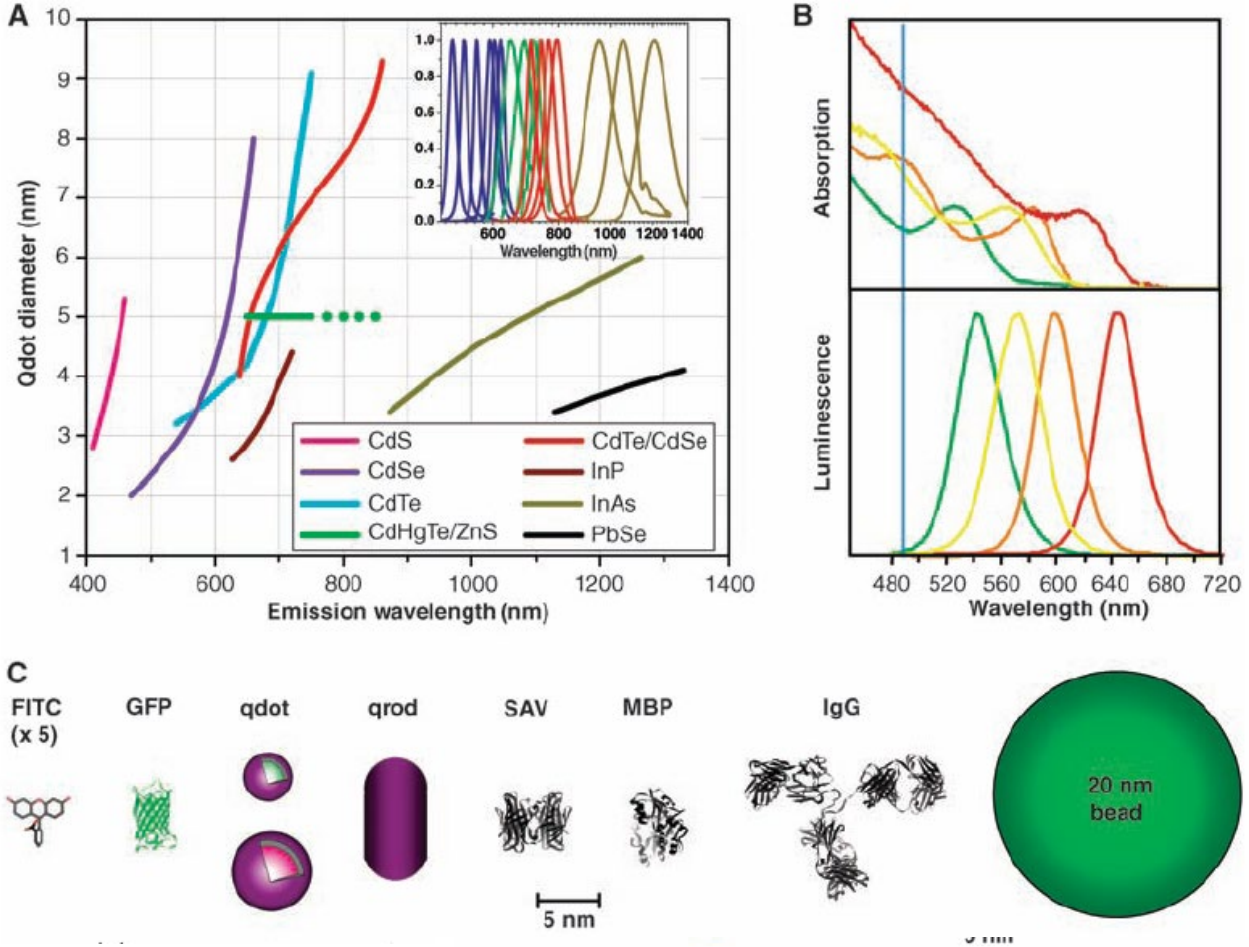

Fig. 1. (**A**) Emission maxima and sizes of quantum dots of different composition. Quantum dots can be synthesized from various types of semiconductor materials (II-VI: CdS, CdSe, CdTe…; III-V: InP, InAs…; IV-VI: PbSe…) characterized by different bulk band gap energies. The curves represent experimental data from the literature on the dependence of peak emission wavelength on qdot diameter. The range of emission wavelength is 400 to 1350 nm, with size varying from 2 to 9.5 nm (organic passivation/solubilization layer not included). All spectra are typically around 30 to 50 nm (full width at half maximum). Inset: Representative emission spectra for some materials. Data are from (*12*, *18*, *27*, *76*–*82*). Data for CdHgTe/ZnS have been extrapolated to the maximum emission wavelength obtained in our group. (**B**) Absorption (upper curves) and emission (lower curves) spectra of four CdSe/ZnS qdot samples. The blue vertical line indicates the 488-nm line of an argon-ion laser, which can be used to efficiently excite all four types of qdots simultaneously. [Adapted from (*28*)] (**C**) Size comparison of qdots and comparable objects. FITC, fluorescein isothiocyanate; GFP, green fluorescent protein; qdot, green (4 nm, top) and red (6.5 nm, bottom) CdSe/ZnS qdot; qrod, rod-shaped qdot (size from Quantum Dot Corp.'s Web site). Three proteins—streptavidin (SAV), maltose binding protein (MBP), and immunoglobulin G (IgG)—have been used for further functionalization of qdots (see text) and add to the final size of the qdot, in conjunction with the solubilization chemistry (Fig. 2).

Scheme 1. Modular Design of Hydrophilic Ligands with Terminal Functional Groups Used in This Study

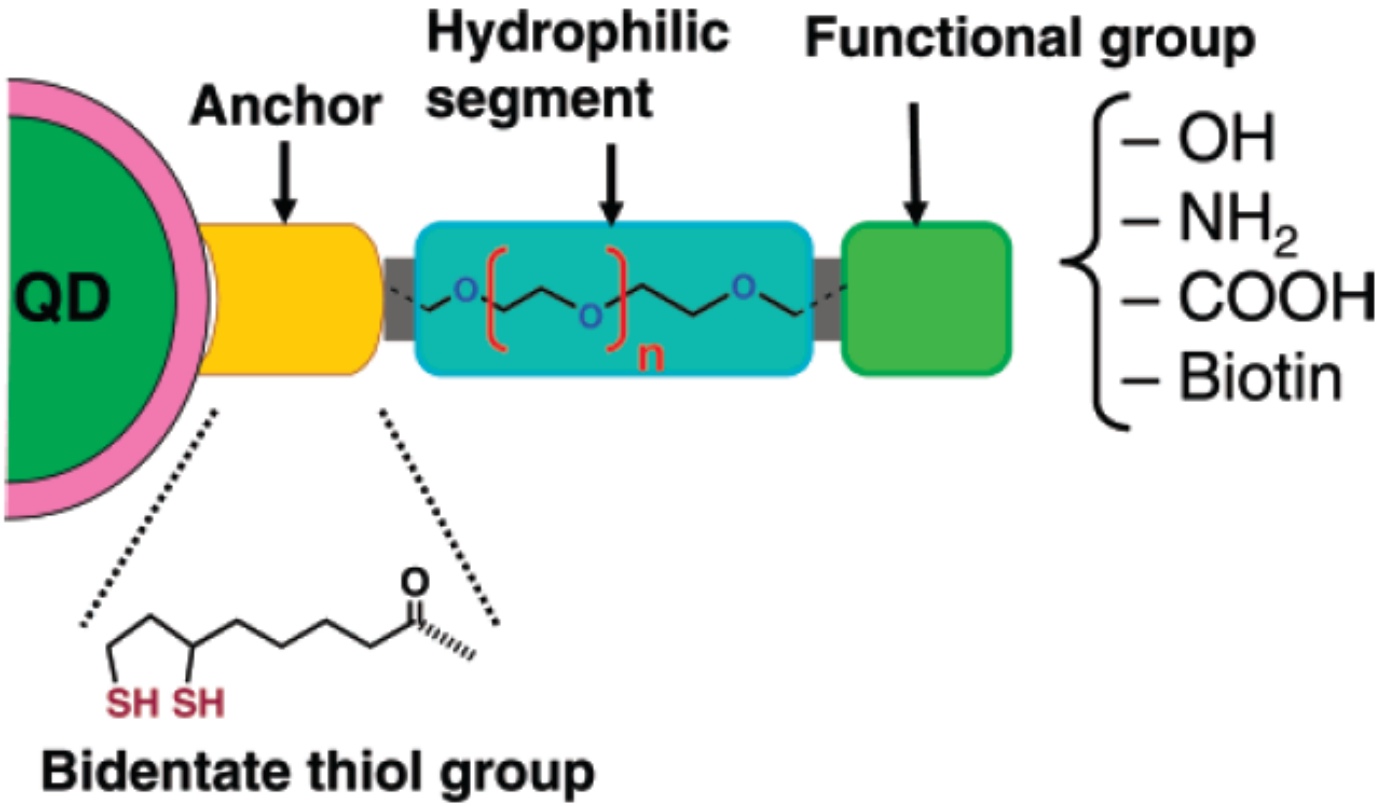

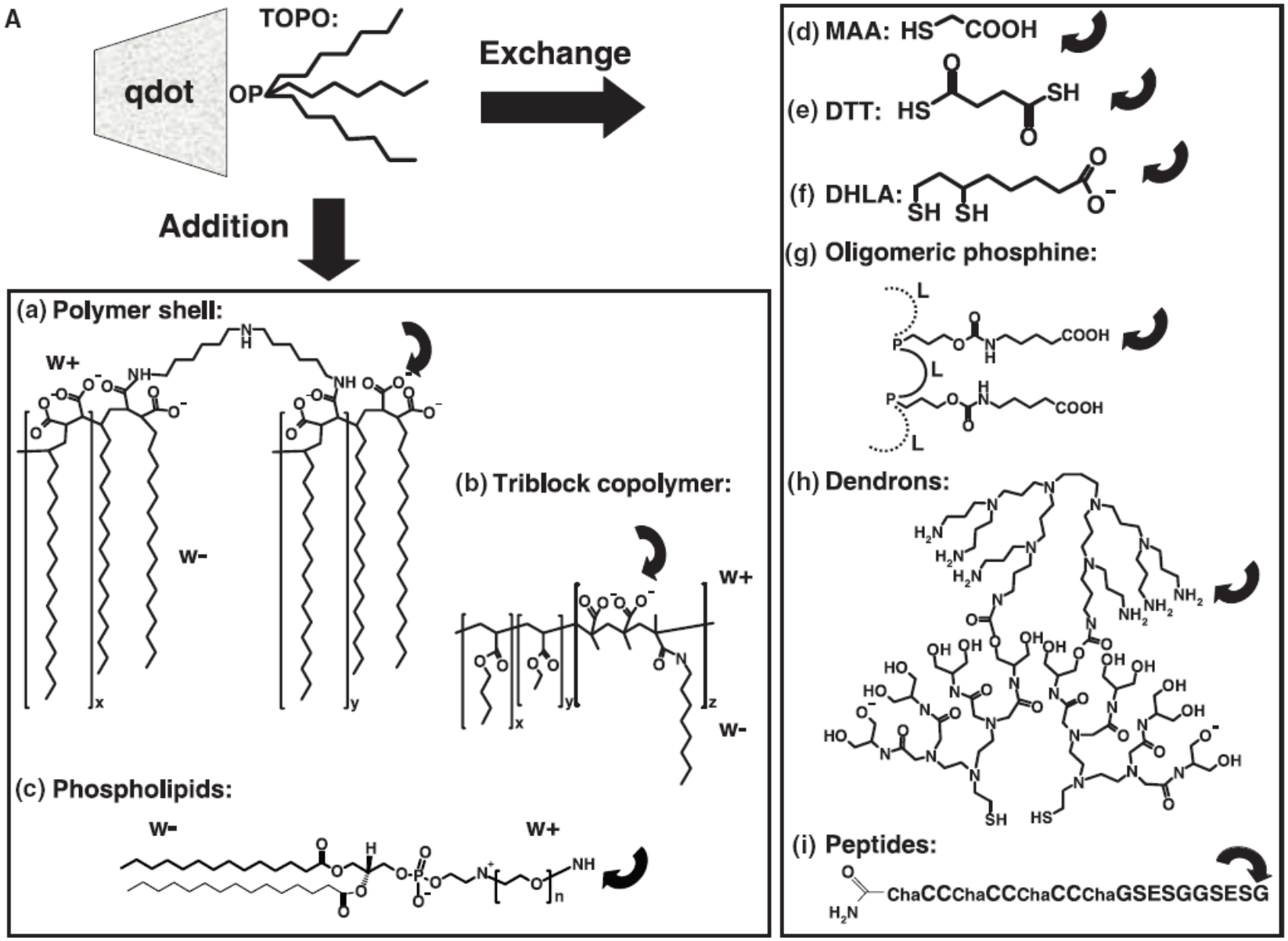
A
qdot
TOPO:
OP
Exchange
Addition
(a) Polymer shell:
W+
W-
(b) Triblock copolymer:
W+
W-
(c) Phospholipids:
W-
W+
(d) MAA: HS COOH
(e) DTT: HS SH
(f) DHLA: SH SH
(g) Oligomeric phosphine:
L
COOH
(h) Dendrons:
(i) Peptides:
ChaCCChaCCChaCCChaGSESGGSESG

Nanomaterials for Biodiagnostic

- Nucleic Acid
  - Genetic information for identification
  - Diseases, bacterium, virus, pathogen
  - PCR with molecular fluorophore, State of the Art
  - Expansive, Non-portable, Non-multiplexing
- Proteins
  - Cancers and diseases, unusual high concentration of marker
  - ELISA (~pM) with molecular fluorophore
  - No PCR version

Colorimetric Detection of DNA

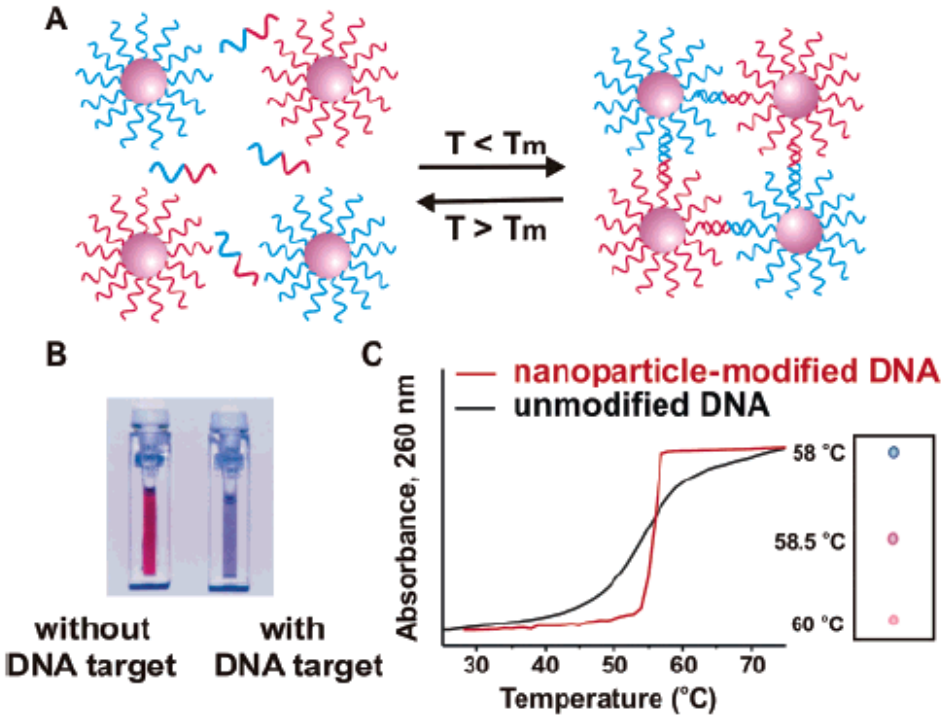

Figure 2. In the presence of complementary target DNA, oligonucleotide-functionalized gold nanoparticles will aggregate (A), resulting in a change of solution color from red to blue (B). The aggregation process can be monitored using UV−vis spectroscopy or simply by spotting the solution on a silica support (C). (Reprinted with permission from *Science* (http://www.aaas.org), ref 29. Copyright 1997 American Association for the Advancement of Science.)

A DNA-based method for rationally assembling nanoparticles into macroscopic materials

Chad A. Mirkin, Robert L. Letsinger, Robert C. Mucic & James J. Storhoff

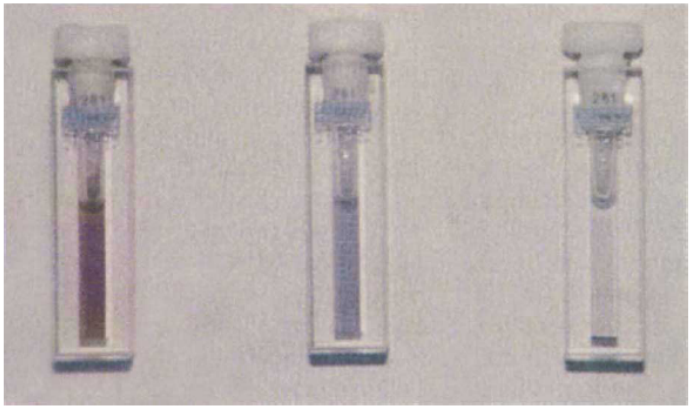

FIG. 2 Cuvettes with the Au colloids and the four DNA strands responsible for the assembly process. Left cuvette, at 80 °C with DNA-modified colloids in the unhybridized state; centre, after cooling to room temperature but before the precipitate settles; and right, after the polymeric precipitate settles to the bottom of the cuvette. Heating either of these cool solutions results in the reformation of the DNA-modified colloids in the unhybridized state (shown in the left cuvette).

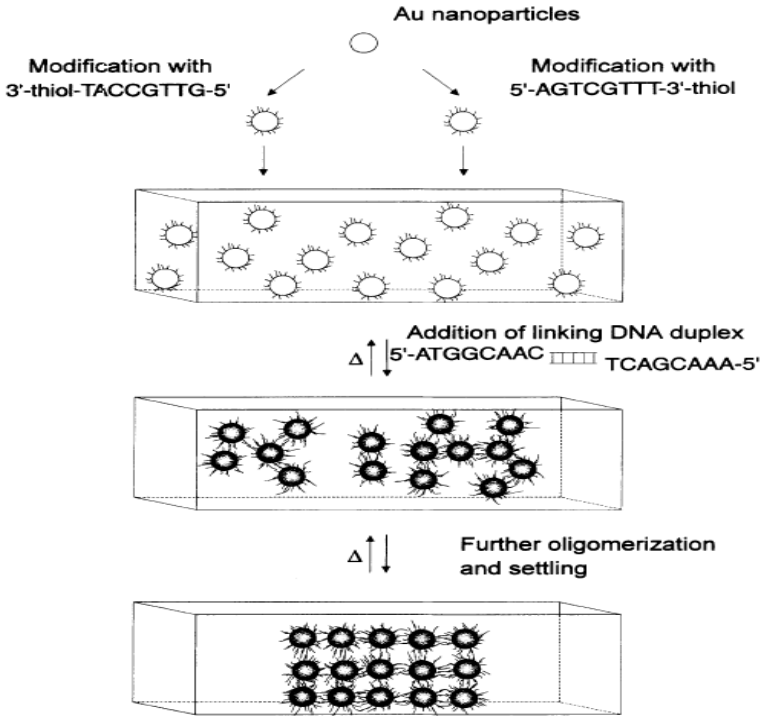

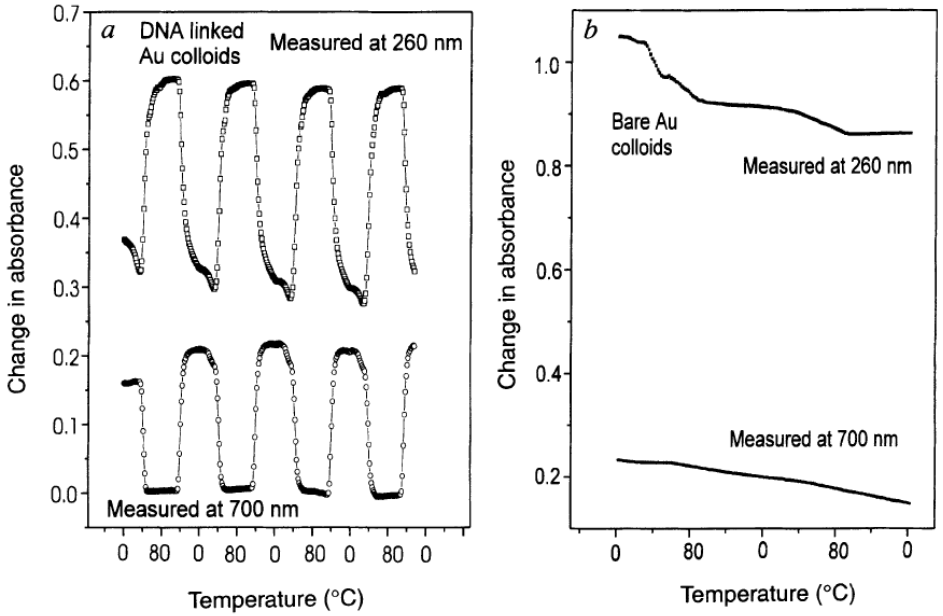

Nature, 1996, 382, 607

Selective Colorimetric Detection of Polynucleotides Based on the Distance-Dependent Optical Properties of Gold Nanoparticles

Robert Elghanian, James J. Storhoff, Robert C. Mucic,
Robert L. Letsinger,* Chad A. Mirkin*

SCIENCE • VOL. 277 • 22 AUGUST 1997

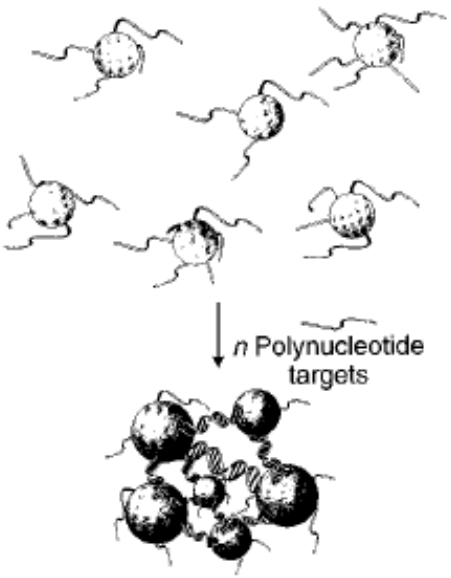

Fig. 1. Schematic representation of the concept for generating aggregates signaling hybridization of nanoparticle-oligonucleotide conjugates with oligonucleotide target molecules. The nanoparticles and the oligonucleotide interconnects are not drawn to scale, and the number of oligomers per particle is believed to be much larger than depicted.

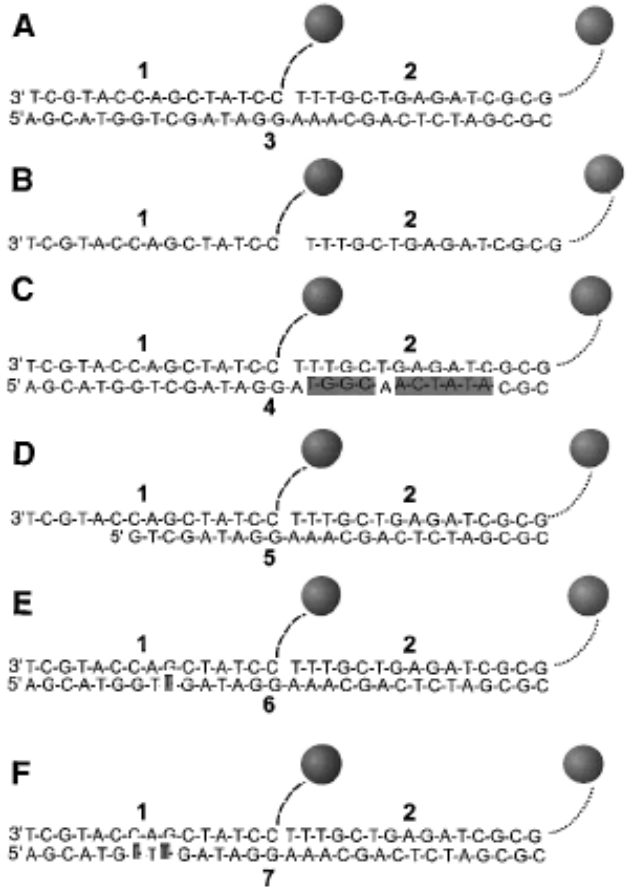

Fig. 2. Mercaptoalkyloligonucleotide-modified 13-nm Au particles and polynucleotide targets used for examining the selectivity of the nanoparticle-based colorimetric polynucleotide detection system. (**A**) Complementary target; (**B**) probes without the target; (**C**) a half-complementary target; (**D**) a 6-bp deletion; (**E**) a 1-bp mismatch; and (**F**) a 2-bp mismatch. For the sake of clarity, only two particles are shown; in reality a polymeric aggregate with many particles is formed. Dashed lines represent flexible spacer portions of the mercaptoalkyloligonucleotide strands bound to the nanoparticles; note that these spacers, because of their noncomplementary nature, do not participate in hybridization. The full sequences for the two probes, **1** and **2**, which bind to targets **3** through **7**, are

1-5′SH-$(CH_2)_6$- [CTA-ATC-CGC-ACA-G]
spacer

[CC-TAT-CGA-CCA-TGC-T]
probe

2-5′SH-$(CH_2)_6$-[ATG-GCA-ACT-ATA-C]
spacer

[GC-GCT-AGA-GTC-GTT-T]
probe

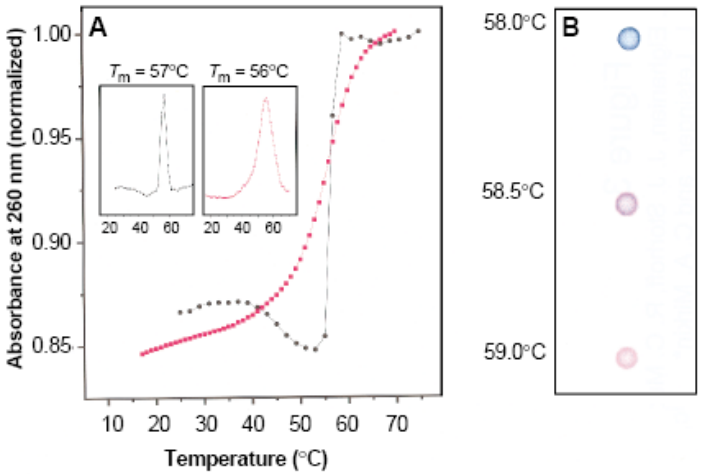

Fig. 3. (**A**) Comparison of the thermal dissociation curves for complexes of mercaptoalkyloligonucleotide-modified Au nanoparticles (black circles) and mercaptoalkyloligonucleotides without Au nanoparticles (red squares) with the complementary target, **3**, in hybridization buffer (0.1 M NaCl, 10 mM phosphate buffer, pH 7.0). For the first set (black circles), a mixture of 150 μl of each colloid conjugate and 3 μl of the target oligonucleotide in hybridization buffer (0.1 M NaCl, 10 mM phosphate, pH 7.0) was frozen at the temperature of dry ice, kept for 5 min, thawed over a period of 15 min, and diluted to 1.0 ml with buffer (final target concentration, 0.02 μM). The absorbance was measured at 1-min intervals with a temperature increase of 1°C per minute. The increase in absorption at 260 nm (A_{260}) was ~0.3 absorption units (AU). In the absence of the oligonucleotide targets, the absorbance of the nanoparticles did not increase with increasing temperature. For the second set, the mercaptoalkyloligonucleotides and complementary target (each 0.33 μM) were equilibrated at room temperature in 1 ml of buffer, and the changes in absorbance with temperature were monitored as before. The increase in A_{260} was 0.08 AU. (**Insets**) Derivative curves for each set (*15*). (**B**) Spot test showing T_c (thermal transition associated with the color change) for the Au nanoparticle probes hybridized with complementary target. A solution prepared from 150 μl of each probe and 3 μl of the target (0.06 μM final target concentration) was frozen for 5 min, allowed to thaw for 10 min, transferred to a 1-ml cuvette, and warmed at 58°C for 5 min in the thermally regulated cuvette chamber of the spectrophotometer. Samples (3 μl) were transferred to a C_{18} reverse phase plate with an Eppendorf pipette as the temperature of the solution was increased incrementally 0.5°C at 5-min intervals.

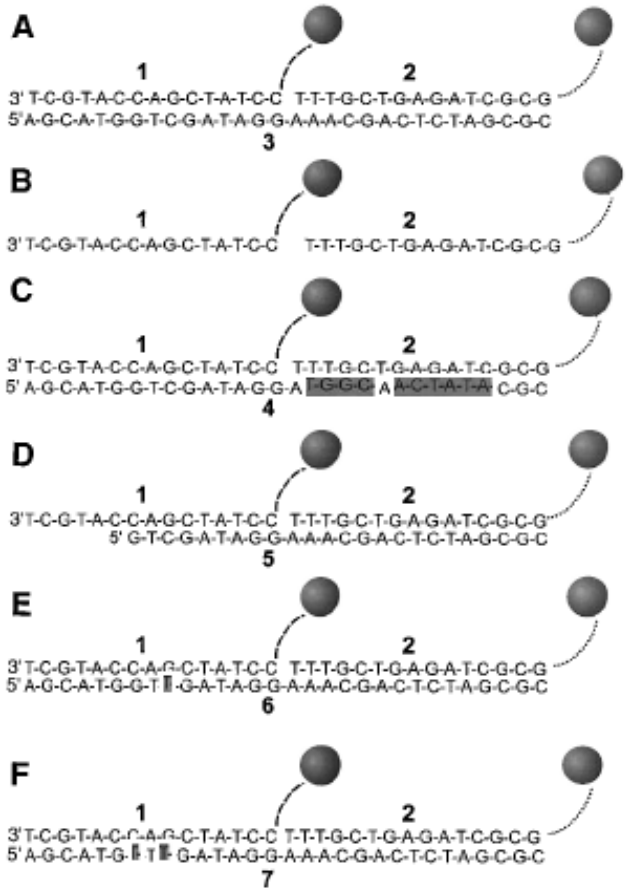

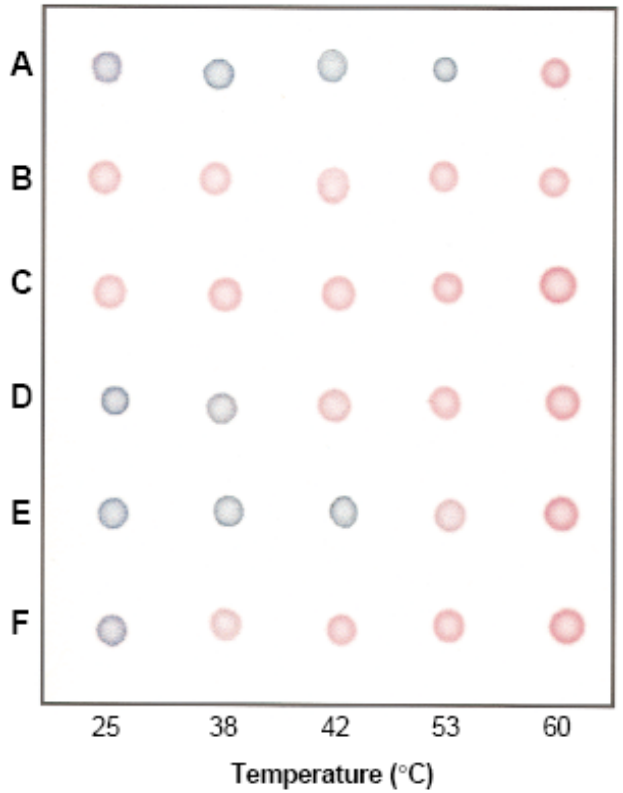

Fig. 4. Selective polynucleotide detection for the target probes shown in Fig. 2: (**A**) complementary target; (**B**) no target; (**C**) complementary to one probe; (**D**) a 6-bp deletion; (**E**) a 1-bp mismatch; and (**F**) a 2-bp mismatch. Nanoparticle aggregates were prepared in a 600-μl thin-walled Eppendorf tube by addition of 1 μl of a 6.6 μM oligonucleotide target to a mixture containing 50 μl of each probe (0.06 μM final target concentration). The mixture was frozen (5 min) in a bath of dry ice and isopropyl alcohol and allowed to warm to room temperature. Samples were then transferred to a temperature-controlled water bath, and 3-μl aliquots were removed at the indicated temperatures and spotted on a C_{18} reverse phase plate.

J. Am. Chem. Soc. **2000,** *122,* 9071−9077

Colloidal Au-Enhanced Surface Plasmon Resonance for Ultrasensitive Detection of DNA Hybridization

Lin He, Michael D. Musick, Sheila R. Nicewarner, Frank G. Salinas, Stephen J. Benkovic, Michael J. Natan, and Christine D. Keating*

Scheme 1. SPR Surface Assembly

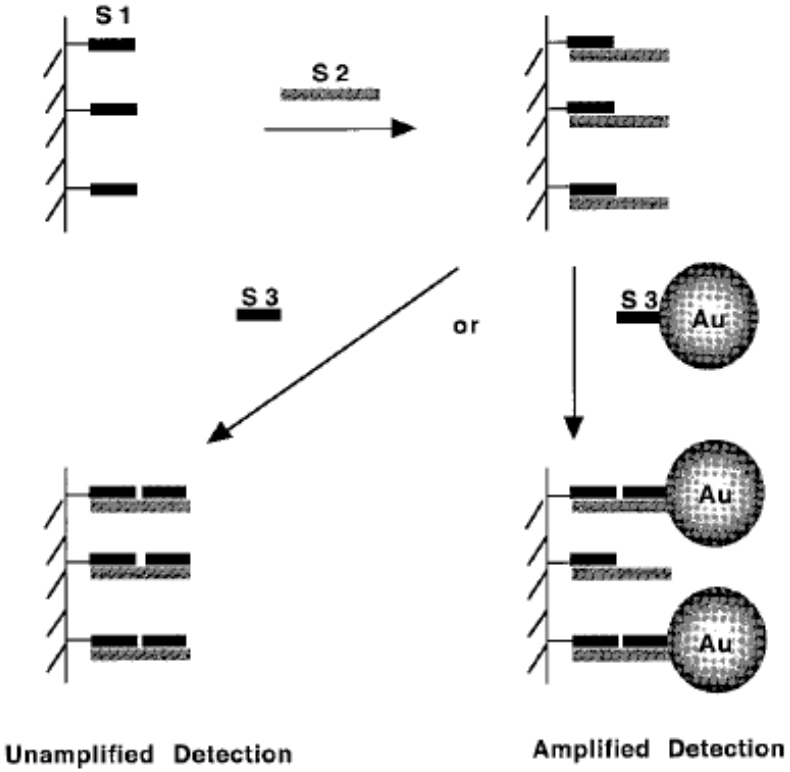

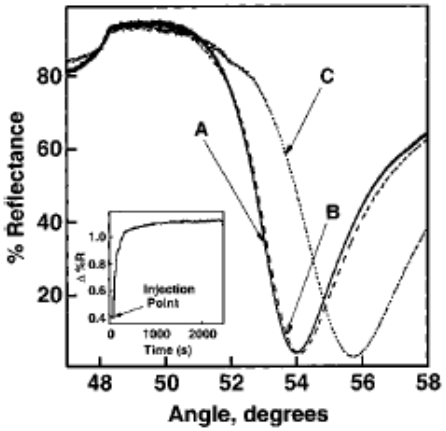

Figure 1. SPR curves of surfaces prepared in sequential steps as illustrated in Scheme 1: a MHA-coated Au film modified with a 12-mer oligonucleotide S1(A), after hybridization with its complementary 24-mer target S2 (B), and followed by introduction of S3:Au conjugate (C) to the surface. Inset: surface plasmon reflectance changes at 53.2° for the oligonucleotide-coated Au film measured during a 60-min exposure to S3:Au conjugates.

Scheme 2. SPR Surface Assembly in the Digestion Experiment

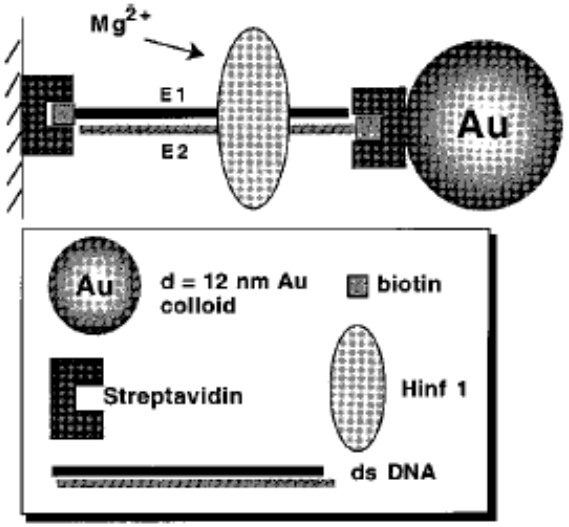

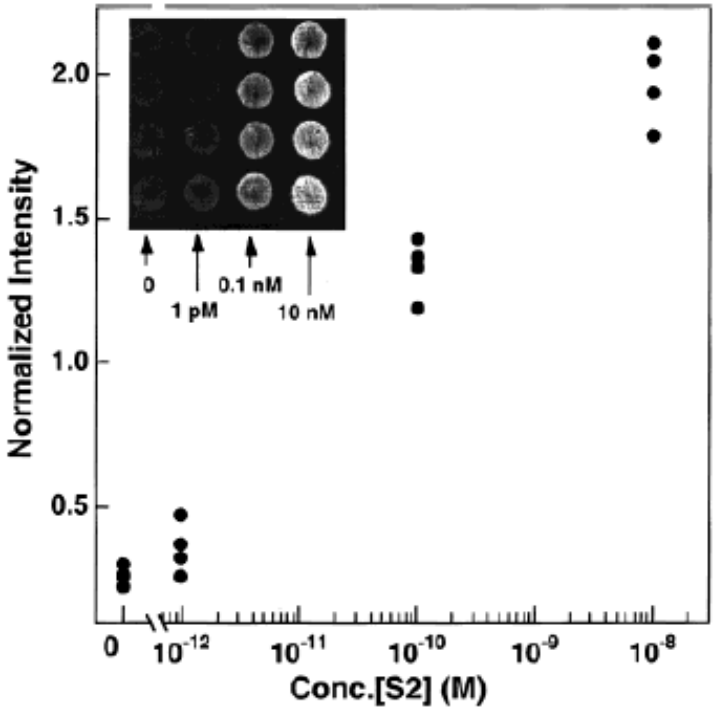

Figure 5. Plot of normalized intensity of SPR reflectance as a function of logarithmic concentration of the analyte 24-mer oligo (S2). Each spot represents one data point at the corresponding concentration. CCD parameters: exposure time = 0.3 s, 16 bit resolution, spot size = 4.5 mm in diameter. Inset: a 2-D SPR image of a Au surface derivatized with 20 μL of buffer blank, 1 pM, 0.1 nM, and 10 nM S2 oligos (from left to right, respectively).

Self-Assembled Nanoparticle Probes for Recognition and Detection of Biomolecules

Dustin J. Maxwell, Jason R. Taylor, and Shuming Nie*,†

9606 ■ J. AM. CHEM. SOC. 2002, *124*, 9606−9612

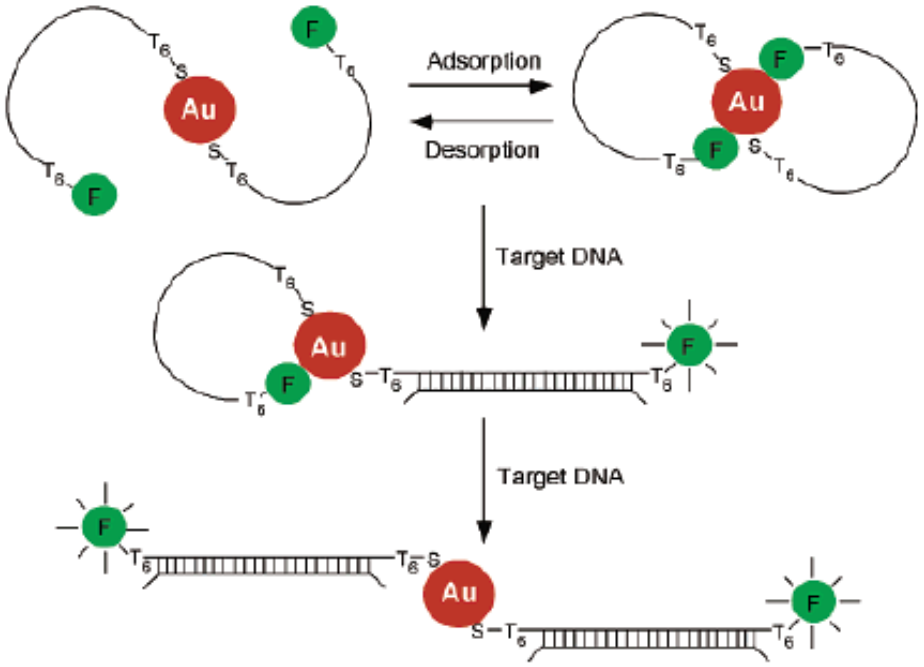

Figure 1. Nanoparticle-based probes and their operating principles. Two oligonucleotide molecules (oligos) are shown to self-assemble into a constrained conformation on each gold particle (2.5 nm diameter). A T_6 spacer (six thymines) is inserted at both the 3′- and 5′-ends to reduce steric hindrance. Single-stranded DNA is represented by a single line and double-stranded DNA by a cross-linked double line. In the assembled (closed) state, the fluorophore is quenched by the nanoparticle. Upon target binding, the constrained conformation opens, the fluorophore leaves the surface because of the structural rigidity of the hybridized DNA (double-stranded), and fluorescence is restored. In the open state, the fluorophore is separated from the particle surface by about 10 nm. See text for detailed explanation. Au, gold particle; F, fluorophore; S, sulfur atom.

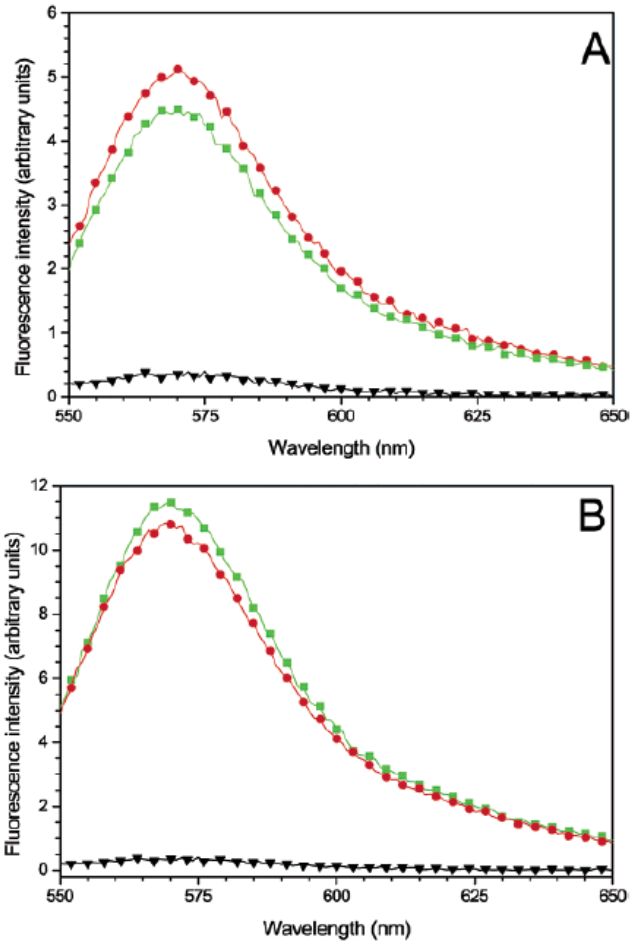

Figure 5. Fluorescence responses and the lack of sequence recognition abilities observed for nonthiolated nanoparticle probes. (A) Fluorescence spectra of nonthiolated probes generated by a complementary target (red curve), a noncomplementary target (green curve), and no target (black curve). These probes are considered nonfunctional because they do not recognize specific DNA sequences. (B) Fluorescence signals obtained from the supernatant solution when the probes were treated with a complementary target (red curve) or a noncomplementary target (green curve). The result revealed that the oligos were released into solution by nonspecific adsorption of the target on the particle surface. With a thiol group, this release was not observed (little or no signal in solution, black curve in B). The nonfunctional probes were prepared in the same way as the functional probes, except that the 3′-end thiol group was deleted. The intensity differences for the red and green curves were within experimental errors and had no particular significance.

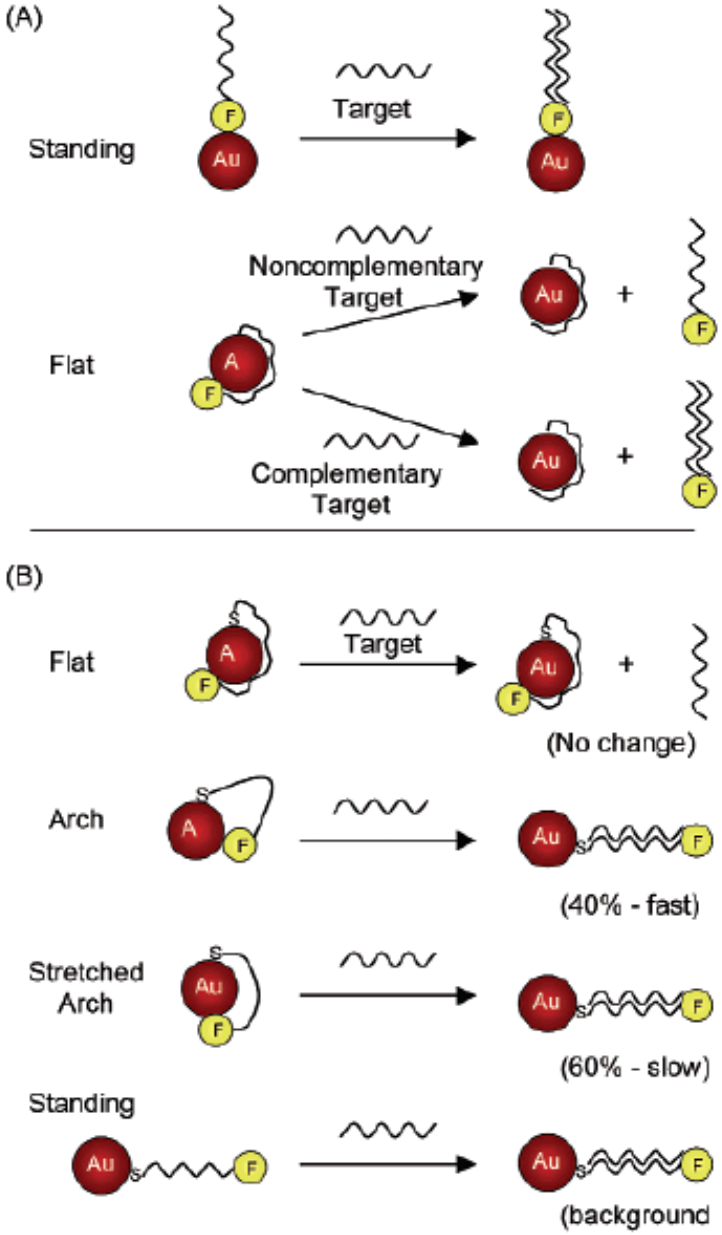

Figure 6. Schematic illustration of possible configurations for (a) nonthiolated and (b) thiolated oligonucleotides adsorbed on colloidal gold nanocrystals. Detailed discussion in text.

Scanometric DNA Array Detection with Nanoparticle Probes

SCIENCE VOL 289 8 SEPTEMBER 2000

T. Andrew Taton,[1,2] Chad A. Mirkin,[1,2]* Robert L. Letsinger[1]*

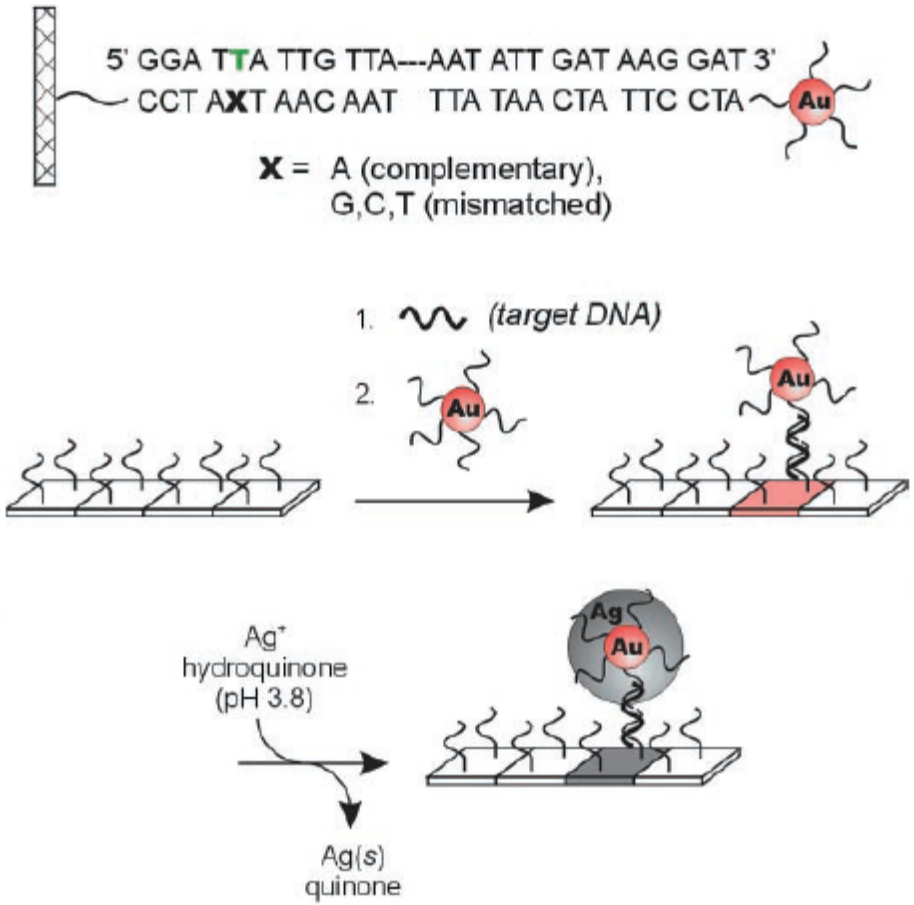

50 fM => 0.2 fM

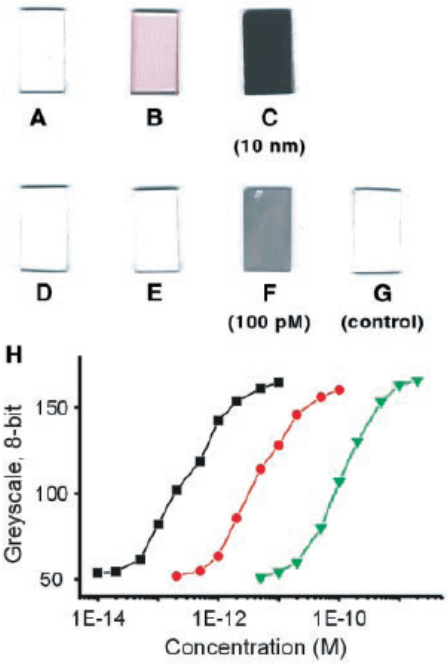

Fig. 1. Images of 7 mm by 13 mm, oligonucleotide-functionalized, float glass slides, obtained with a flatbed scanner. (**A**) Slide before hybridization of target and nanoparticle probe. (**B**) A slide identical to (A) after hybridization with oligonucleotide target (10 nM) and then nanoparticle probes (5 nM in particles). The pink color derives from the Au nanoparticle probes. (**C**) A slide identical to (B) after exposure to silver amplification solution for 5 min. (**D**) Slide before hybridization of target and nanoparticle probe. (**E**) A slide identical to (D) after hybridization with target (100 pM) and then nanoparticle probe (5 nM). The extinction of the submonolayer of nanoparticles is too low to be observed visually or with a flatbed scanner. (**F**) A slide identical to (E) after exposure to silver amplification solution for 5 min. Slide (F) is lighter than slide (C), indicating a lower concentration of target. (**G**) A control slide exposed to 5 nM nanoparticle probe and then exposed to silver amplification solution for 5 min. No darkening of the slide is observed. (**H**) Graph of 8-bit gray scale values as a function of target concentration. The gray scale values were taken from flatbed scanner images of oligonucleotide-functionalized glass surfaces that had been exposed to varying concentrations of oligonucleotide target, labeled with 5 nM oligonucleotide probe and immersed in silver amplification solution. For any given amplification time, the grayscale range is limited by surface saturation at high grayscale values and the sensitivity of the scanner at low values. Therefore, the dynamic range of this system can be adjusted by means of hybridization and amplification conditions (that is, lower target concentrations require longer amplification periods). Squares: 18-base capture-target overlap (*5*), 8× PBS hybridization buffer [1.2 M NaCl and 10 mM NaH_2PO_4/Na_2HPO_4 buffer (pH 7)], 15 min amplification time. Circles: 12-base capture-target overlap, 8× PBS hybridization buffer, 10 min amplification time. Triangles: 12-base capture-target overlap, 2× PBS hybridization buffer [0.3 M NaCl, 10 mM NaH_2PO_4/Na_2HPO_4 buffer (pH 7)], 5 min amplification time. The lowest target concentration that can be effectively distinguished from the background baseline is 50 fM.

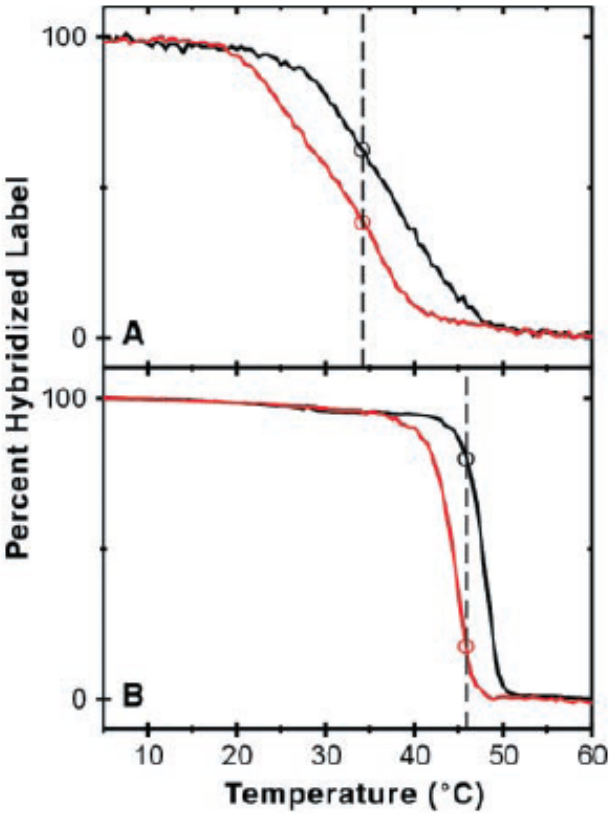

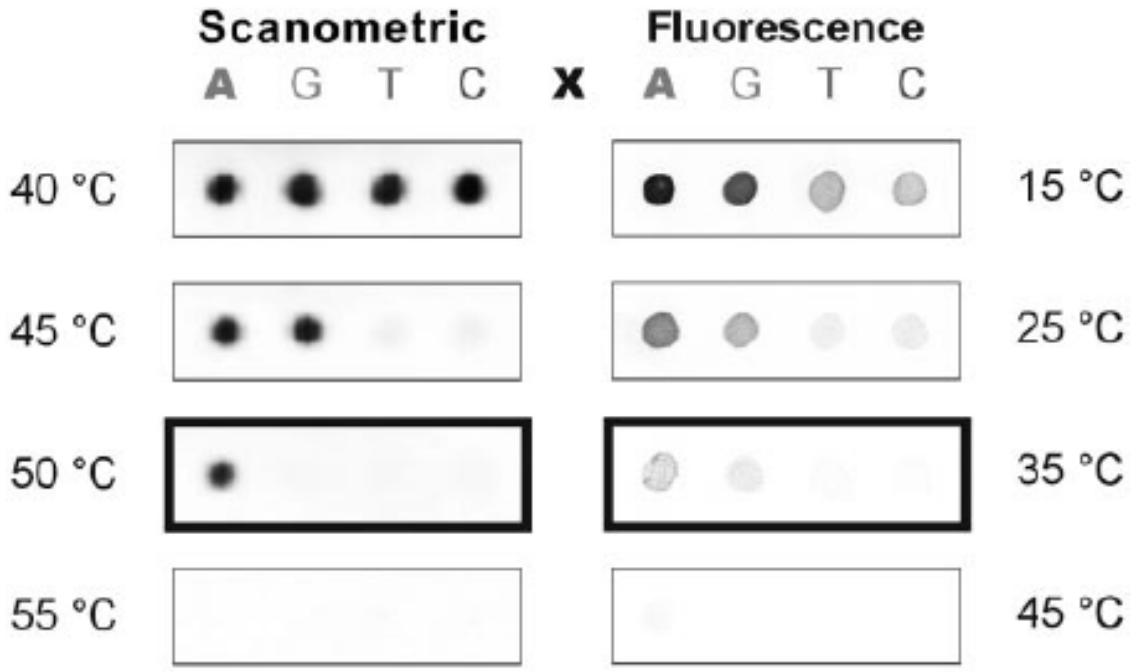

Fig. 3. (**Left**) Nanoparticle-labeled arrays developed at different stringency temperatures. Model oligonucleotide arrays (with the capture sequences shown in Scheme 1) were treated with oligonucleotide target and nanoparticle probes, followed by a 2-min buffer wash at the temperatures shown and subsequent silver amplification (*13*). Images were obtained with an Epson Expression 636 (600 dots per inch) flatbed scanner (Epson America, Long Beach, California). The darkened border indicates the array that showed optimum selectivity for the perfectly complementary target; at this temperature, the ratio of background-subtracted, 8-bit gray scale values for elements A:G:T:C, obtained from histogram averages in Adobe Photoshop (Adobe Systems, San Jose, California), is 96:9:7:6. (**Right**) Fluorophore-labeled arrays washed at different stringency temperatures. Model oligonucleotide arrays identical to those shown at left were treated with oligonucleotide target and Cy3-labeled oligonucleotide probes, followed by a 2-min buffer wash at the temperatures shown. Images were obtained with a ScanArray Confocal Microarray Scanner (GSI Lumonics, Billerica, Massachusetts). The darkened border indicates the array that showed the highest selectivity for the perfectly complementary target, as calculated by the QuantArray Analysis software package (GSI Lumonics); at this temperature, the intensity ratio (in percent, with the intensity of the X = A element at 15°C set to 100%) for elements A:G:T:C is 18:7:1:1.

Nanoparticles with Raman Spectroscopic Fingerprints for DNA and RNA Detection

YunWei Charles Cao, Rongchao Jin, Chad A. Mirkin*

30 AUGUST 2002 VOL 297 SCIENCE

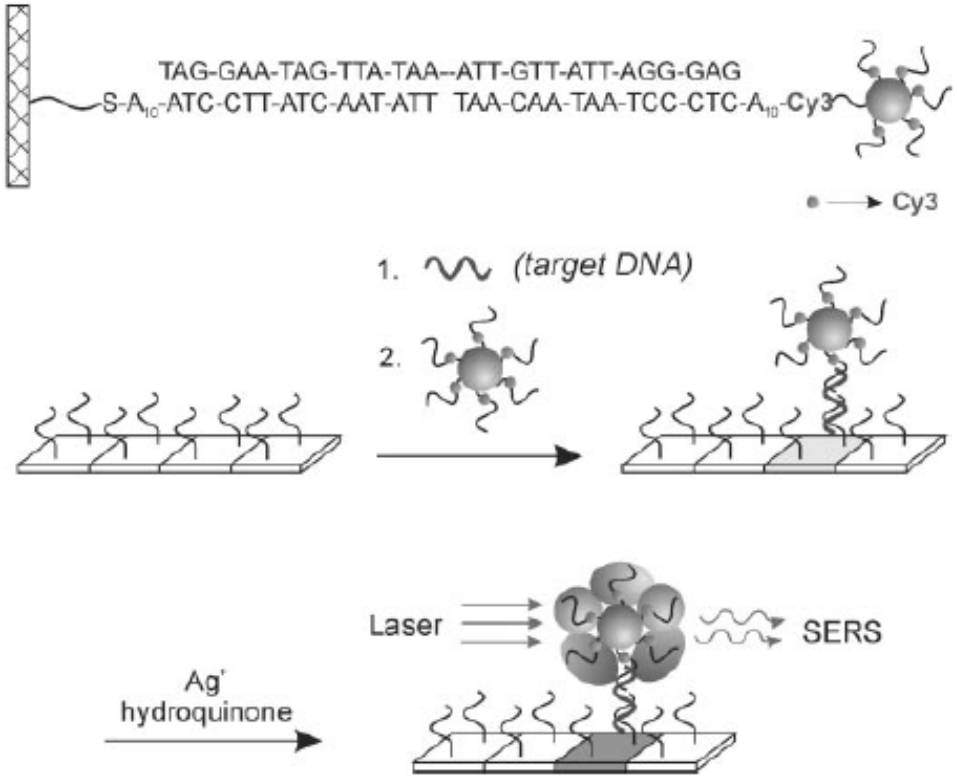

1 fM

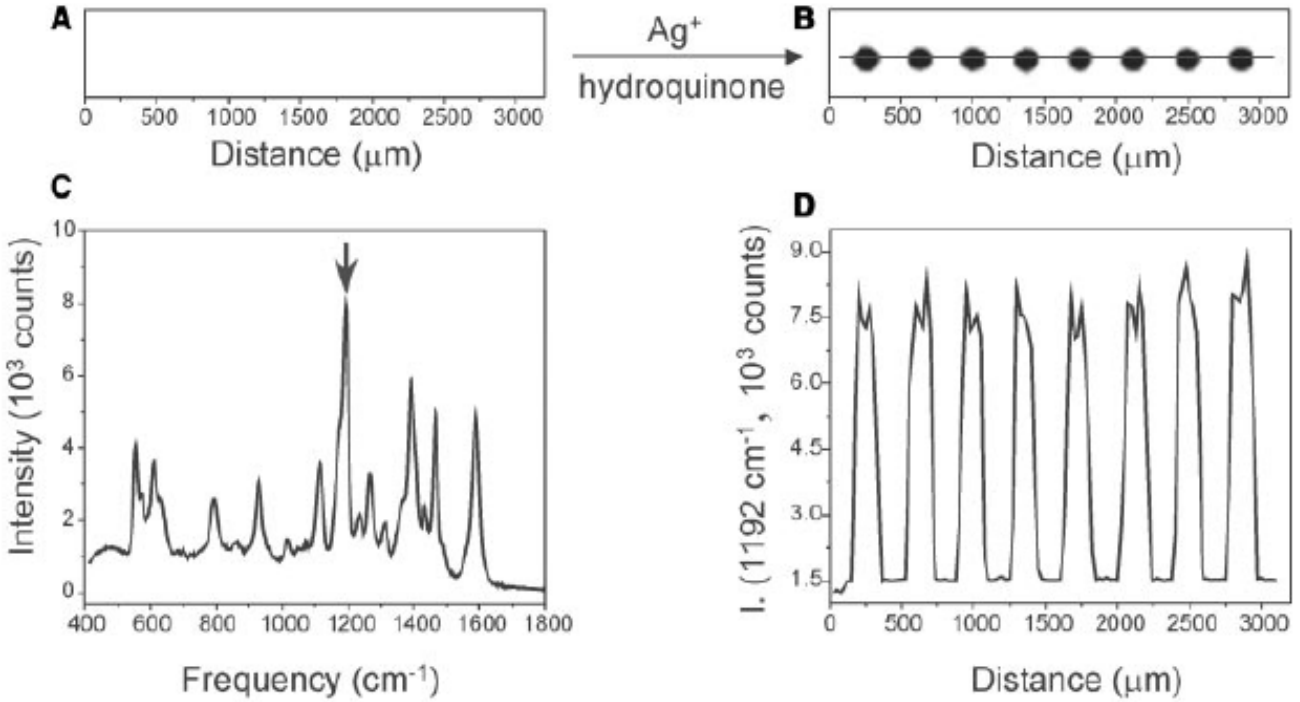

Fig. 1. Flatbed scanner images of microarrays hybridized with nanoparticles (**A**) before and (**B**) after Ag enhancing. (**C**) A typical Raman spectrum acquired from one of the Ag spots. (**D**) A profile of Raman intensity at 1192 cm^{-1} as a function of position on the chip; the laser beam from the Raman instrument is moved over the chip from left to right as defined by the line in (B).

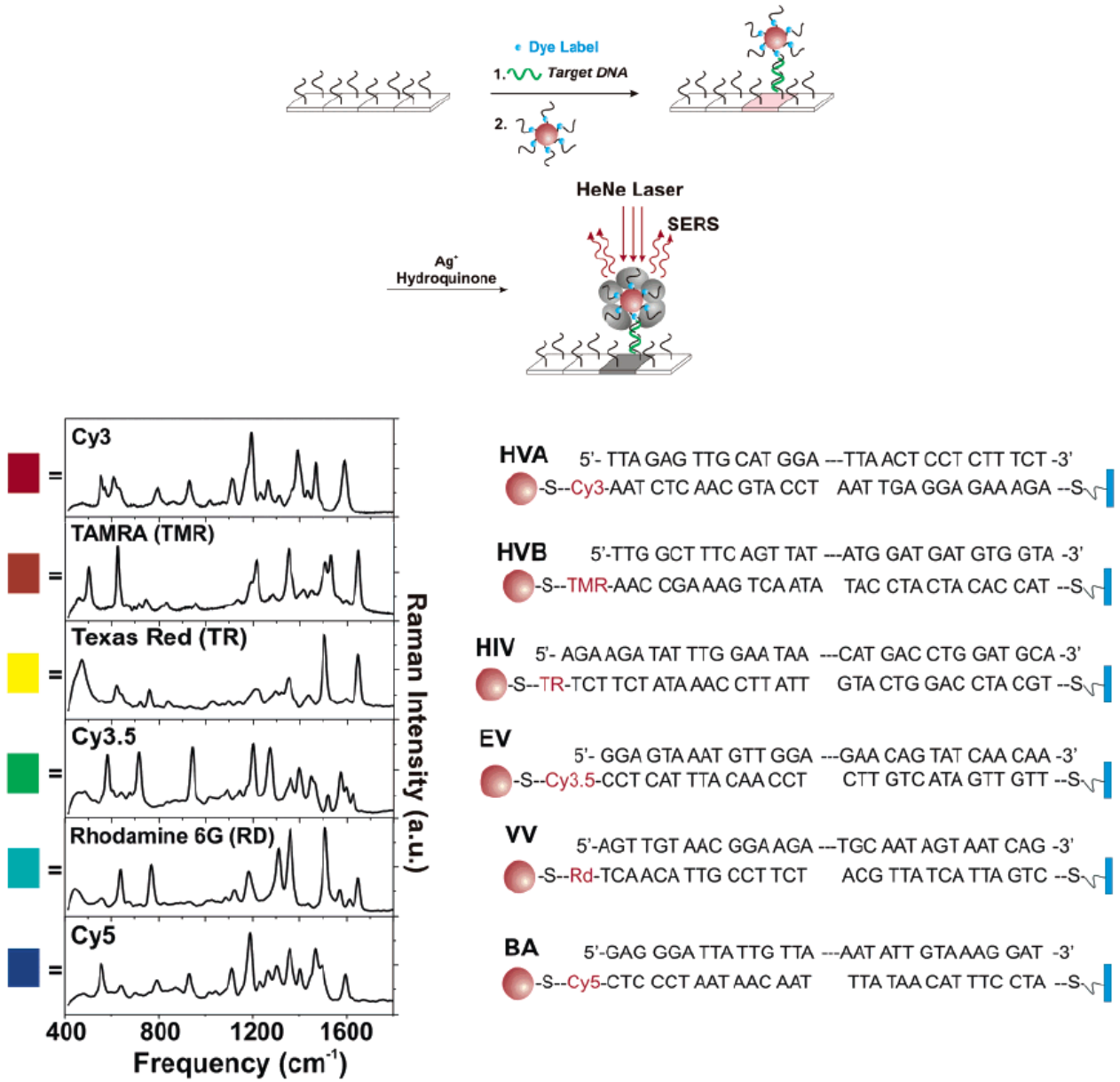

Figure 5. If Raman dyes (blue spheres) are attached to the labeling probe in the scanometric assay, the targets can be encoded and detected via the Raman signal of their labels. (Reprinted with permission from *Science* (http://www.aaas.org), ref 68. Copyright 2002 American Association for the Advancement of Science.)

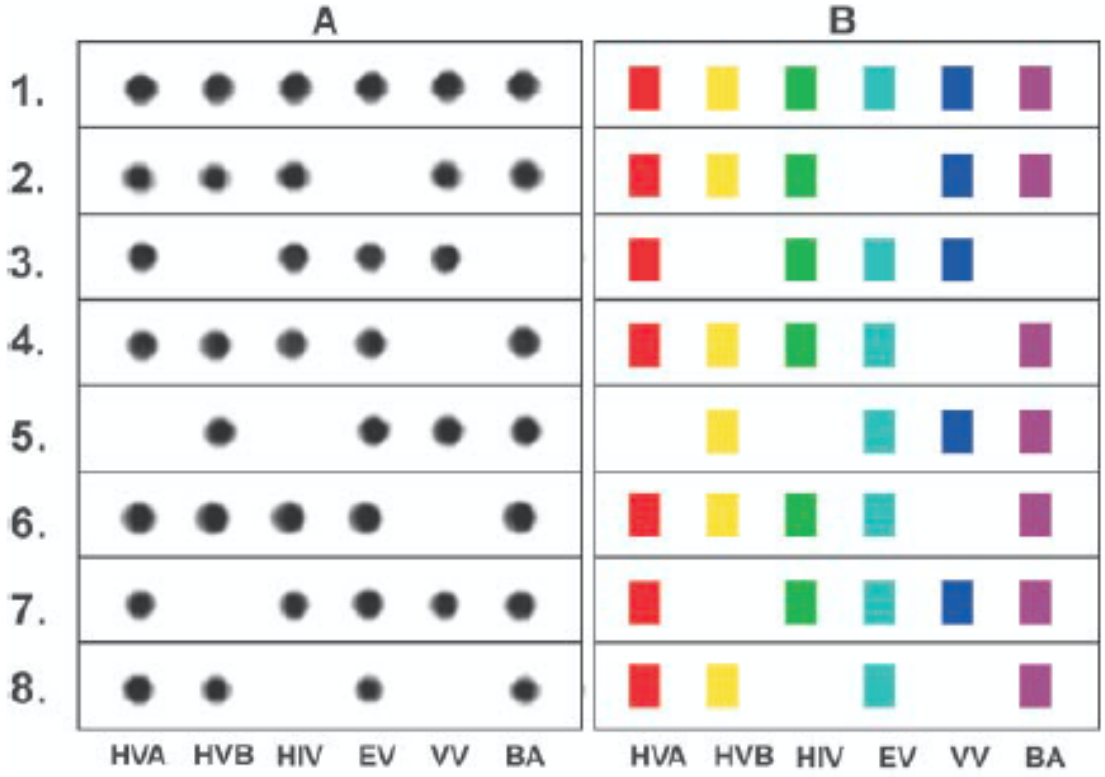

Fig. 3. (**A**) Flatbed scanner images of Ag-enhanced microarrays and (**B**) corresponding Raman spectra. The colored boxes correlate with the color-coded Raman spectra in Fig. 2. No false-positives or false-negatives were observed.

Bio-Bar-Code-Based DNA Detection with PCR-like Sensitivity

Jwa-Min Nam, Savka I. Stoeva, and Chad A. Mirkin*

J. AM. CHEM. SOC. 2004, *126*, 5932−5933

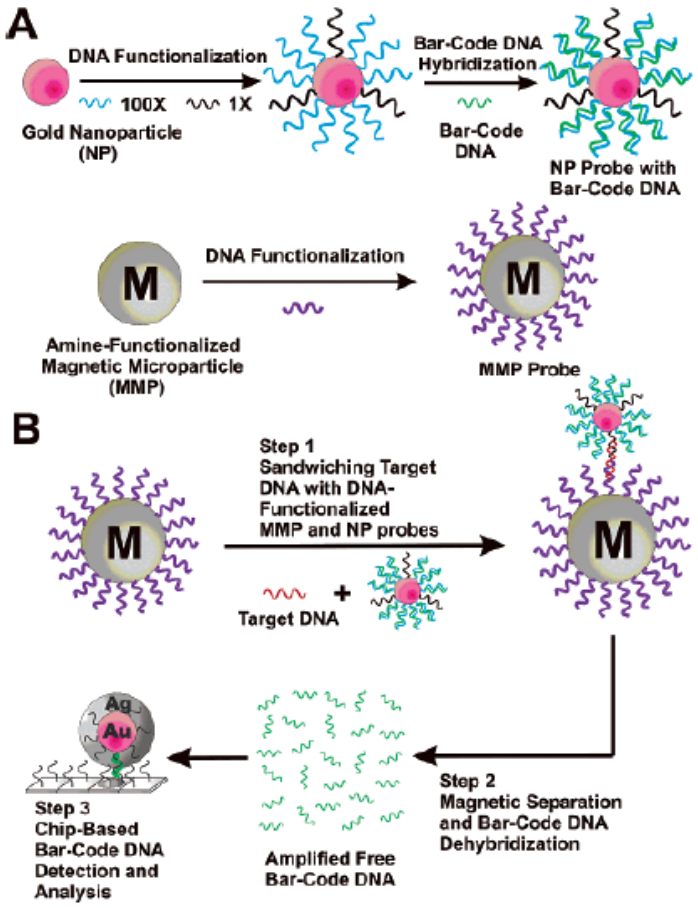

Figure 1. The DNA-BCA assay. (A) Nanoparticle and magnetic microparticle probe preparation. (B) Nanoparticle-based PCR-less DNA amplification scheme.

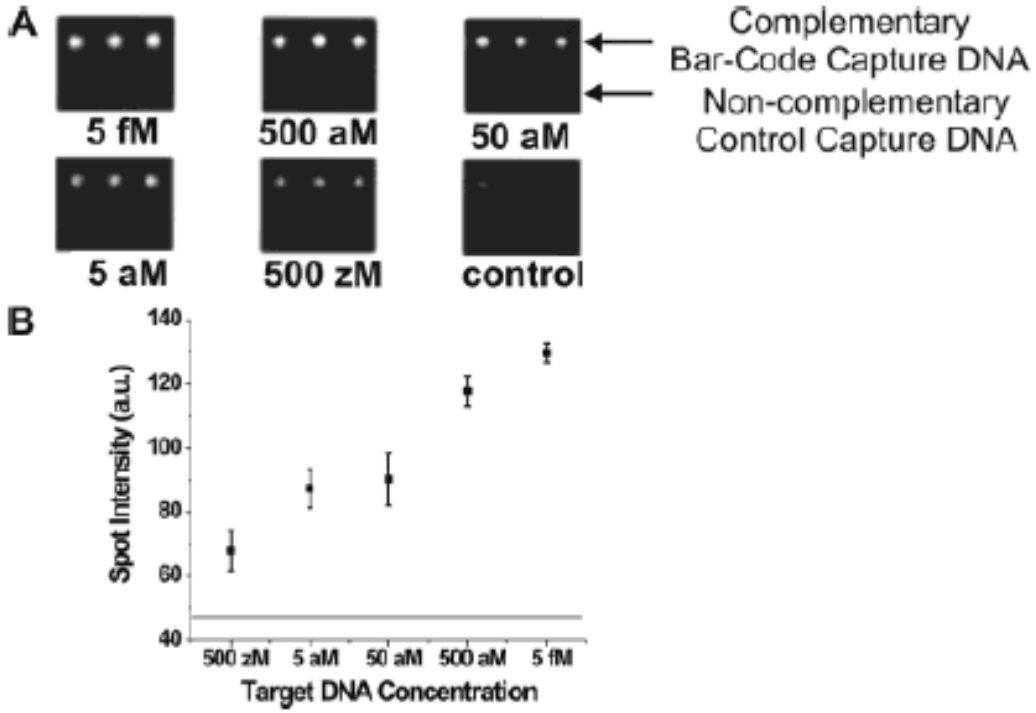

Figure 2. Amplified anthrax bar-code DNA detection with the Verigene ID system. (A) Anthrax bar-code DNA detection with 30 nm NP probes. (B) Quantitative data of spot intensities with 30 nm NP probes (Adobe Photoshop, Adobe Systems, Inc., San Jose, CA). The horizontal line represents control signal intensity (47 ± 2).

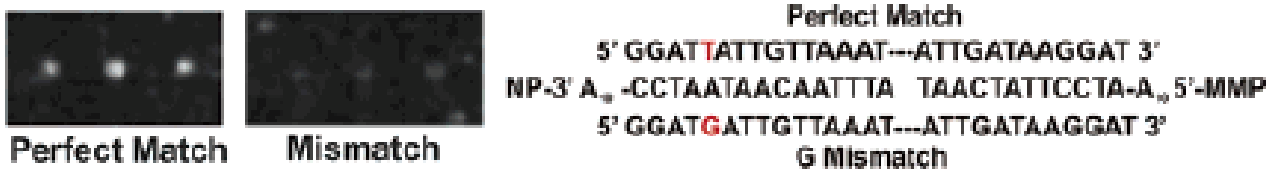

Figure 3. Single base mismatch experiment.

Nanoparticle-Based Bio–Bar Codes for the Ultrasensitive Detection of Proteins

26 SEPTEMBER 2003 VOL 301 SCIENCE

Jwa-Min Nam,* C. Shad Thaxton,* Chad A. Mirkin†

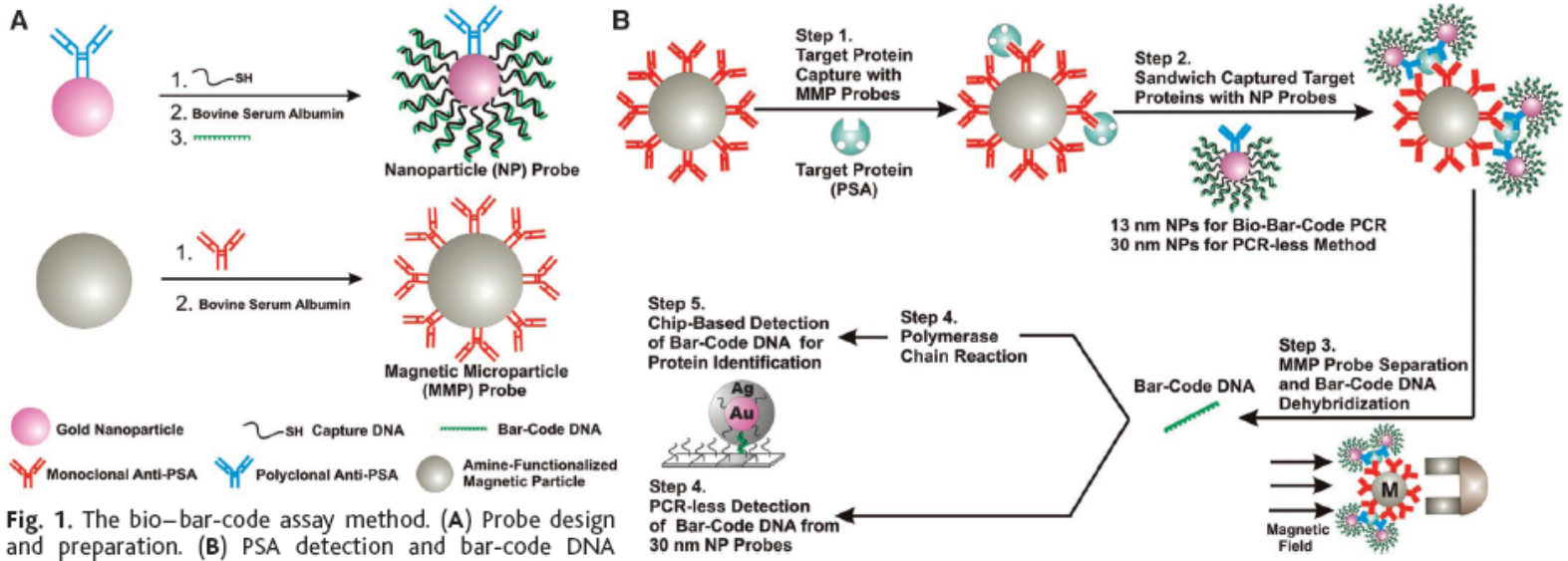

Fig. 1. The bio–bar-code assay method. (**A**) Probe design and preparation. (**B**) PSA detection and bar-code DNA amplification and identification. In a typical PSA-detection experiment, an aqueous dispersion of MMP probes functionalized with mAbs to PSA (50 μl of 3 mg/ml magnetic probe solution) was mixed with an aqueous solution of free PSA (10 μl of PSA) and stirred at 37°C for 30 min (Step 1). A 1.5-ml tube containing the assay solution was placed in a BioMag microcentrifuge tube separator (Polysciences, Incorporated, Warrington, PA) at room temperature. After 15 s, the MMP-PSA hybrids were concentrated on the wall of the tube. The supernatant (solution of unbound PSA molecules) was removed, and the MMPs were resuspended in 50 μl of 0.1 M phosphate-buffered saline (PBS) (repeated twice). The NP probes (for 13-nm NP probes, 50 μl at 1 nM; for 30-nm NP probes, 50 μl at 200 pM), functionalized with polyclonal Abs to PSA and hybridized bar-code DNA strands, were then added to the assay solution. The NPs reacted with the PSA immobilized on the MMPs and provided DNA strands for signal amplification and protein identification (Step 2). This solution was vigorously stirred at 37°C for 30 min. The MMPs were then washed with 0.1 M PBS with the magnetic separator to isolate the magnetic particles. This step was repeated four times, each time for 1 min, to remove everything but the MMPs (along with the PSA-bound NP probes). After the final wash step, the MMP probes were resuspended in NANOpure water (50 μl) for 2 min to dehybridize bar-code DNA strands from the nanoparticle probe surface. Dehybridized bar-code DNA was then easily separated and collected from the probes with the use of the magnetic separator (Step 3). For bar-code DNA amplification (Step 4), isolated bar-code DNA was added to a PCR reaction mixture (20-μl final volume) containing the appropriate primers, and the solution was then thermally cycled (*20*). The bar-code DNA amplicon was stained with ethidium bromide and mixed with gel-loading dye (*20*). Gel electrophoresis or scanometric DNA detection (*24*) was then performed to determine whether amplification had taken place. Primer amplification was ruled out with appropriate control experiments (*20*). Notice that the number of bound NP probes for each PSA is unknown and will depend upon target protein concentration.

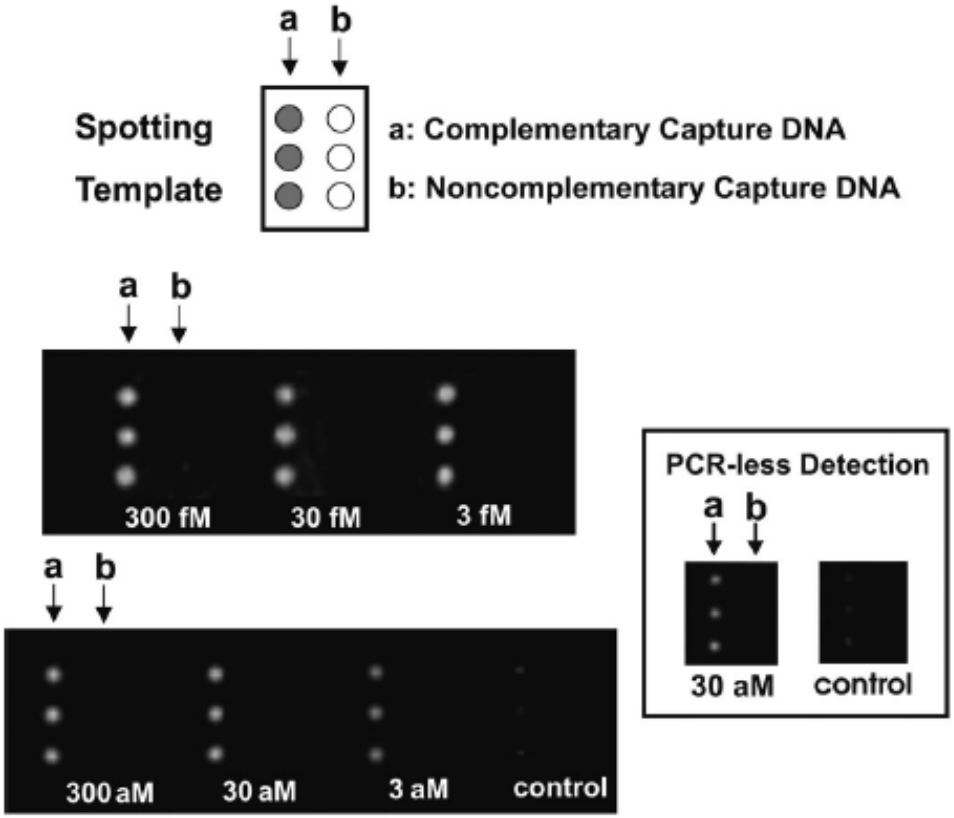

Fig. 2. Scanometric detection of PSA-specific bar-code DNA. PSA concentration (sample volume of 10 μl) was varied from 300 fM to 3 aM and a negative control sample where no PSA was added (control) is shown. For all seven samples, 2 μl of antidinitrophenyl (10 pM) and 2 μl of β-galactosidase (10 pM) were added as background proteins. Also shown is PCR-less detection of PSA (30 aM and control) with 30 nm NP probes (inset). Chips were imaged with the Verigene ID system (*20*).

Table 1. Detection Limits of Nucleic Acid Assays[a]

	assay	ss DNA	PCR products	genomic DNA
nanostructure-based methods	colorimetric[29] (cross-linked Au nanoparticles)	~10 nM		
	colorimetric[36] (non-cross-linked Au nanoparticles)	60 nM		
	magnetic relaxation[97] (iron oxide nanoparticles)	20 pM		
	electrochemical[96] (nanoparticles)	270 pM		
	scanometric[35,66,67] (Au nanoparticles with Ag amplification)	50 fM	100 aM[b]	200 fM
	Raman spectroscopy[68] (Au nanoparticles with Ag amplification)	~1 fM		
	electrical[93] (Au nanoparticles with Ag amplification)	500 fM		
	electrical[99] (Si nanowire)	10 fM		
	electrical[103] (carbon nanotube)	54 aM		
	resonant light-scattering[61–66] (metal nanoparticles)	170 fM[b]		33 fM
	fluorescence[56] (ZnS and CdSe quantum dots)	2 nM		
	surface plasmon resonance[41] (Au nanoparticles)	10 pM		
	quartz crystal microbalance[94] (Au nanoparticles)	~1 fM		
	laser diffraction[42] (Au nanoparticles)	~50 fM		
	fluorescence[45] (fluorescent nanoparticles)	~1 fM		
	bio-bar-code amplification[71] (Au nanoparticles with Ag amplification)	500 zM		
other non-enzymatic based methods	fluorescence[35] (molecular fluorophores)		~600 fM[b]	
	fluorescence (dendrimer amplification)[134]		2.5 μg	
	electrochemical amplification[136] (electroactive reporter molecules)	100 aM		

[a] Detection limits can vary based on target length and sequence; therefore, it is difficult to compare assays without testing them using identical targets and conditions. [b] Values taken from ref 34.

Table 2. Detection Limits of Protein Assays

	assay	target	protein in saline	protein in serum
nanostructure-based methods	optical[72] (Au nanoshells)	rabbit IgG	0.88 ng/mL (~4.4 pM)[a]	0.88 ng/mL (~4.4 pM)[c]
	optical[74] (Au nanoparticles)	IgE and IgG1	~20 nM	
	magnetic relaxation[98] (iron oxide nanoparticles)	adenovirus (ADV) and herpes simplex virus (HSV)	100 ADV/ 100μL	50 HSV/ 100 μL
	scanometric[79] (Au nanoparticles with Ag amplification)	mouse IgG	200 pM	
	Raman[82] (Au nanoparticles with Raman labels)	prostate-specific antigen		30 fM
	surface plasmon resonance[83,84] (triangular Ag particles on surfaces)	streptavidin(S A) and anti-biotin (AB)	~1 pM SA and ~700 pM AB	
	electrical[110] (single-walled carbon nanotubes)	10E3 antibody to U1A RNA splicing factor	~1 nM	
	electrical[20] (Si nanowires)	streptavidin	10 pM	
	bio-bar-code amplification[75] (Au nanoparticles with Ag amplification)	prostate-specific antigen	30 aM (3 aM)[b]	(30 aM)[b]
molecular fluorophore methods	enzyme-linked immunosorbent assay	various	pM range	pM range
electrochemical methods	electrochemical amplification[137] (oligonucleotide reporter molecules)	IgG	13 fM	
enzyme-based amplification methods	immuno-PCR[76]	bovine serum albumin	2 fM	
	rolling circle amplification[77]	prostate-specific antigen	3 fM	

[a] Reported in ng/mL; authors converted to molar concentration for ease of comparison. [b] These values are the lower limits when PCR is used to amplify the bar-code DNA prior to scanometric detection of bar codes.

Surface Plasmon

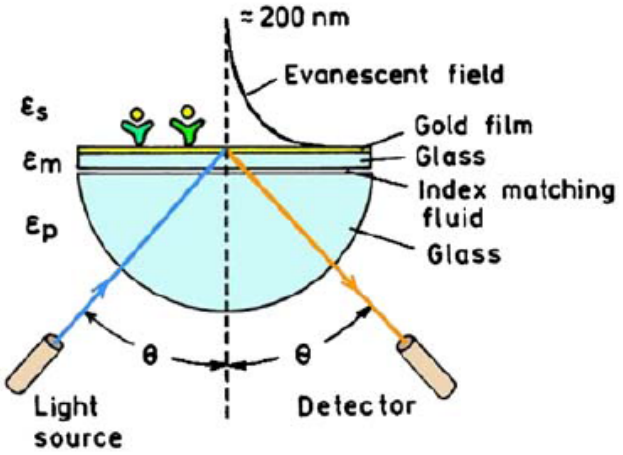

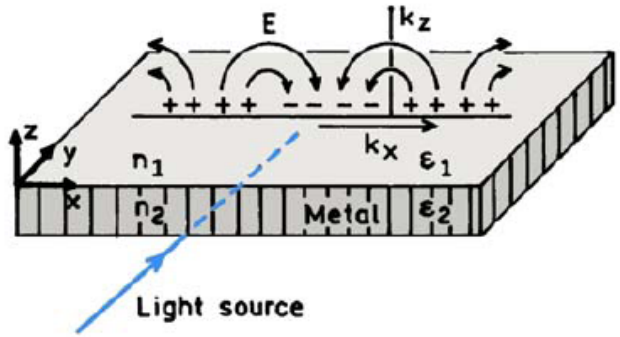

Figure 3. Schematics of an SPR experiment (top) and of the light-induced surface plasmons (bottom).

(b)

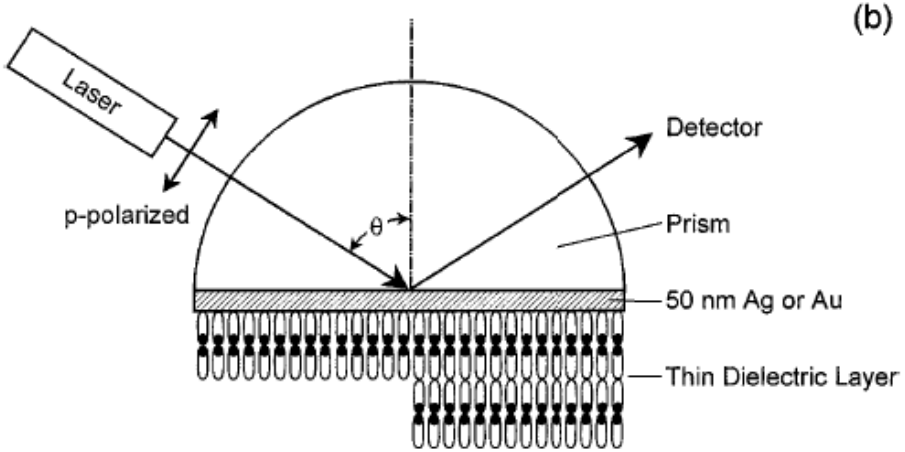

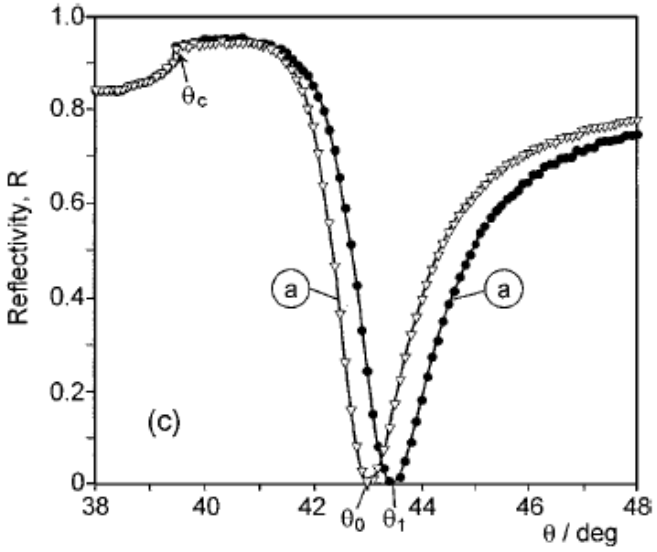

Drift: Drude model

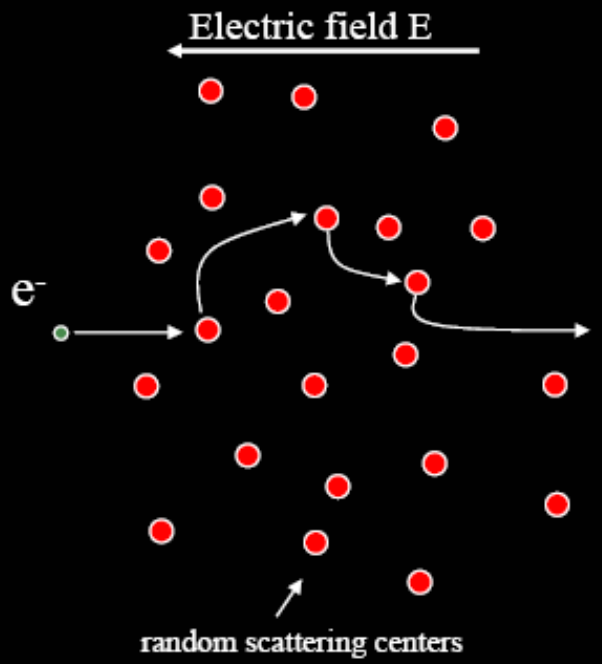

$$F = ma$$

$$eE = m\frac{\partial v}{\partial t}$$

$$v_{avg} = \underbrace{\frac{e\tau}{m}}_{\mu} E$$

$$j = nev_{avg} = \underbrace{\frac{ne^2\tau}{m}}_{\sigma} E$$

$$m\frac{\partial}{\partial t}\langle\vec{v}\rangle = q\vec{E} - \gamma\langle\vec{v}\rangle$$

$$\sigma(\omega) = \frac{\sigma_0}{1 + i\omega\tau}$$

AC Dielectric Response

$$\varepsilon_m = 1 - \frac{\omega_p^2}{\omega^2}$$

Plasma frequency

polarizability of a small metal sphere with dielectric function $\varepsilon(\lambda)$

$$\alpha = R^3 \frac{\varepsilon - 1}{\varepsilon + 2}\,.$$

$$\varepsilon = \varepsilon_\mathrm{b} + 1 - \frac{\omega_\mathrm{P}^2}{\omega^2 + \mathrm{i}\omega\gamma}\,,$$

$$\alpha = \frac{R^3(\varepsilon_\mathrm{b}\omega^2 - \omega_\mathrm{P}^2) + i\omega\gamma\varepsilon_\mathrm{b}}{[(\varepsilon_\mathrm{b} + 3)\omega^2 - \omega_\mathrm{P}^2] + i\omega\gamma(\varepsilon_\mathrm{b} + 3)}\,.$$

$\omega_\mathrm{R} = \frac{\omega_\mathrm{P}}{\sqrt{\varepsilon_\mathrm{b}+3}}$ $\qquad\qquad$ $\gamma(\varepsilon_\mathrm{b} + 3)$.

Biomolecular Binding in Real Time

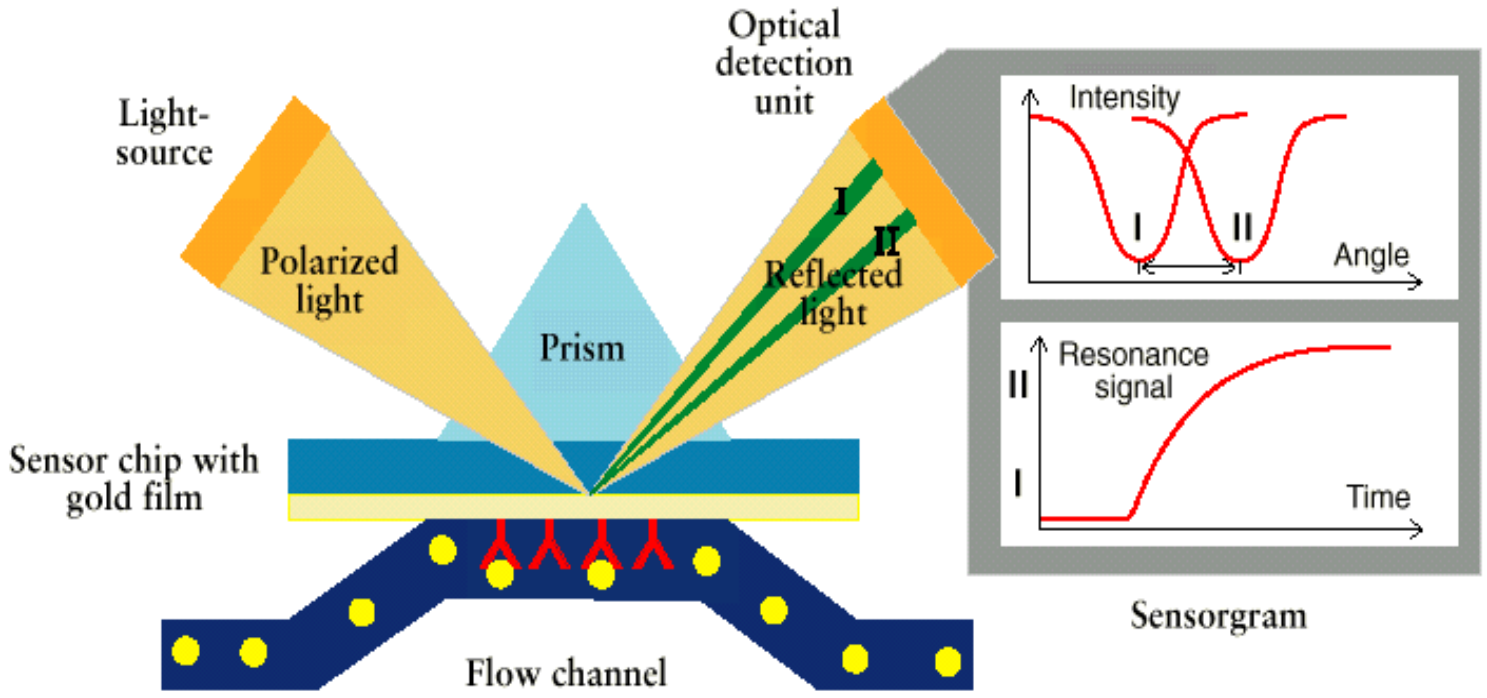

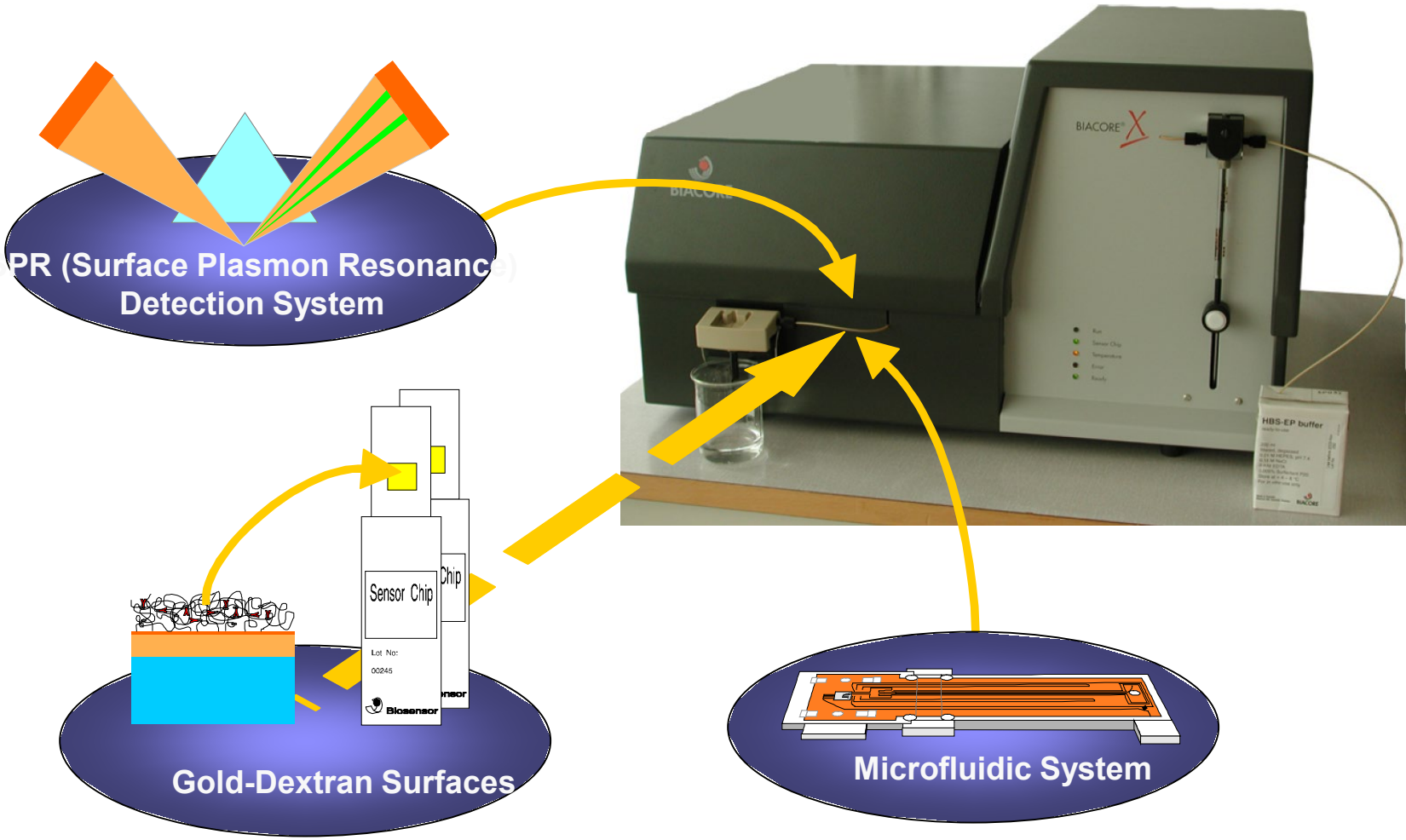
SPR (Surface Plasmon Resonance)
Detection System
BIACORE X
HBS-EP buffer
Sensor Chip
Lot No:
00245
Biosensor
Gold-Dextran Surfaces
Microfluidic System

SPR Imaging Apparatus

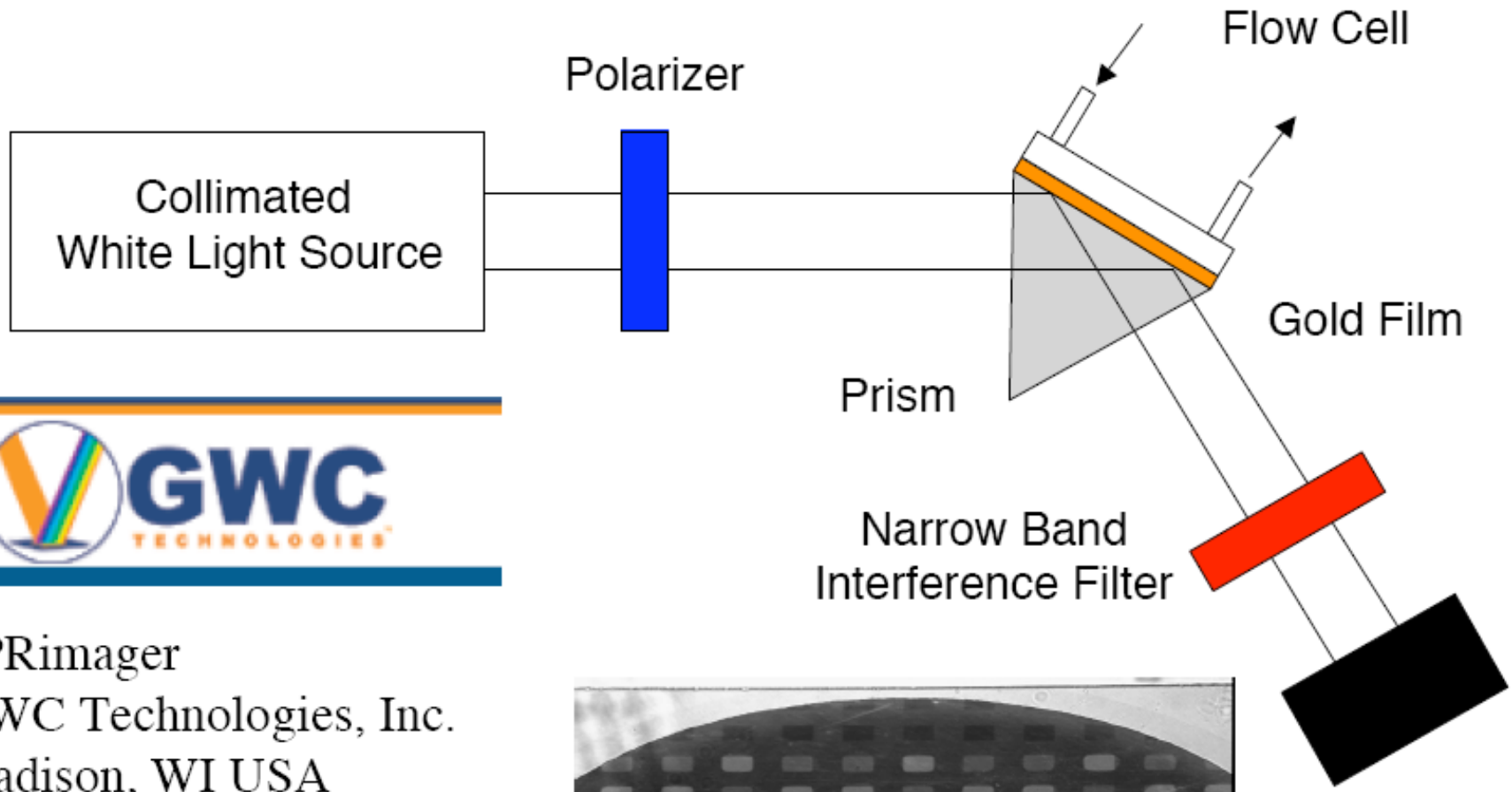

SPRimager
GWC Technologies, Inc.
Madison, WI USA

www.gwctechnologies.com

Raw Image

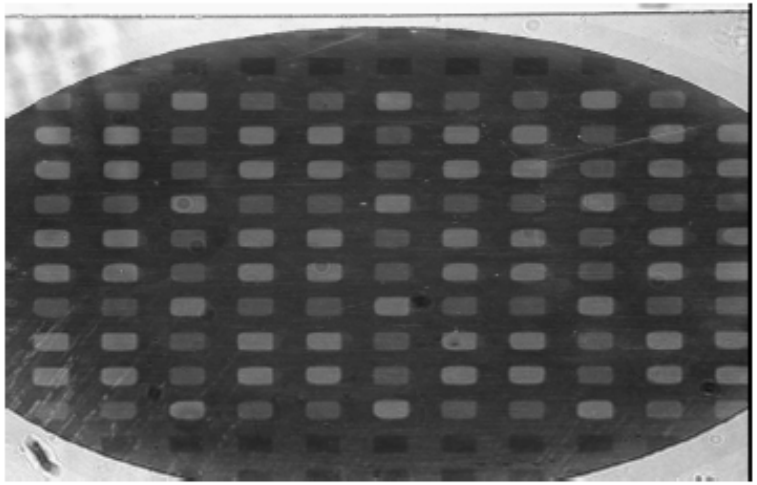

UCIrvin
University of California, Ir

Localized Plasmon

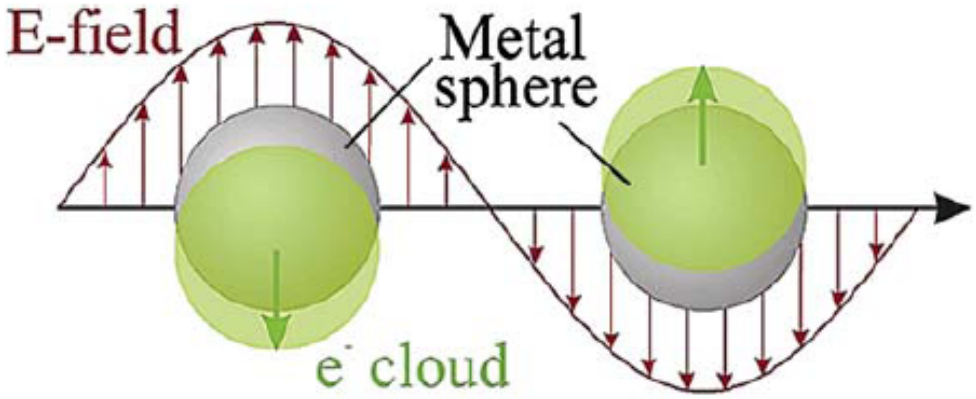

Figure 6. Schematic of plasmon oscillation for a sphere. From [39].

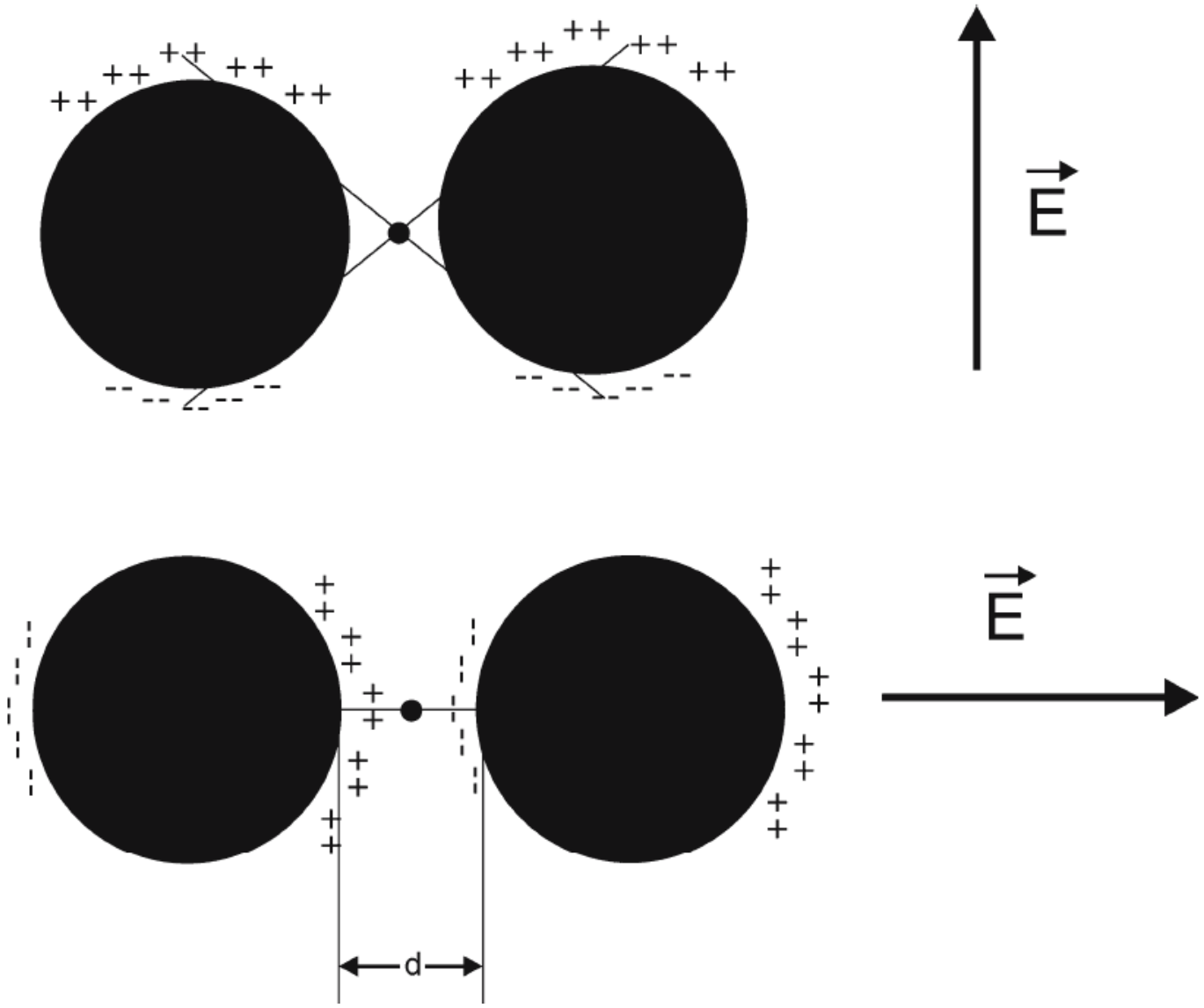
E
E
d

field enhancement

$E_s = gE_0$, where E_0 is the magnitude of the incident field

$$E_R \propto \alpha_R E_s \propto \alpha_R g E_0$$

$$E_{SERS} \propto \alpha_R g g' E_0$$

$$I_{SERS} \propto |\alpha_R|^2 |gg'|^2 I_0$$

$$g \cong g'$$

$$|E_L|^4 = |g|^4.$$

Probing Single Molecules and Single Nanoparticles by Surface-Enhanced Raman Scattering

SCIENCE • VOL. 275 • 21 FEBRUARY 1997

Shuming Nie* and Steven R. Emory

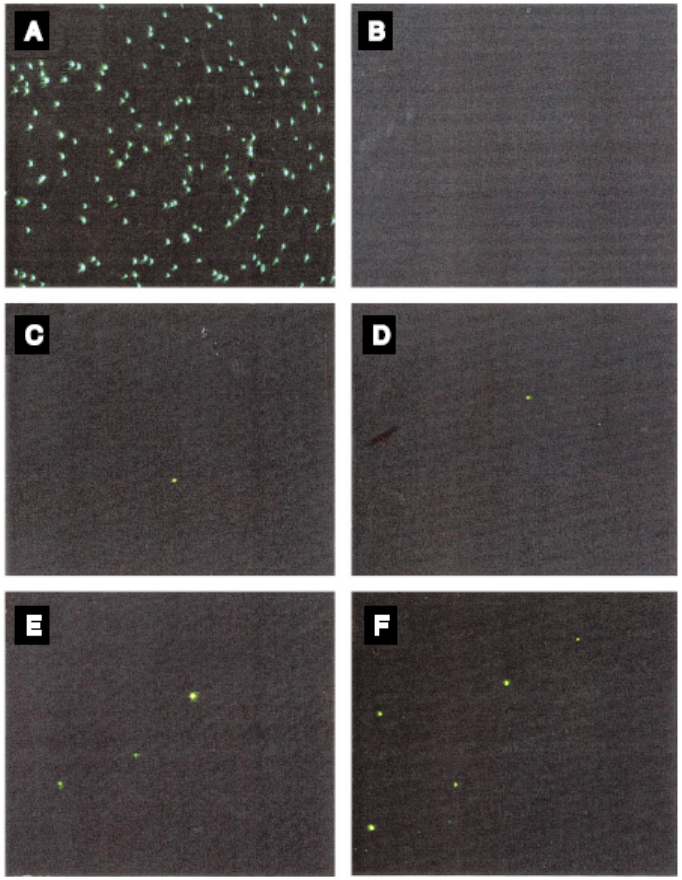

Fig. 1. Single Ag nanoparticles imaged with evanescent-wave excitation. Total internal reflection of the laser beam at the glass-liquid interface was used to reduce the laser scattering background. The instrument setup for evanescent-wave microscopy was adapted from Funatsu *et al.* (*11*). The images were directly recorded on color photographic film (ASA-1600) with a 30-s exposure by a Nikon 35-mm camera attached to the microscope. (**A**) Unfiltered photograph showing scattered laser light from all particles immobilized on a polylysine-coated surface. (**B**) Filtered photographs taken from a blank Ag colloid sample (incubated with 1 mM NaCl and no R6G analyte molecules). (**C**) and (**D**) Filtered photographs taken from a Ag colloid sample incubated with 2×10^{-11} M R6G. These images were selected to show at least one Raman scattering particle. Different areas of the cover slip were rapidly screened, and most fields of view did not contain visible particles. (**E**) Filtered photograph taken from Ag colloid incubated with 2×10^{-10} M R6G. (**F**) Filtered photograph taken from Ag colloid incubated with 2×10^{-9} M R6G. A high-performance bandpass filter was used to remove the scattered laser light and to pass Stokes-shifted Raman signals from 540 to 580 nm (920 to 2200 cm^{-1}). Continuous-wave excitation at 514.5 nm was provided by an Ar ion laser. The total laser power at the sample was 10 mW. Note the color differences between the scattered laser light in (A) and the red-shifted light in (C) through (F).

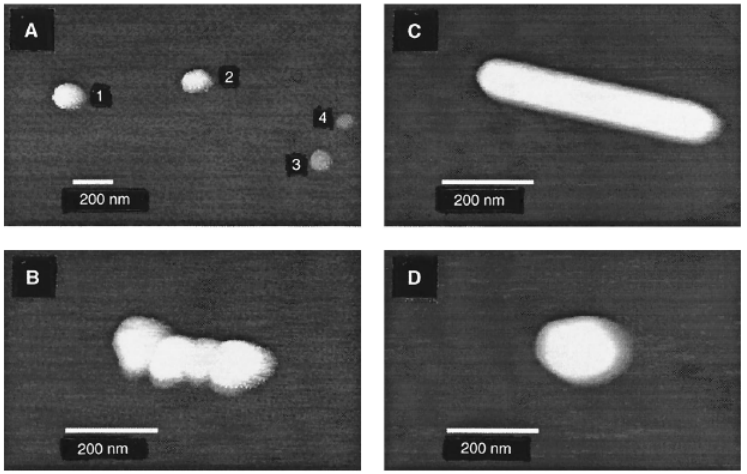

Fig. 2. Tapping-mode AFM images of screened Ag nanoparticles. (**A**) Large area survey image showing four single nanoparticles. Particles 1 and 2 were highly efficient for Raman enhancement, but particles 3 and 4 (smaller in size) were not. (**B**) Close-up image of a hot aggregate containing four linearly arranged particles. (**C**) Close-up image of a rod-shaped hot particle. (**D**) Close-up image of a faceted hot particle.

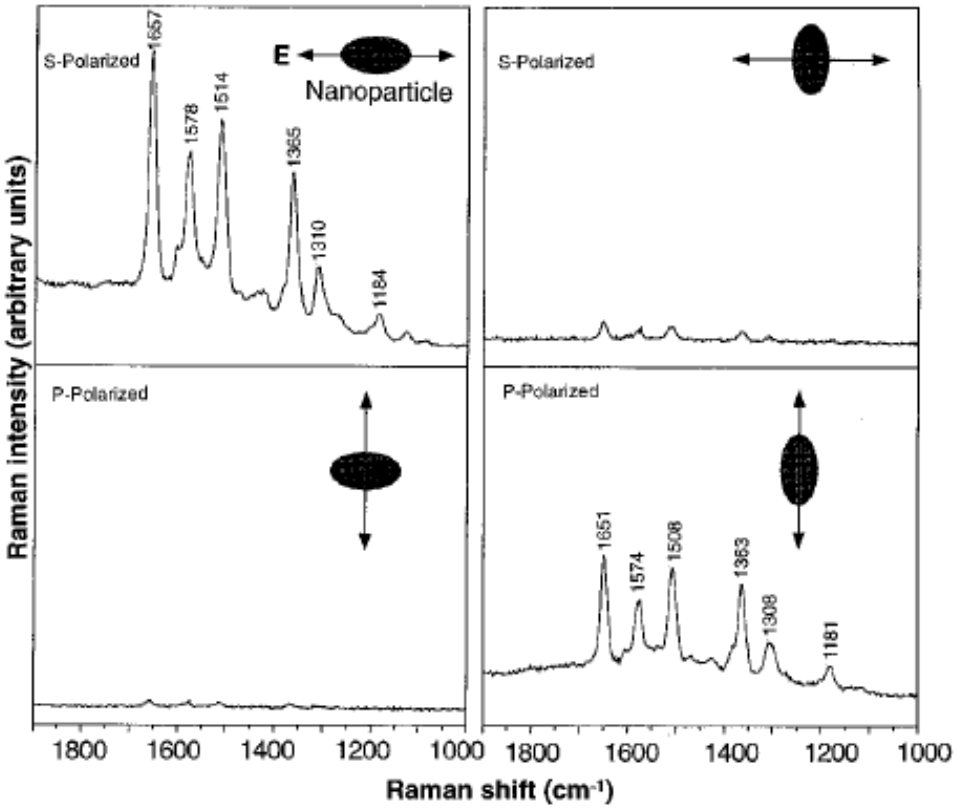

Fig. 3. Surface-enhanced Raman spectra of R6G obtained with a linearly polarized confocal laser beam from two Ag nanoparticles. The R6G concentration was 2×10^{-11} M, corresponding to an average of 0.1 analyte molecule per particle. The direction of laser polarization and the expected particle orientation are shown schematically for each spectrum. Laser wavelength, 514.5 nm; laser power, 250 nW; laser focal radius, ~250 nm; integration time, 30 s. All spectra were plotted on the same intensity scale in arbitrary units of the CCD detector readout signal.

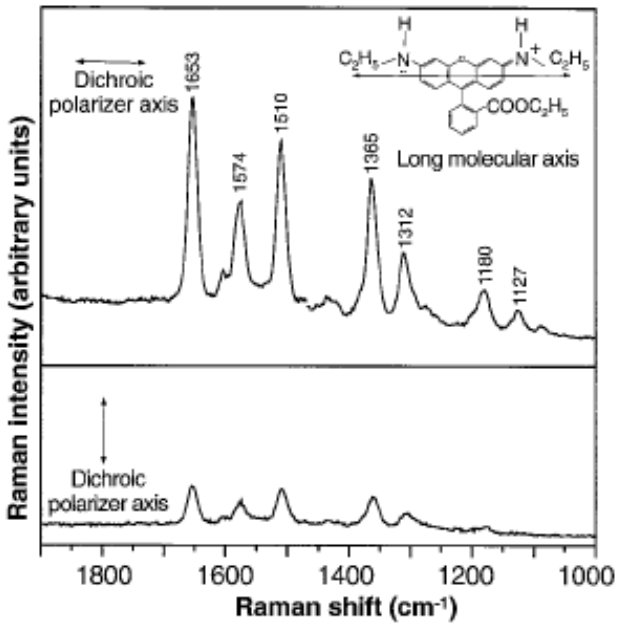

Fig. 4. Emission-polarized surface-enhanced Raman signals of R6G observed from a single Ag nanoparticle with a polarization-scrambled confocal laser beam. A dichroic sheet polarizer was rotated 90° to select Raman scattering signals polarized parallel (upper spectrum) or perpendicular (lower spectrum) to the long molecular axis of R6G. (**Inserts**) Structure of R6G, the electronic transition dipole (along the long axis when excited at 514.5 nm), and the dichroic polarizer orientations. Other conditions as in Fig. 3.

troscopic signatures of adsorbed molecules. For single rhodamine 6G molecules adsorbed on the selected nanoparticles, the intrinsic Raman enhancement factors were on the order of 10^{14} to 10^{15}, much larger than the ensemble-averaged values derived from conventional measurements. This enormous enhancement leads to vibrational Raman signals that are more intense and more stable than single-molecule fluorescence.

Electromagnetic contributions to single-molecule sensitivity in surface-enhanced Raman scattering

PRE 62 4318

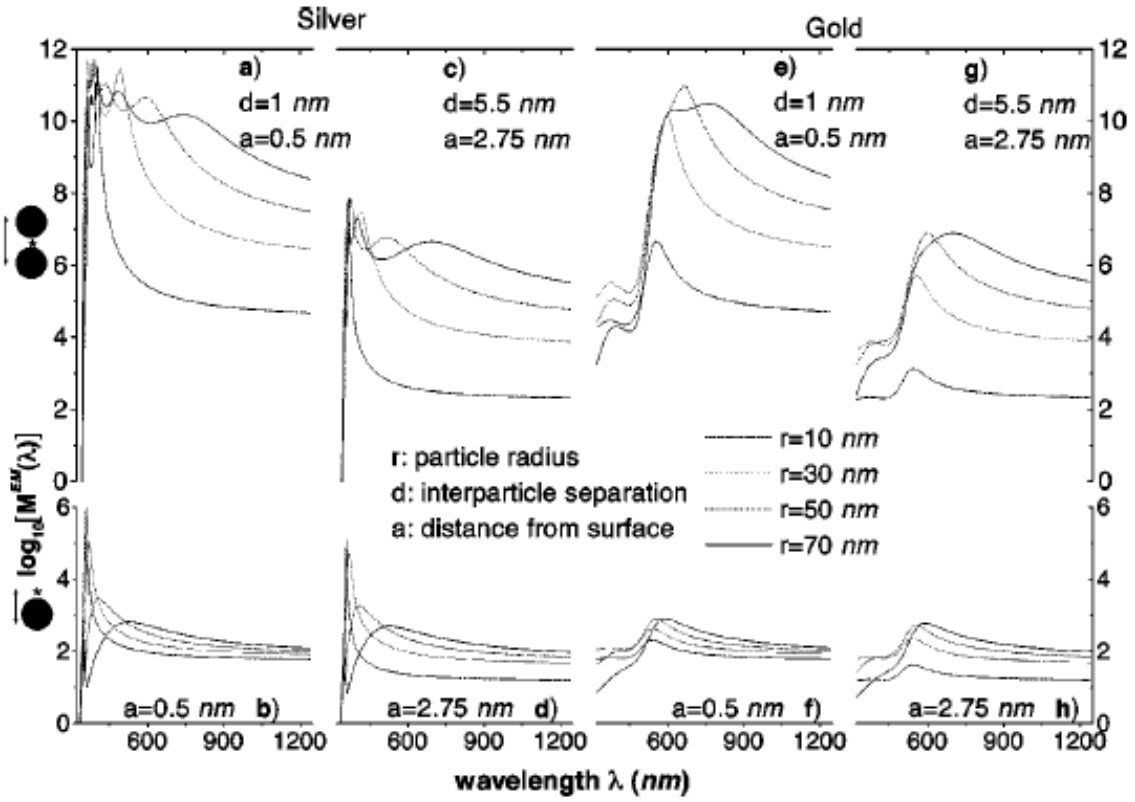

FIG. 3. (Color) EM-enhancement factor M^{EM} at a cross section through six different silver particle configurations. The wavelength of the incident field is $\lambda = 514.5$ nm with vertical polarization. The left-hand column illustrates the EM enhancement for dimer configurations of two spheres (top) and two polygons (bottom) with a separation of 1 nm. The middle column shows the same situation, but with a separation distance of 5.5 nm. The right-hand column shows the case of an isolated single particle. All particles share a common largest dimension of 90 nm. Note that the color scale from dark blue to dark red is logarithmic, covering the interval $10^0 < M^{EM} < 10^8$. Regions with enhancement outside this interval are shown in dark blue and dark red, respectively.

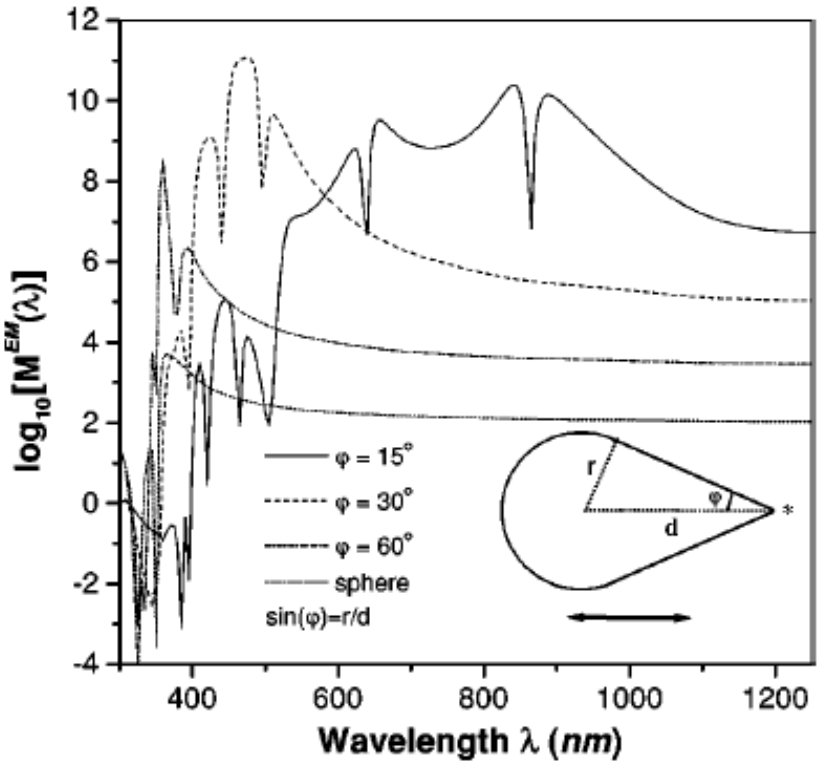

FIG. 5. EM-enhancement factor for a rotationally symmetric silver droplet as a function of the angle defining the opening edge ϕ. The field is polarized parallel to the axis of the droplet and the evaluation position (star) is located 0.5 nm outside the tip. As the droplet becomes sharper the enhancement increases several orders of magnitude.

Nanosphere Arrays with Controlled Sub-10-nm Gaps as Surface-Enhanced Raman Spectroscopy Substrates

J. AM. CHEM. SOC. 2005, *127*, 14992−14993

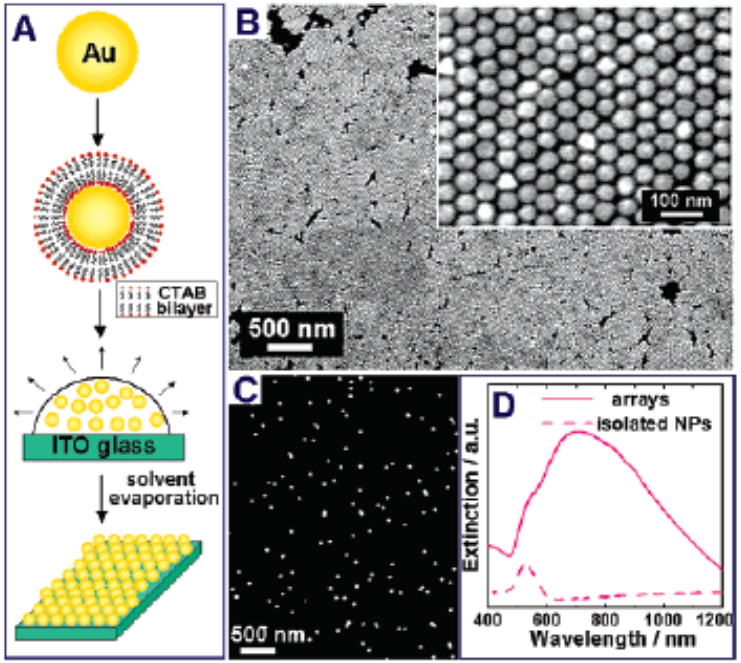

Figure 1. (A) Schematic illustration of the fabrication of sub-10-nm gap Au NP arrays. (B) SEM image of the arrays. (C) SEM image of monolayer of isolated Au NPs on ITO glass. (D) Vis−NIR extinction spectrum of the monolayer of isolated Au NPs and arrays.

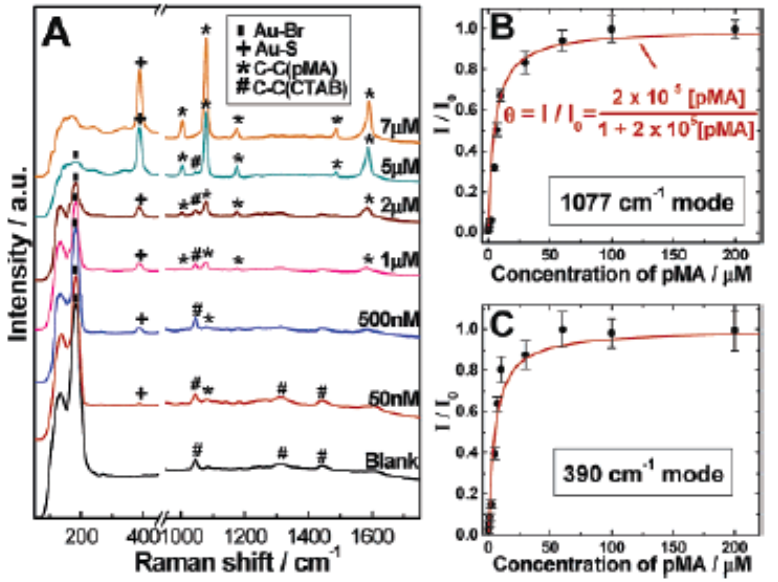

Figure 2. (A) SERS spectra of 5 μL of pMA with different concentrations deposited on the NP arrays. The excitation laser wavelength is 785 nm. Adsorption isotherm of pMA on the NP arrays obtained according to (B) 1077 and (C) 390 cm^{-1} modes in the SERS spectra. I_0 is the peak intensity of a saturated pMA monolayer.

Profiling the Near Field of a Plasmonic Nanoparticle with Raman-Based Molecular Rulers

NANO LETTERS

2006
Vol. 6, No. 10
2338−2343

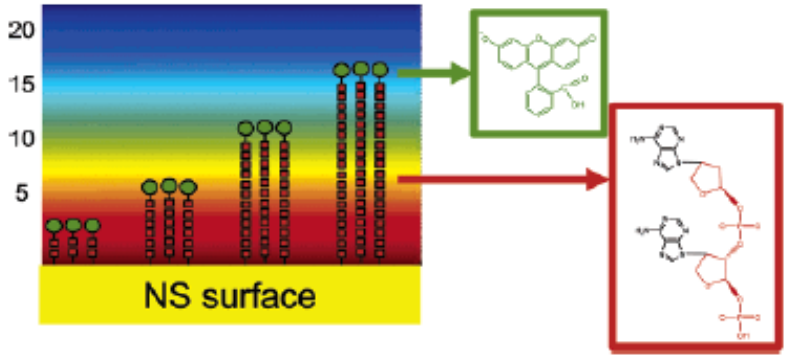

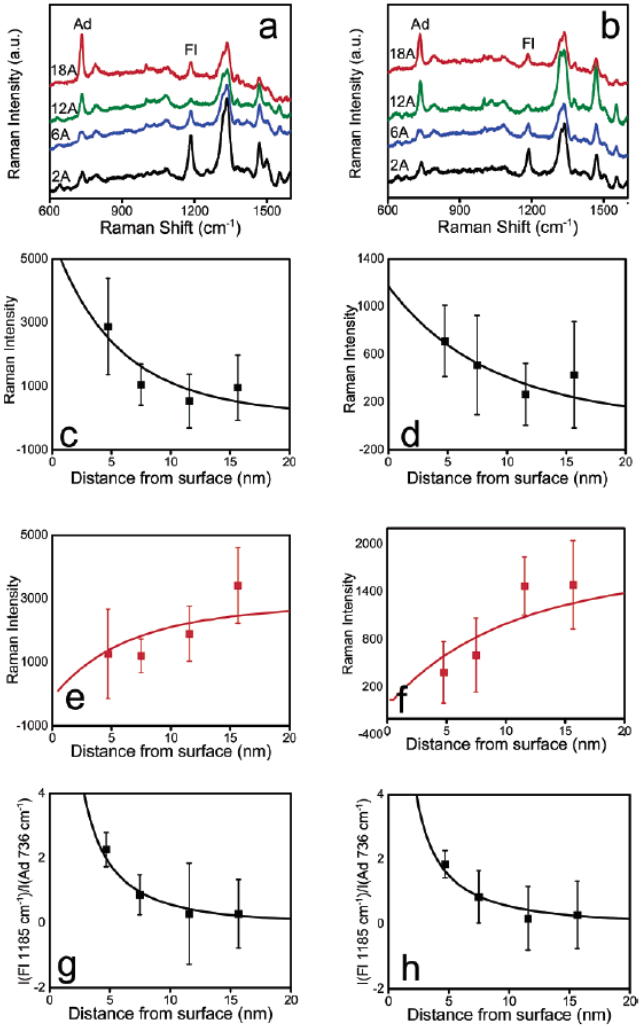

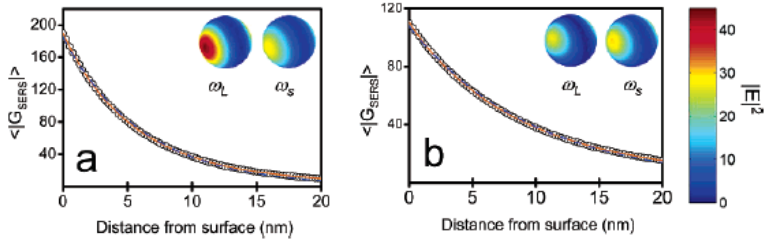

•Eukaryotic cells are about 1000 times larger than bacteria cells and also have a membrane enclosed nucleus containing their DNA, and several other internal structures known as organelles.

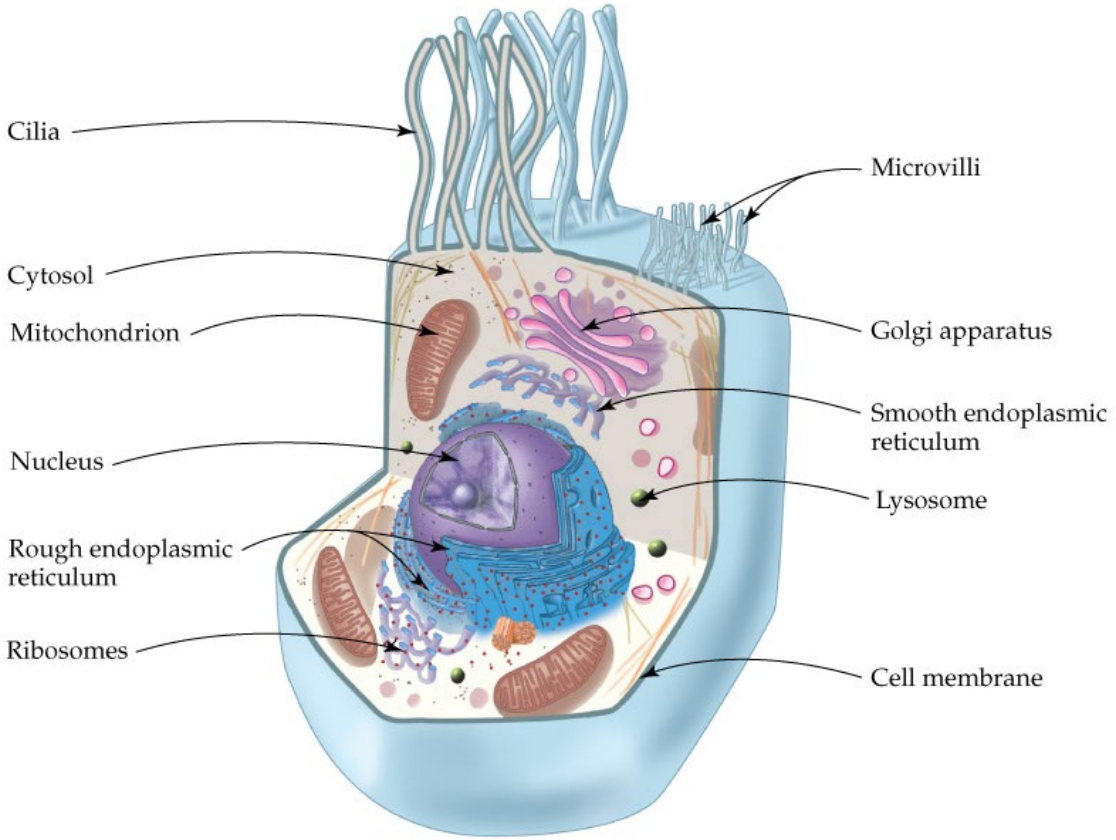

Fig 21.3 A generalized eukaryotic cell.

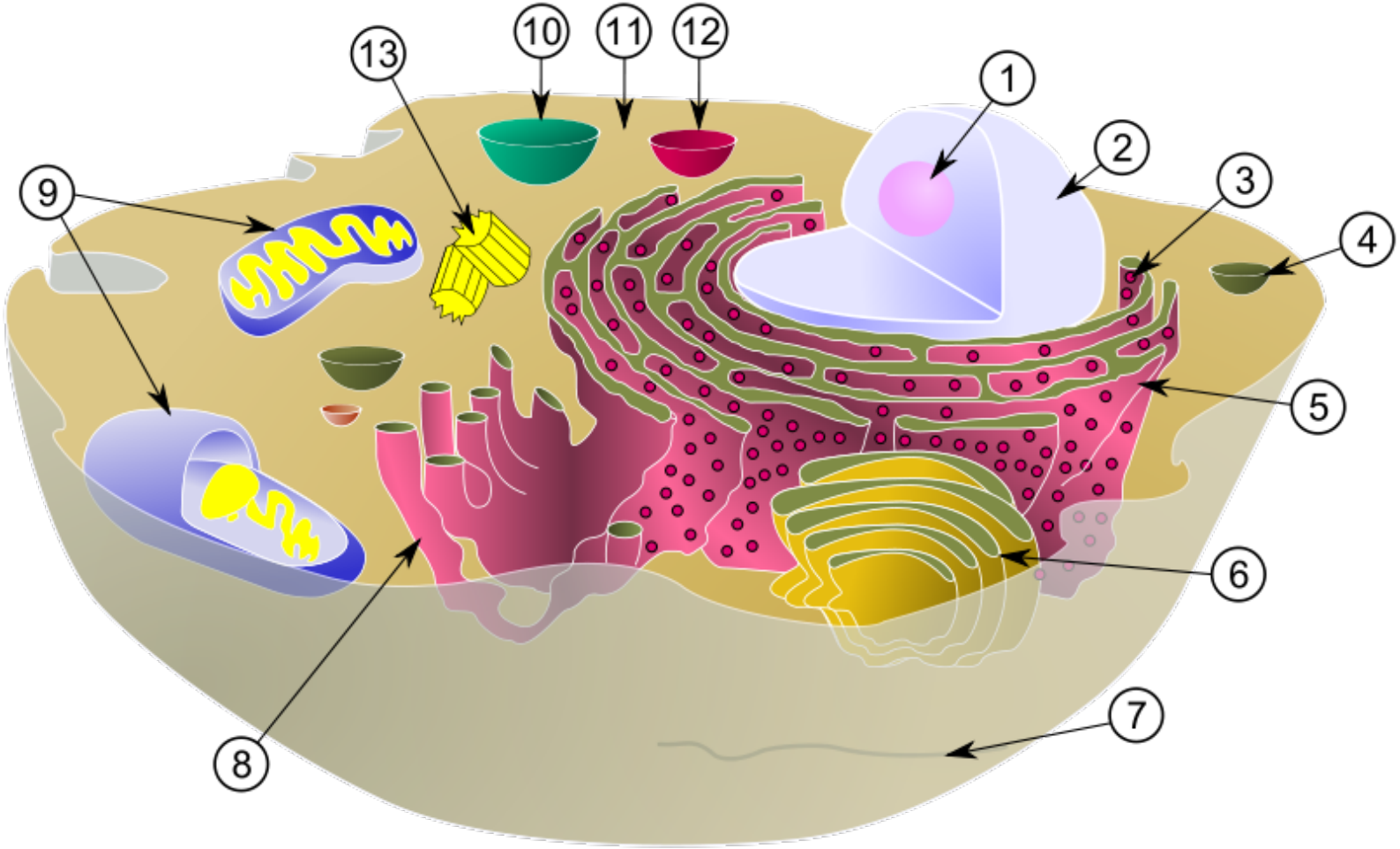

•Schematic showing the cytoplasm, with its components (or *organelles*), of a typical animal cell. Organelles: (1) nucleolus (2) nucleus (3) ribosome (4) vesicle (5) rough endoplasmic reticulum (6) Golgi apparatus (7) cytoskeleton (8) smooth endoplasmic reticulum (9) mitochondria (10) vacuole (11) cytosol (12) lysosome (13) centriole.

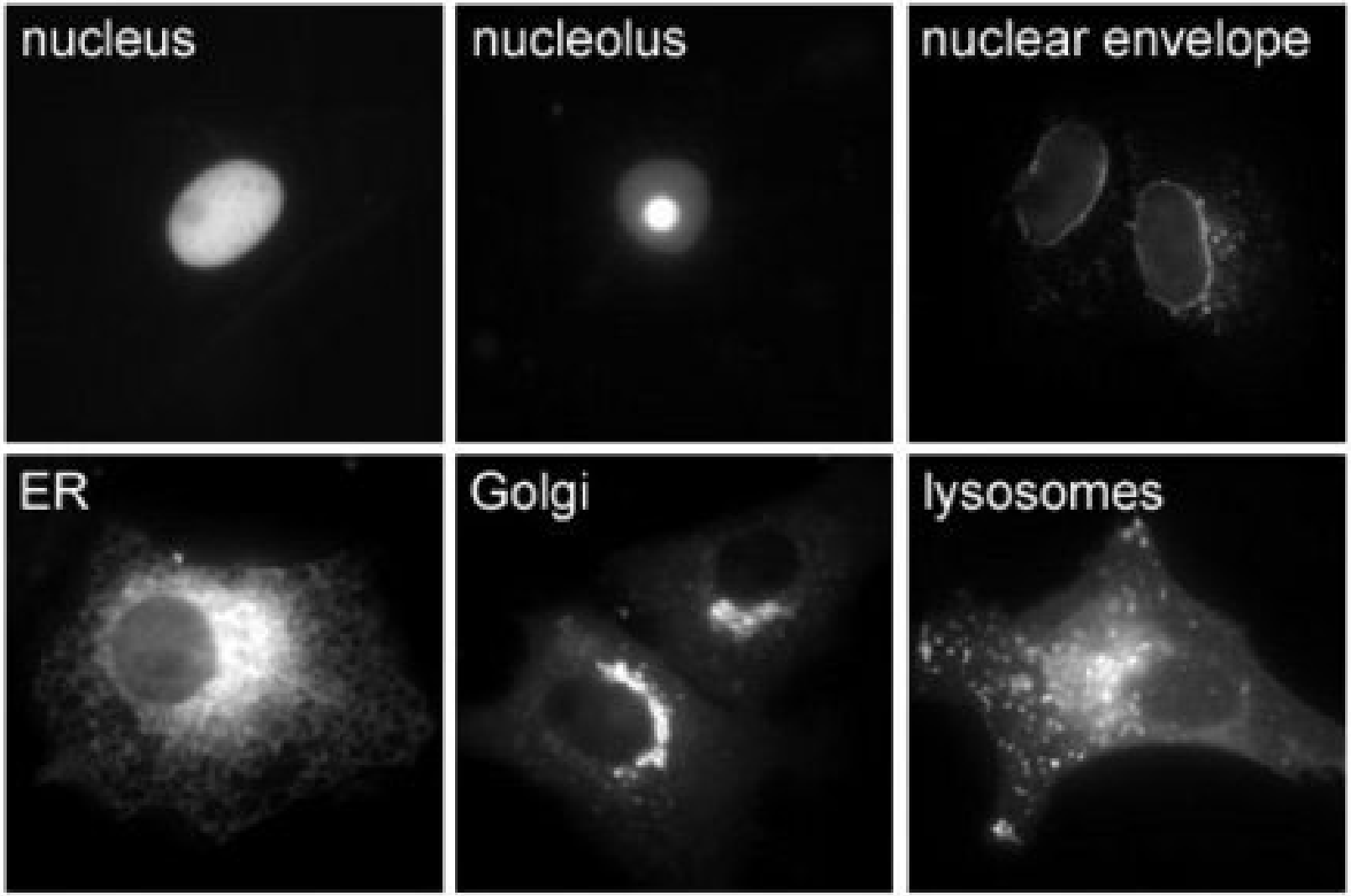
nucleus
nucleolus
nuclear envelope
ER
Golgi
lysosomes

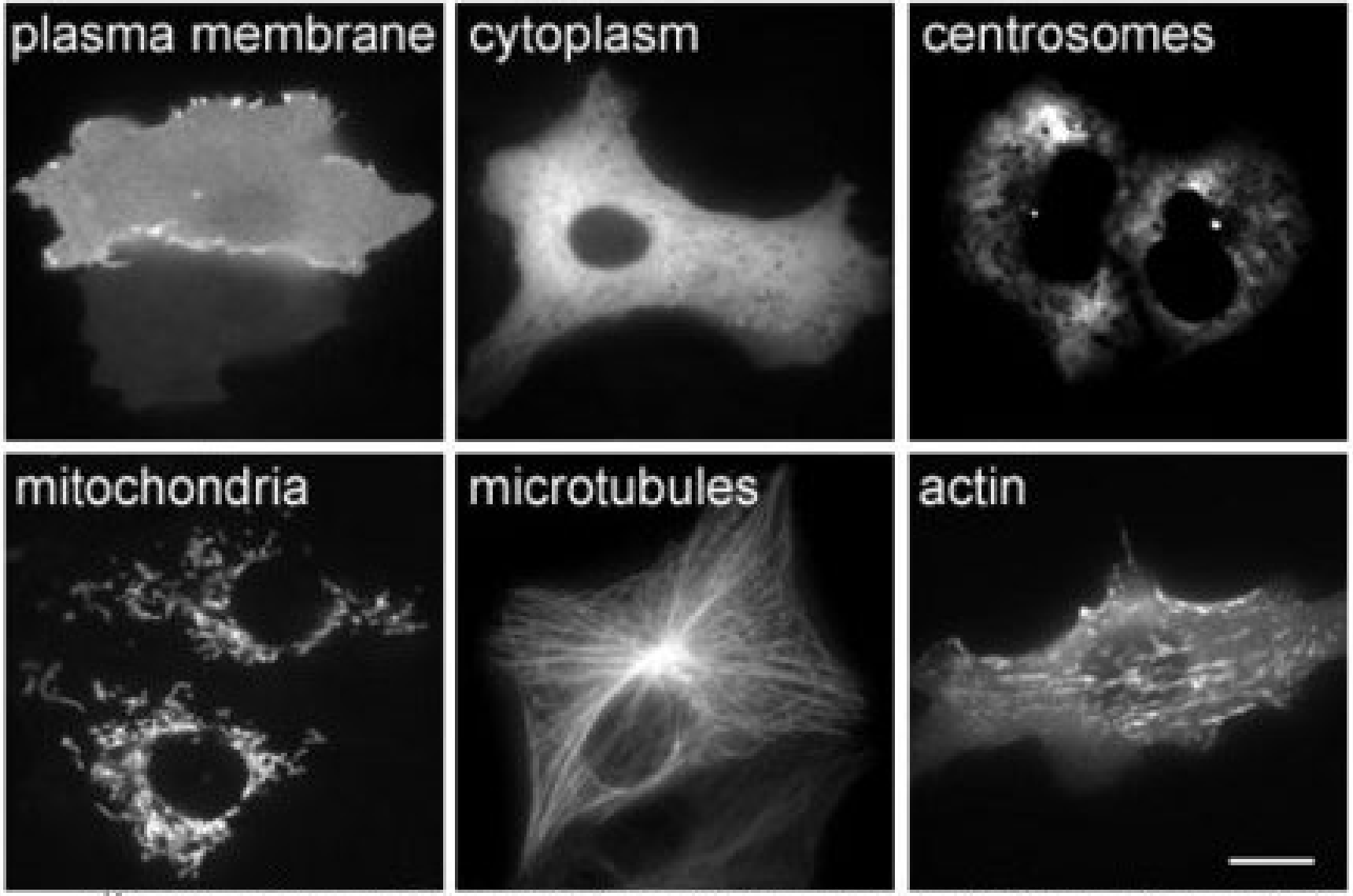

with friendly permission of Jeremy Simpson and Rainer Pepperkok

A Busy Factory

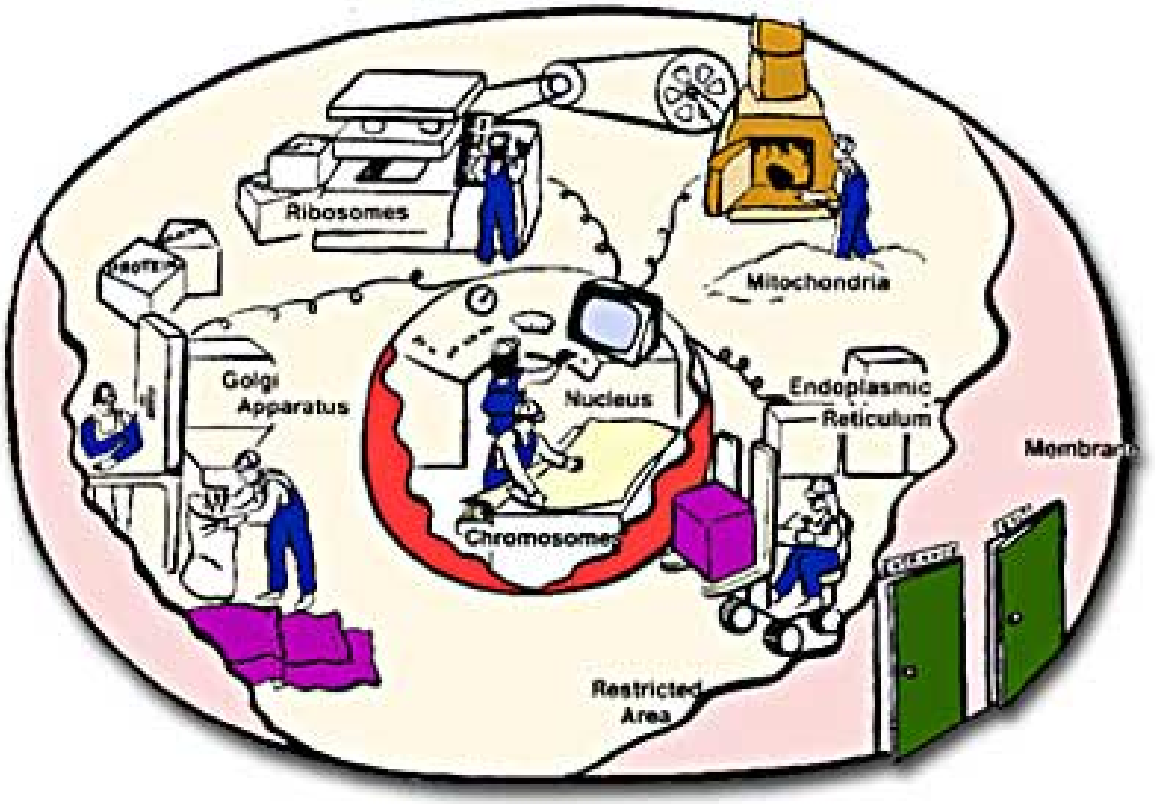

A cell can be thought of as a "factory," with different departments each performing specialized tasks.

The Plasma Membrane

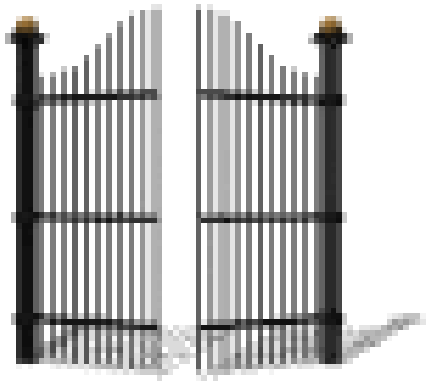

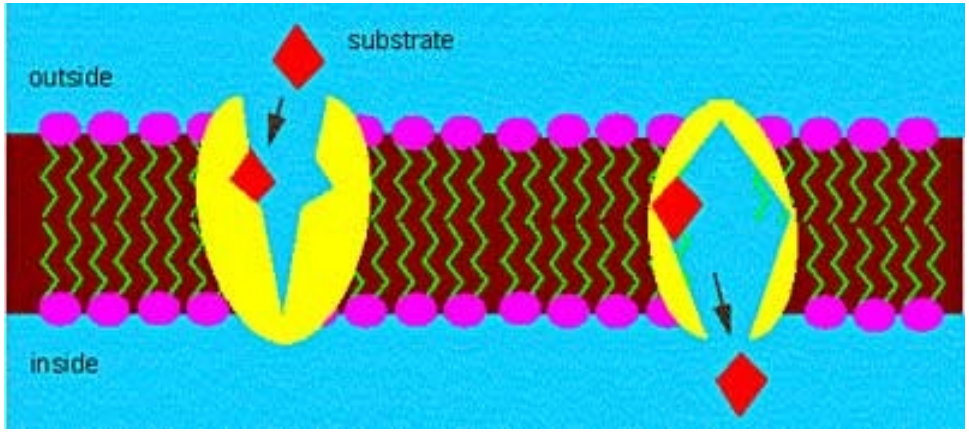

Cell Membrane

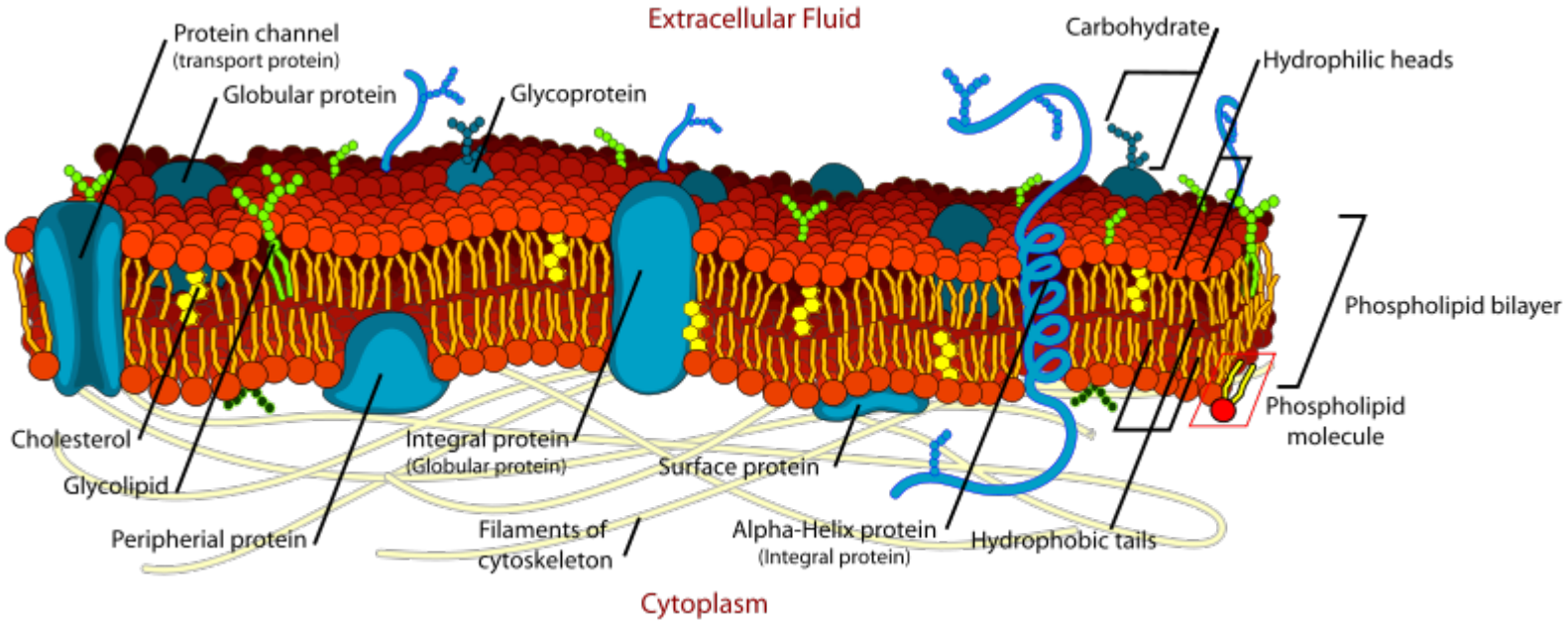

Characteristic diffusivities

Particle	Typical size	Diffusion constant
Solute ion	10^{-1} nm	2×10^3 $\mu m^2/s$
Small protein	5 nm	40 $\mu m^2/s$
Virus	100 nm	2 $\mu m^2/s$
Bacterium	1 μm	0.2 $\mu m^2/s$
Mammalian/human cell	10 μm	0.02 $\mu m^2/s$

The Nucleus

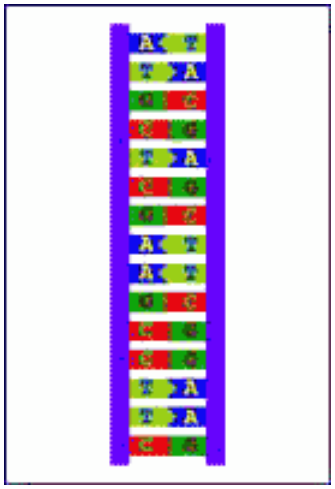

The cell factory contains a large inventory of blueprints dating all the way to its founding. Some of these blueprints are out of date, and some are for parts and products that are no longer made. Part of your job would entail sorting through everything, finding the correct blueprints, copying them, and sending the copies out to the assembly line at the correct time.

Nucleus

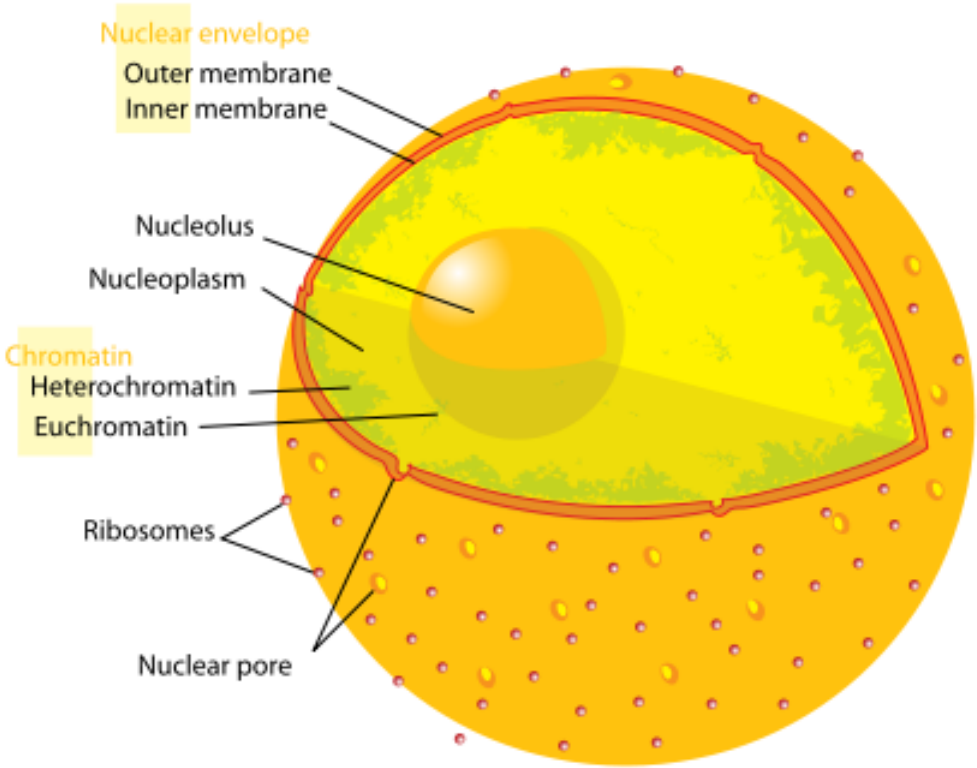

•In cell biology, the **nucleus** is a membrane-enclosed organelle found in most eukaryotic cells. It contains most of the cell's genetic material, organized as multiple long linear DNA molecules in complex with a large variety of proteins such as histones to form chromosomes. The genes within these chromosomes make up the cell's nuclear genome. The function of the nucleus is to maintain the integrity of these genes and to control the activities of the cell by regulating gene expression.

In cell biology, the **nucleolus** (plural *nucleoli*) is a "sub-organelle" of the cell nucleus, which itself is an organelle. A main function of the nucleolus is the production and assembly of ribosome components

Nuclear pores

Nuclear pores, which provide aqueous channels through the envelope, are composed of multiple proteins, collectively referred to as nucleoporins. The pores are 100 nm in total diameter; however, the gap through which molecules freely diffuse is only about 9 nm wide, due to the presence of regulatory systems within the center of the pore. This size allows the free passage of small water-soluble molecules while preventing larger molecules, such as nucleic acids and proteins, from inappropriately entering or exiting the nucleus. These large molecules must be actively transported into the nucleus instead. The nucleus of a typical mammalian cell will have about 3000 to 4000 pores throughout its envelope

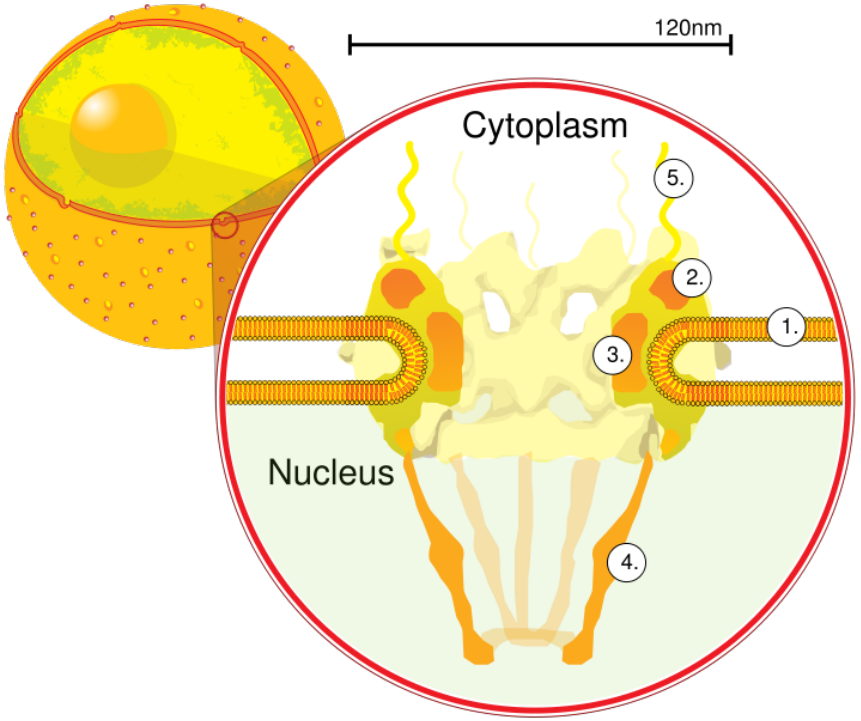

Nuclear localizing sequence (NLS)

- A **nuclear localizing sequence** (**NLS**) is an amino acid sequence which acts like a 'tag' on the exposed surface of a protein. This sequence is used to confine the protein to the cell nucleus through the **Nuclear Pore Complex** and to direct a newly synthesized protein into the nucleus via its recognition by cytosolic nuclear transport receptors. Typically, this signal consists of a few short sequences of positively charged lysines or arginines. Typically the NLS will have a sequence (NH2)-Pro-Pro-Lys-Lys-Lys-Arg-Lys-Val-(COOH).

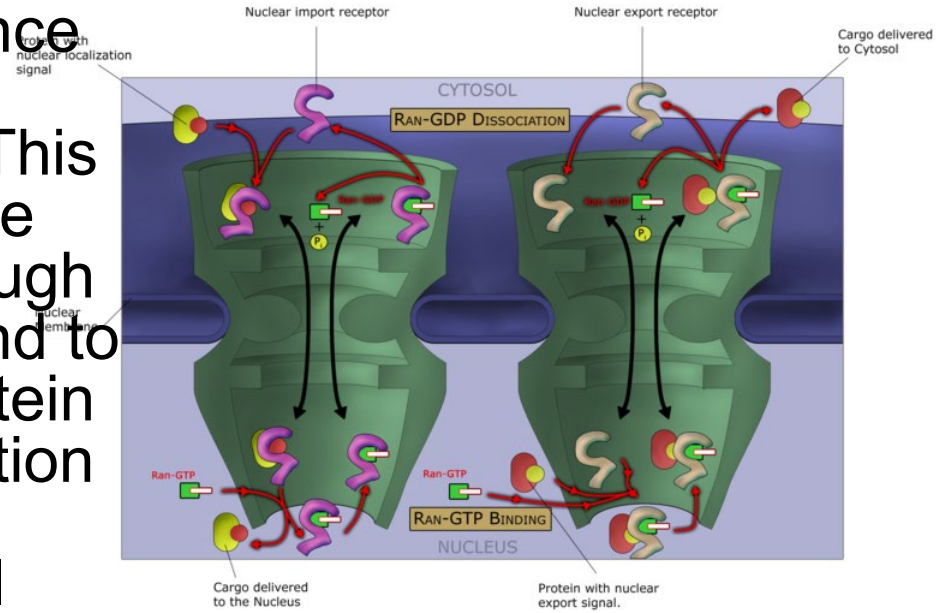

The Ribosomes and the ER

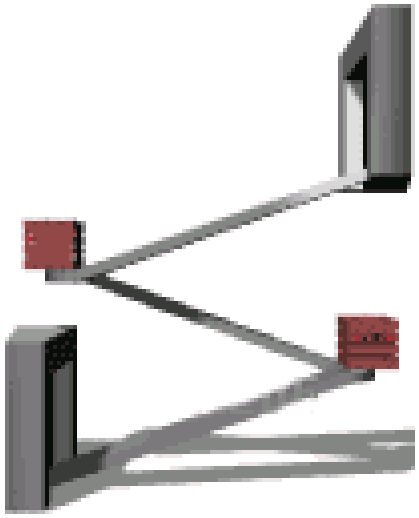

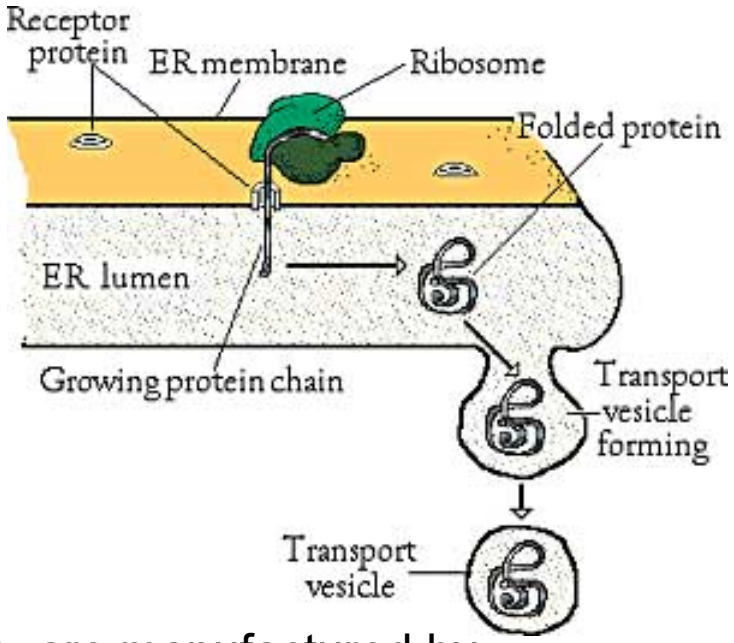

Ribosomes, the workers that build proteins, are manufactured by the nucleolus. They consist of two separate subunits: a large, lower subunit and a small, upper subunit. Ribosomes attach to the rough ER . Now let's take a look at how final processing occurs

The cell has its own assembly line and workers. Within the cytoplasm is a series of large, flattened membranes that fold back and forth on each other and have a very large surface area. This collection of membranes is called the **ENDOPLASMIC RETICULUM**, or**ER**.

Ribosome

A **ribosome** is a small, dense organelle in cells that assembles proteins. Ribosomes are about 20nm in diameter and are composed of 65% ribosomal RNA and 35% ribosomal proteins (known as a Ribonucleoprotein or RNP). It translates messenger RNA (mRNA) to build a polypeptide chain (e.g., a protein) using amino acids delivered by Transfer RNA (tRNA). It can be thought of as a giant enzyme that builds a protein from a set of genetic instructions. Ribosomes can float freely in the cytoplasm (the internal fluid of the cell) or bound to the endoplasmic reticulum, or to the nuclear envelope.

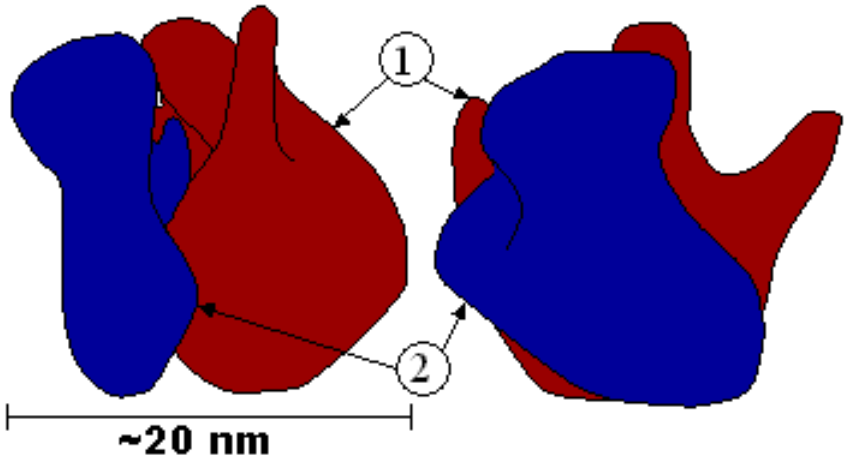

Endoplasmic Reticulum

The **endoplasmic reticulum** or **ER** is an organelle found in all eukaryotic cells that is an interconnected network of tubules, vesicles and cisternae that is responsible for several specialized functions: Protein translation, folding, and transport of proteins to be used in the cell membrane (e.g., transmembrane receptors and other integral membrane proteins), or to be secreted (exocytosed) from the cell (e.g., digestive enzymes); sequestration of calcium; and production and storage of glycogen, steroids, and other macromolecules.[1] The endoplasmic reticulum is part of the endomembrane system. The basic structure and composition of the ER membrane is similar to the plasma membrane.

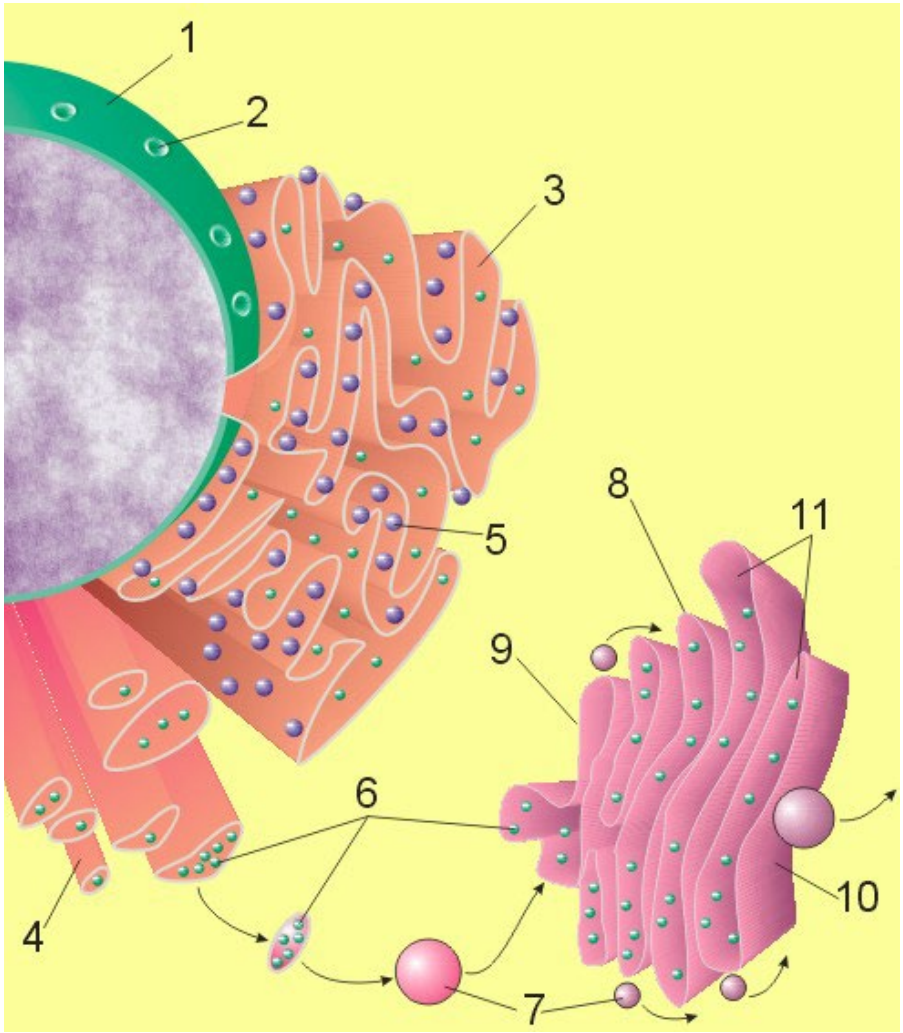

Rough endoplasmic reticulum

- The surface of the rough endoplasmic reticulum is studded with protein-manufacturing ribosomes giving it a "rough" appearance. But it should be noted that these ribosomes are not resident of the endoplasmic reticulum incessantly. The ribosomes only bind to the ER once it begins to synthesize a protein destined for sorting. The membrane of the rough endoplasmic reticulum is continuous with the outer layer of the nuclear envelope. Although there is no continuous membrane between the rough ER and the Golgi apparatus, membrane bound vesicles shuttle proteins between these two compartments. The rough endoplasmic reticulum works in concert with the Golgi complex to target new proteins to their proper destinations

Smooth endoplasmic reticulum

- The smooth endoplasmic reticulum has functions in several metabolic processes, including synthesis of lipids, metabolism of carbohydrates and calcium concentration, and attachment of receptors on cell membrane proteins. It is connected to the nuclear envelope. Smooth endoplasmic reticulum is found in a variety of cell types (both animal and plant) and it serves different functions in each. It consists of tubules and vesicles that branch forming a network. In some cells there are dilated areas like the sacs of rough endoplasmic reticulum. The network of smooth endoplasmic reticulum allows increased surface area for the action or storage of key enzymes and the products of these enzymes. The smooth endoplasmic reticulum is known for its storage of calcium ions in muscle cells.

The Golgi Apparatus

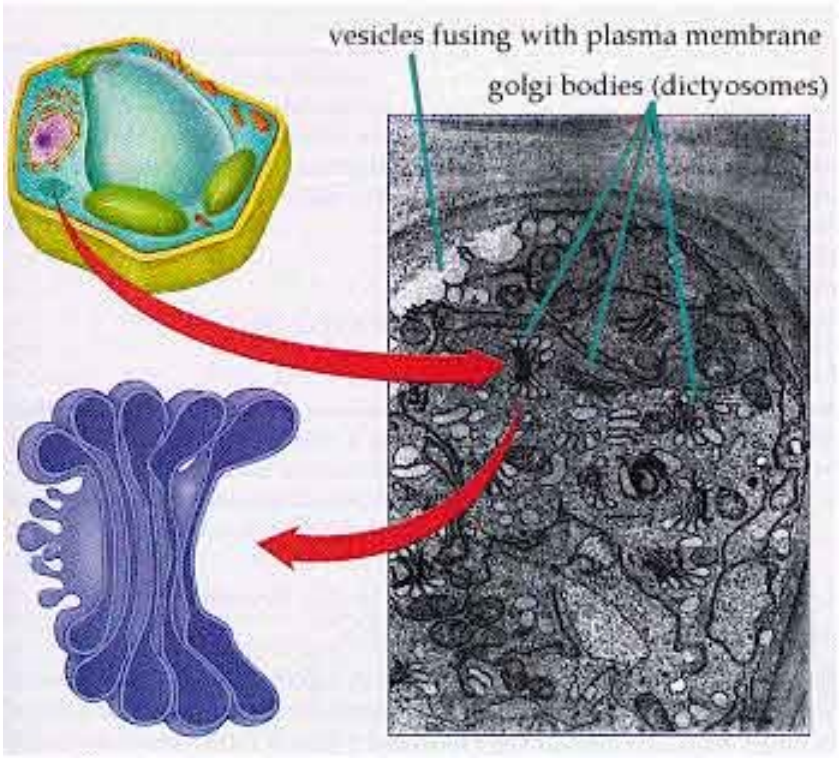

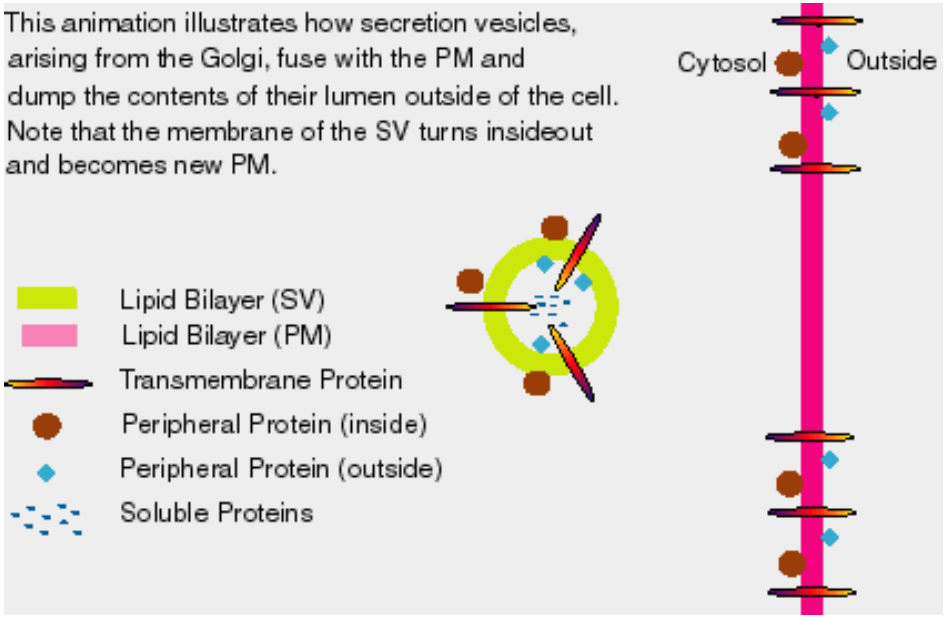

The Golgi apparatus is analogous to the finishing and packing room in a factory. Once the ribosome finishes manufacturing a protein in the rough ER, the protein needs to be prepared for use or export. Special enzymes will trim off any extra amino acids, and then the unfinished protein moves through channels in the smooth ER.

Golgi apparatus

The **Golgi apparatus** (also called the **Golgi body**, **Golgi complex**, or **dictyosome**) is an organelle found in typical eukaryotic cells. It was identified in 1898 by the Italian physician Camillo Golgi and was named after him. The primary function of the Golgi apparatus is to process and package macromolecules synthesised by the cell, primarily proteins and lipids. The Golgi apparatus forms a part of the endomembrane system present in eukaryotic cells.

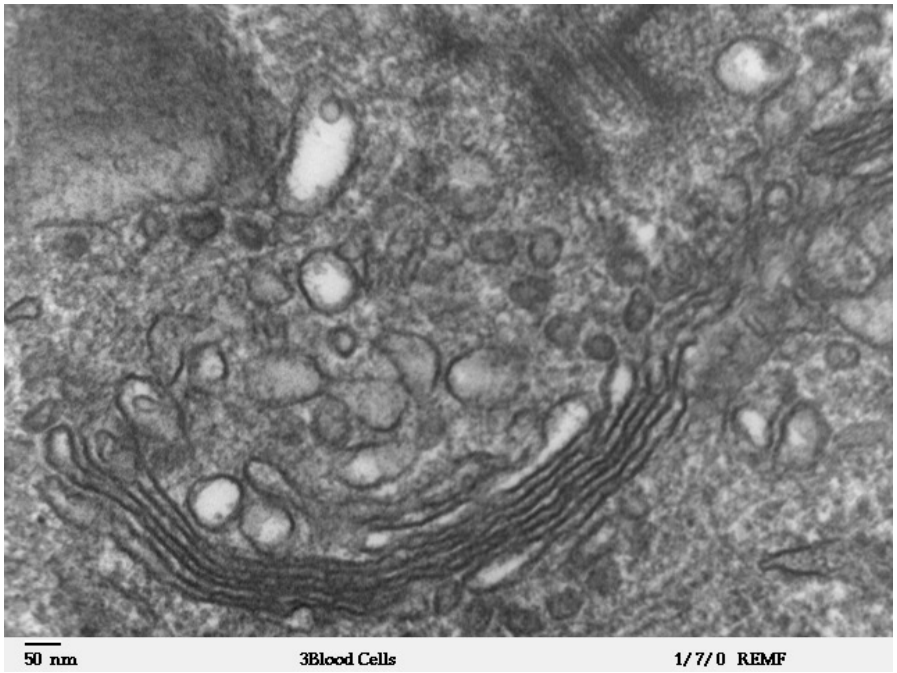

Mitochondria

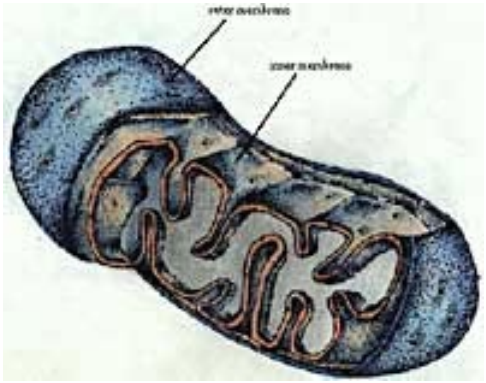

- ATP -
a Source of
ENERGY

Like our factory's power plant, mitochondria and chloroplasts transform one form of energy to another. Remember that nearly all the energy used by living things on Earth comes from the Sun. This section discusses how energy is made available for cell processes.

Mitochondrion

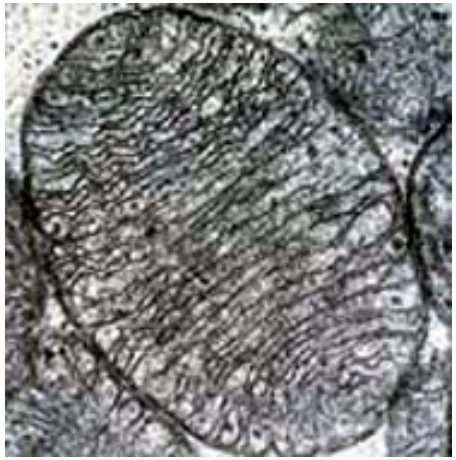

- In cell biology, a **mitochondrion** is a membrane-enclosed organelle, found in most eukaryotic cells.Mitochondria are sometimes described as "cellular power plants," because they convert NADH and NADPH into energy in the form of ATP via the process of oxidative phosphorylation. A typical eukaryotic cell contains about 2,000 mitochondria, which occupy roughly one fifth of its total volume. Mitochondria contain DNA that is independent of the DNA located in the cell nucleus. According to the endosymbiotic theory, mitochondria are descended from free-living prokaryotes.

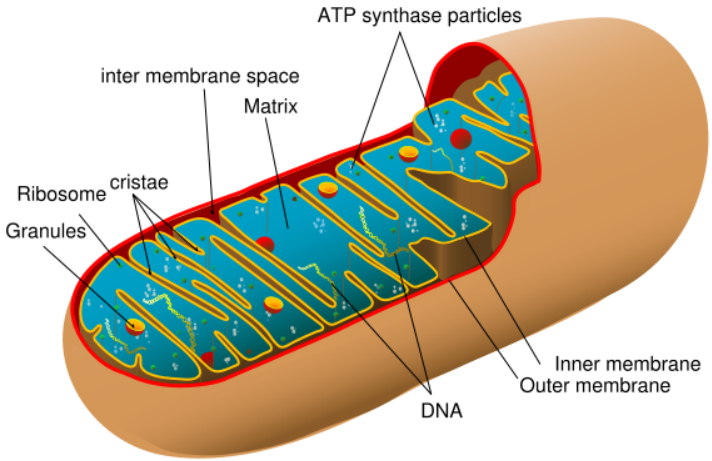

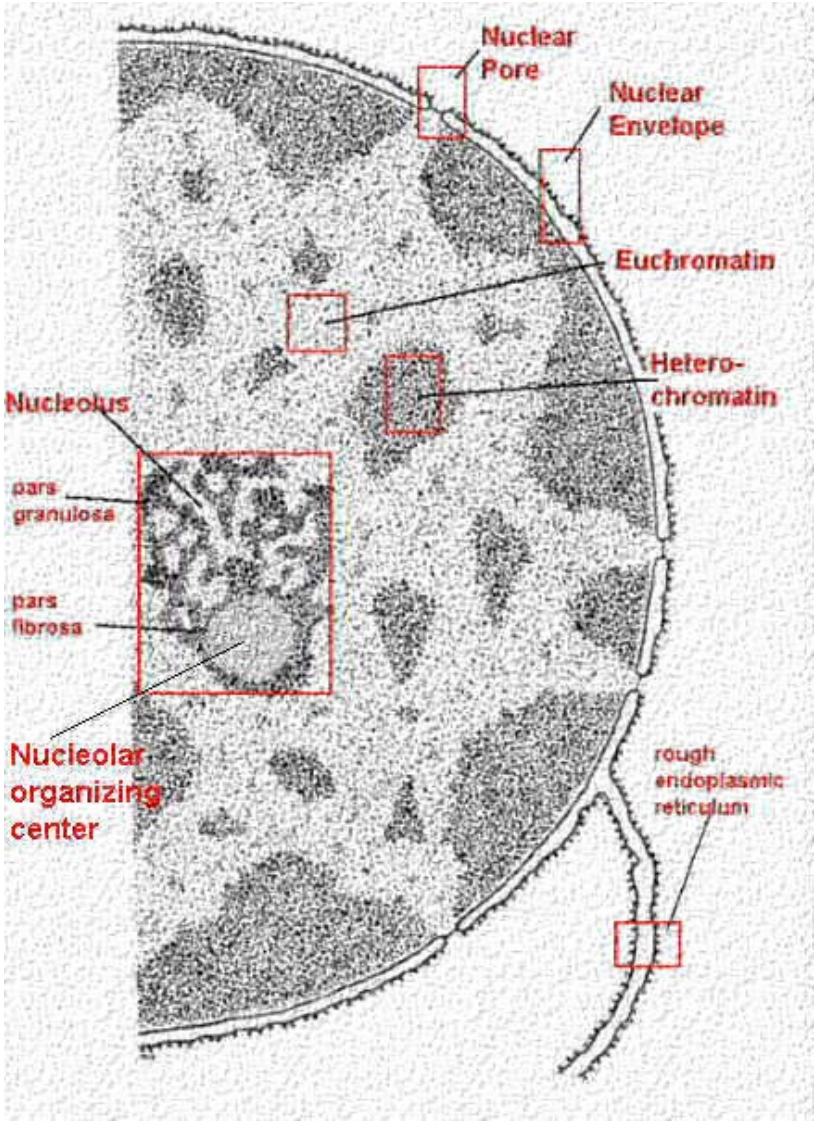

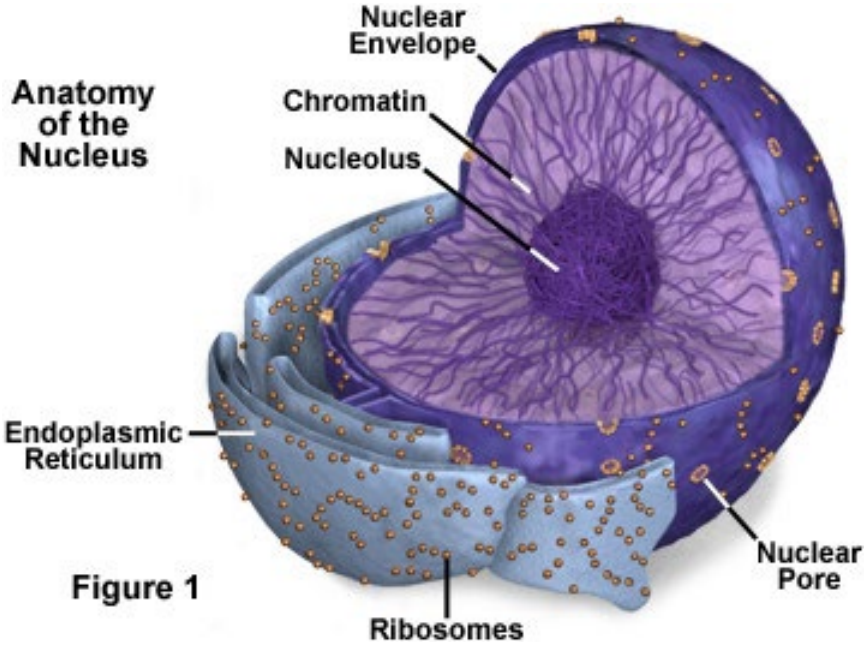

Figure 1

The main roles of the nucleolus are to synthesize rRNA and assemble ribosomes

The main function of the cell nucleus is to control gene expression and mediate the replication of DNA during the cell cycle

Lysosomes

- **Lysosomes** are organelles that contain digestive enzymes (acid hydrolases). They digest excess or worn out organelles, food particles, and engulfed viruses or bacteria. The membrane surrounding a lysosome prevents the digestive enzymes inside from destroying the cell. Lysosomes fuse with vacuoles and dispense their enzymes into the vacuoles, digesting their contents. They are built in the Golgi apparatus. The name *lysosome* derives from the Greek words *lysis*, which means dissolution or destruction, and *soma*, which means body. They are frequently nicknamed "suicide-bags" or "suicide-sacs" by cell biologists due to their role in autolysis.

Lysosomes

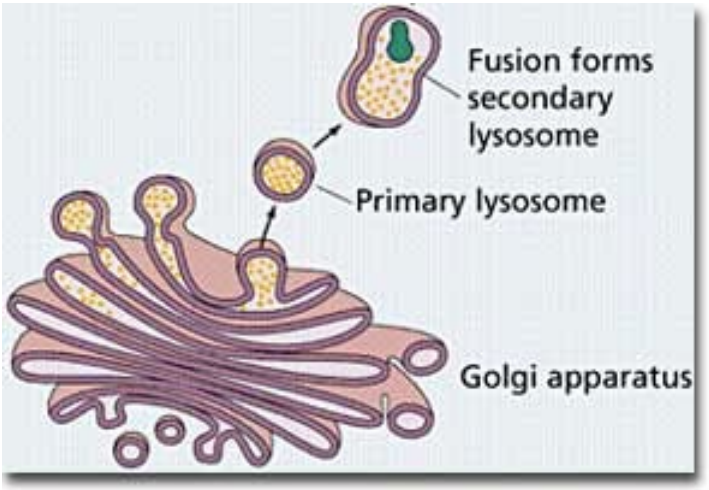

Lysosomes are responsible for the breakdown and absorption of materials taken in by the cell. Often, a cell engulfs a foreign substance through **ENDOCYTOSIS**, another form of active transport. During endocytosis, the cell membrane puckers up, forms a pouch around materials outside the cell, and pinches off to become a vesicle. If the contents need to be destroyed, lysosomes combine with the vesicle and release their enzymes.

Lysosome

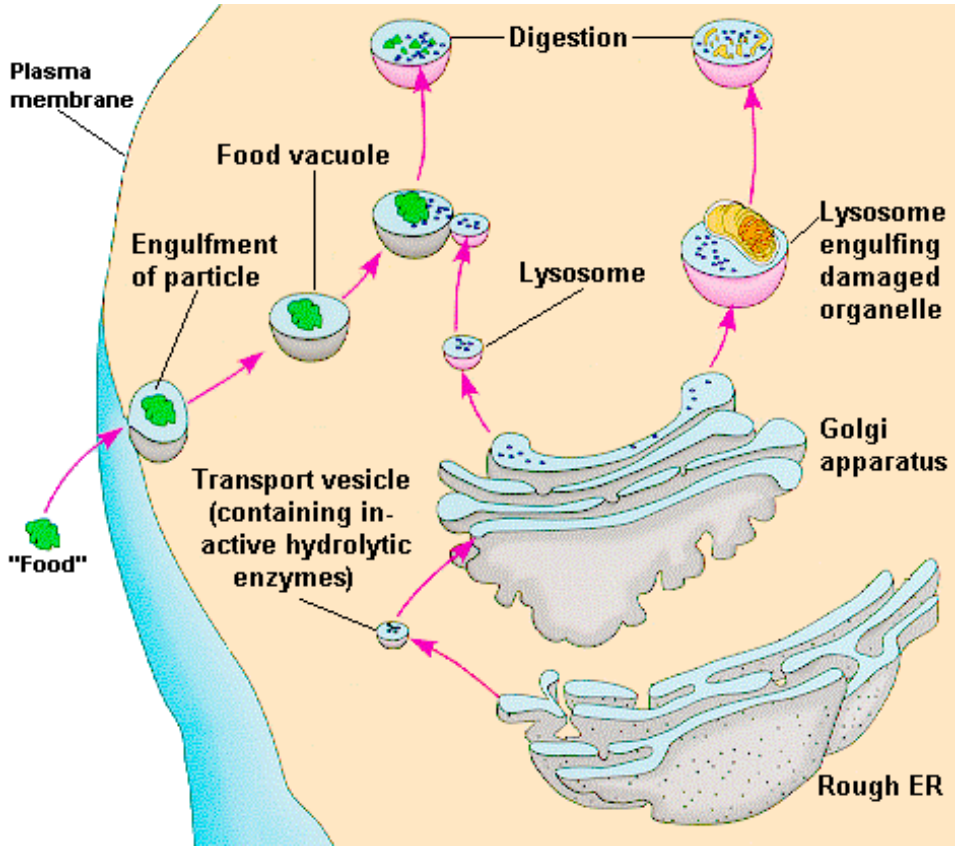
Digestion
Plasma membrane
Food vacuole
Engulfment of particle
Lysosome
Lysosome engulfing damaged organelle
Golgi apparatus
Transport vesicle (containing in-active hydrolytic enzymes)
"Food"
Rough ER

Vesicle

In cell biology, a **vesicle** is a relatively small and enclosed compartment, separated from the cytosol by at least one lipid bilayer. If there is only one lipid bilayer, they are called *unilamellar* vesicles; otherwise they are called *multilamellar*. Vesicles store, transport, or digest cellular products and waste.

This biomembrane enclosing the vesicle is similar to that of the plasma membrane. Because it is separated from the cytosol, the intravesicular environment can be made to be different from the cytosolic environment. Vesicles are a basic tool of the cell for organizing metabolism, transport, enzyme storage, as well as being chemical reaction chambers. Many vesicles are made in the Golgi apparatus, but also in the endoplasmic reticulum, or are made from parts of the plasma membrane.

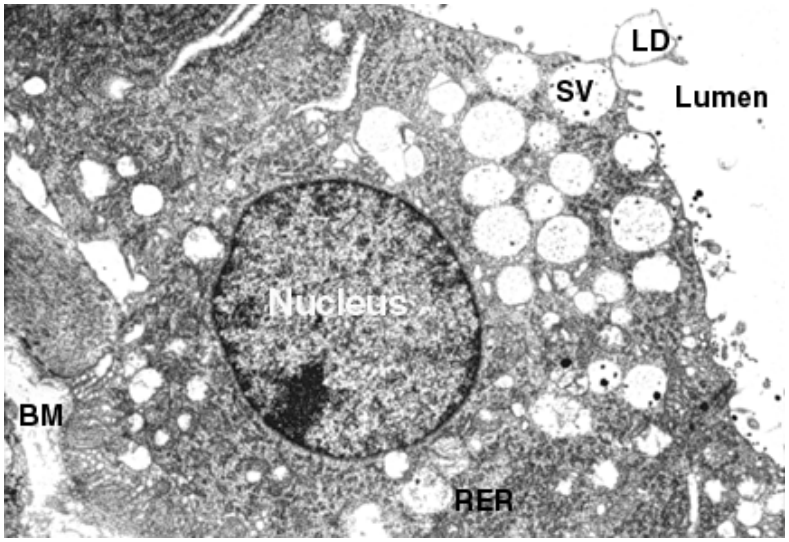

Cytoskeleton

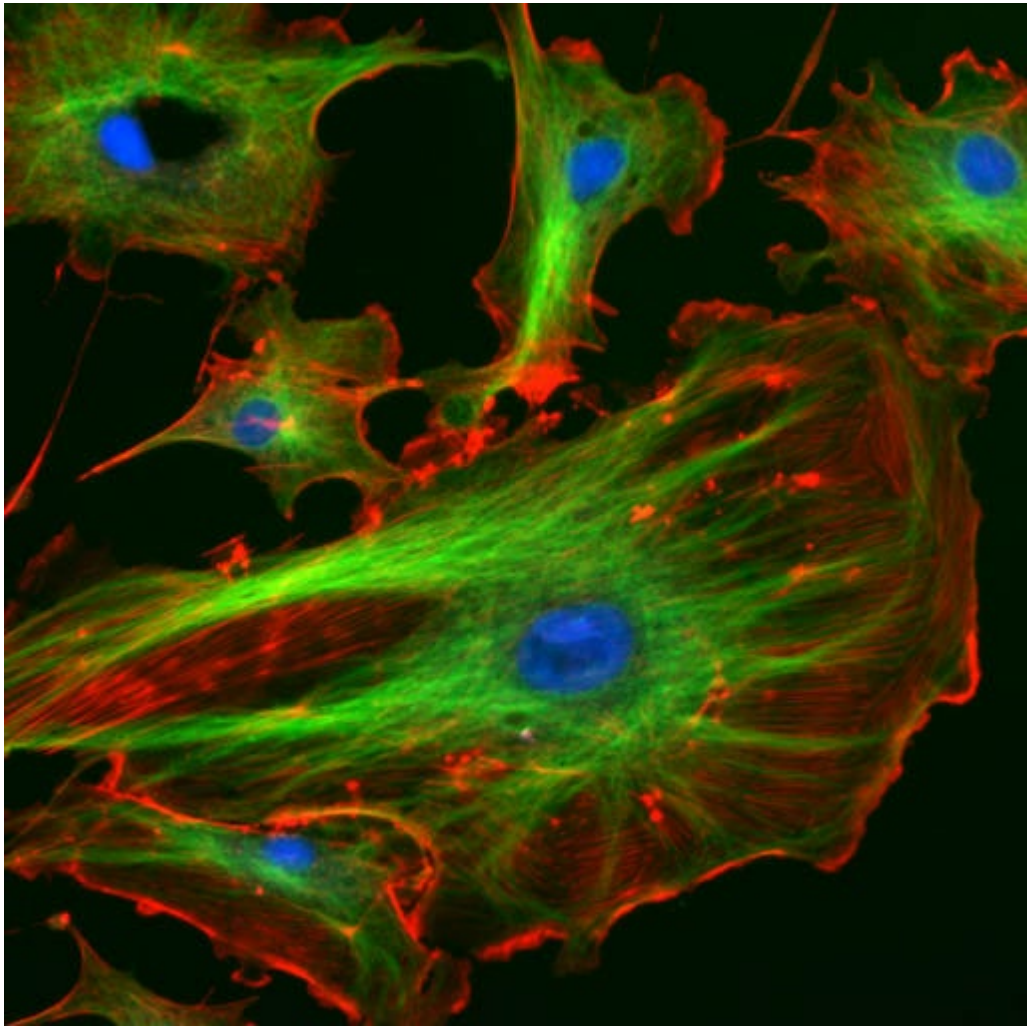

The eukaryotic cytoskeleton. Actin filaments are shown in red, microtubules in green, and the nuclei are in blue.

Actin

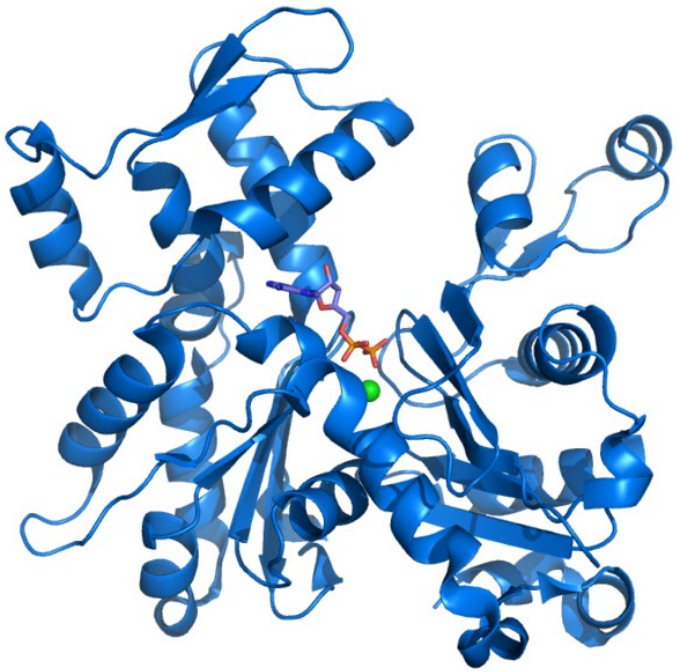

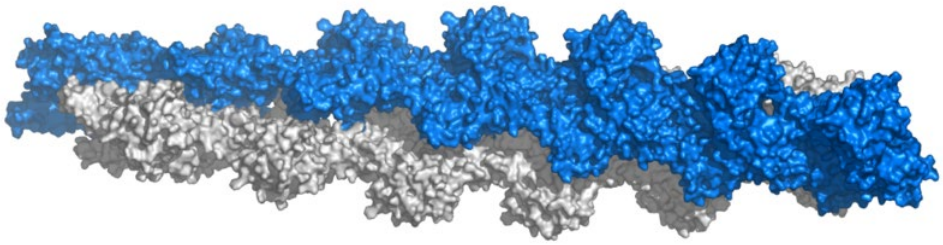

- **Actin** is a globular structural, 42 kDa, protein that polymerizes in a helical fashion to form **actin filaments** (or **microfilaments**). These form the cytoskeleton, a three-dimensional network inside the eukaryotic cell. Actin filaments provide mechanical support for the cell, determine its shape, and enable movement of the cell through lamellipodia, filopodia, or pseudopodia. Actin filaments, along with myosin, have an essential role in muscular contraction. In the cytosol, actin is predominantly bound to ATP, but can also bind to ADP. An ATP-actin complex polymerizes faster and dissociates slower than an ADP-actin complex.

Lamellipodia

- The **lamellipodium** is a cytoskeletal actin projection on the mobile edge of the cell. It contains a two-dimensional actin mesh; the whole structure pulls the cell across a substrate. Within the lamellipodia are ribs of actin called microspikes, which, when they spread beyond the lamellipodium frontier, are called filopodia (Small, et all, 2002). The lamellipodium is born of actin nucleation in the plasma membrane of the cell (Alberts, et al, 2002) and is the primary area of actin incorporation or microfilament formation of the cell. Lamellipodia range from 1µm to 5µm in breadth and are approximately 0.2µm thick.Lamellipodia are found primarily in very mobile cells, crawling at a speeds of 10-20µm/minute over epithelial surfaces..
- The tip of the lamellipodium is the site where exocytosis occurs in migrating mammalian cells as part of their clathrin-mediated endocytic cycle.

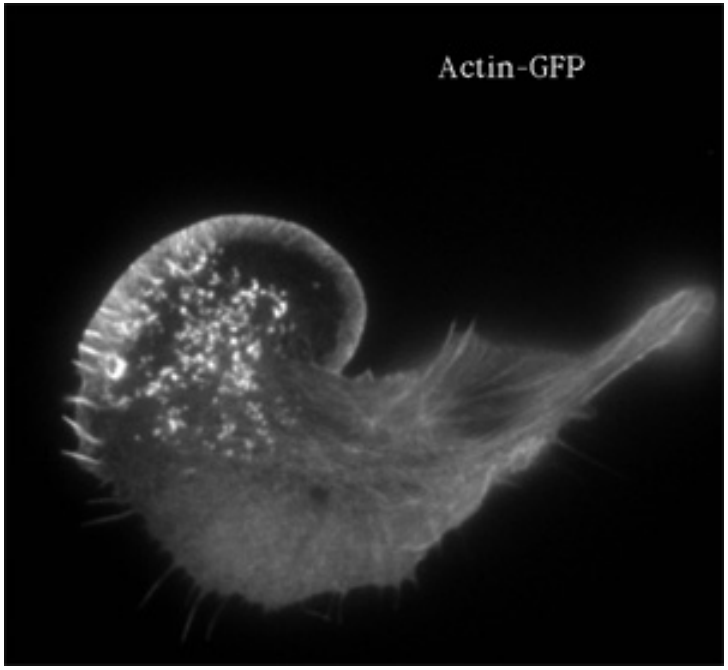

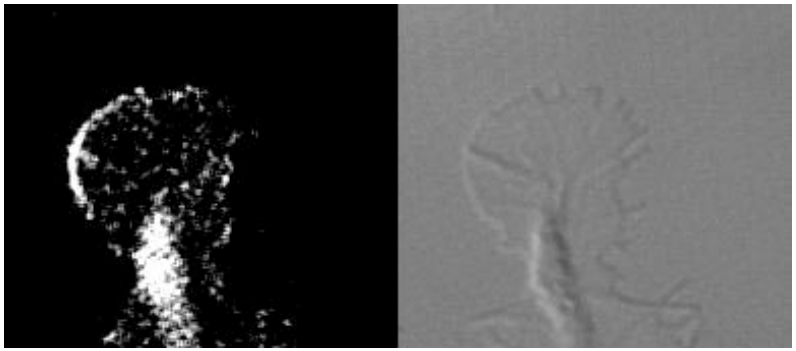

http://www.microscopyu.com/moviegallery/livecellimaging/3t3/t1/3t3-dslwmp1.html

Filopodia

The **filopodia** are slender cytoplasmic projections, similar to lamellipodia, which extend from the leading edge of migrating cells. They contain actin filaments cross-linked into bundles by actin-binding proteins, e.g. fimbrin. Filopodia form focal adhesions with the substratum, linking it to the cell surface. A cell migrates along a surface by extending filopodia at the leading edge. The filopodia attach to the substratum further down the migratory pathway, then contraction of stress fibres retracts the rear of the cell to move the cell forwards.

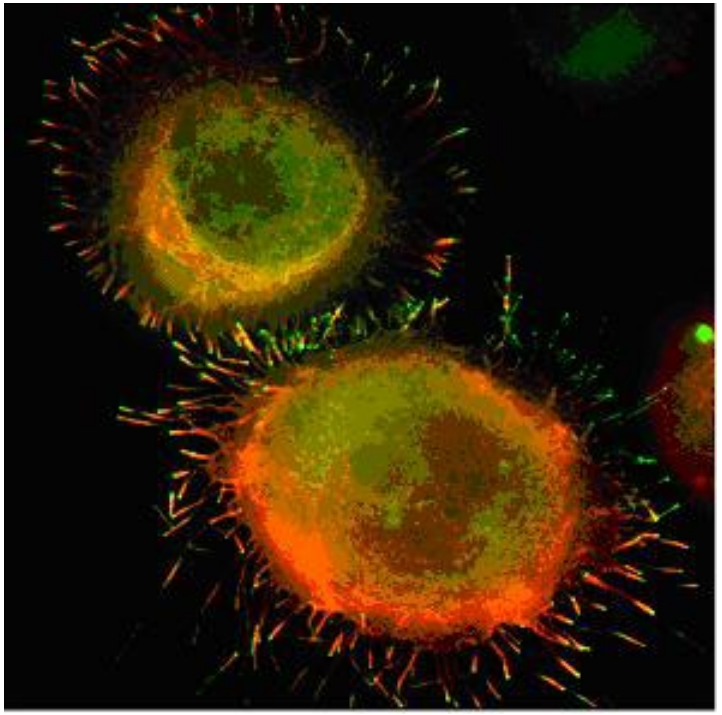

Focal adhesion

- In cell biology, '**Focal Adhesions'** are specific types of large macromolecular assemblies through which both mechanical force and regulatory signals are transmitted. More precisely, **FAs** can be considered as sub-cellular macromolecules that mediate the regulatory effects (e.g. cell anchorage) of extracellular matrix (ECM) adhesion on cell behavior.

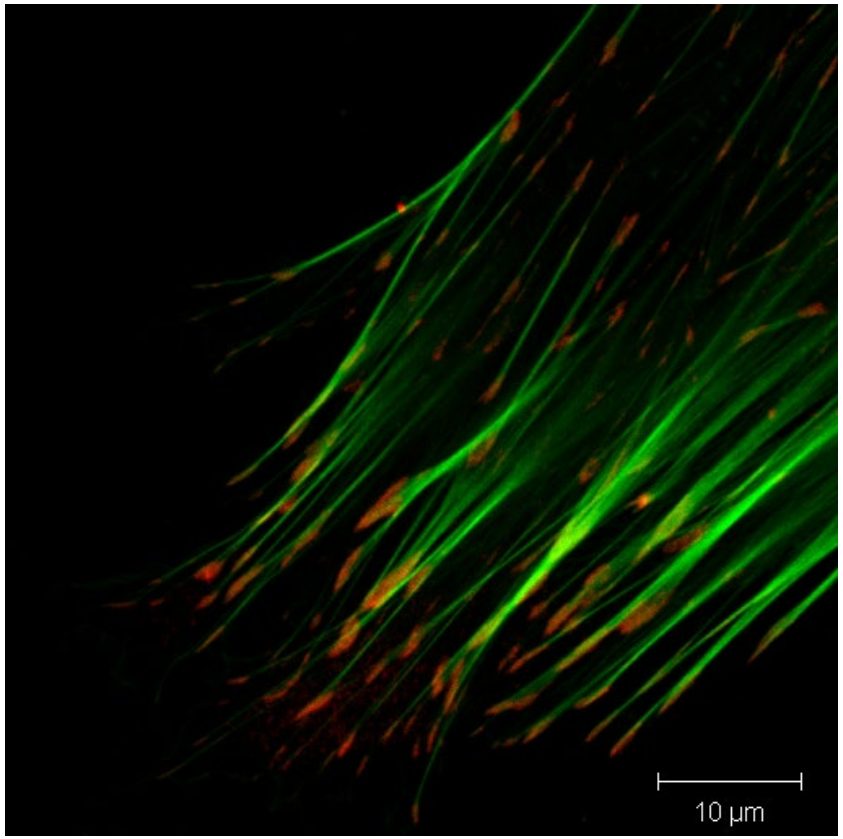

Extra Cellular Matrix

The ECM's main components are various glycoproteins, proteoglycans and hyaluronic acid. In most animals, the most abundant glycoproteins in the ECM are collagens.

ECM also contains many other components: proteins such as fibrin, elastin, fibronectins, laminins, and nidogens, and minerals such as hydroxylapatite, or fluids such as blood plasma or serum with secreted free flowing antigens.

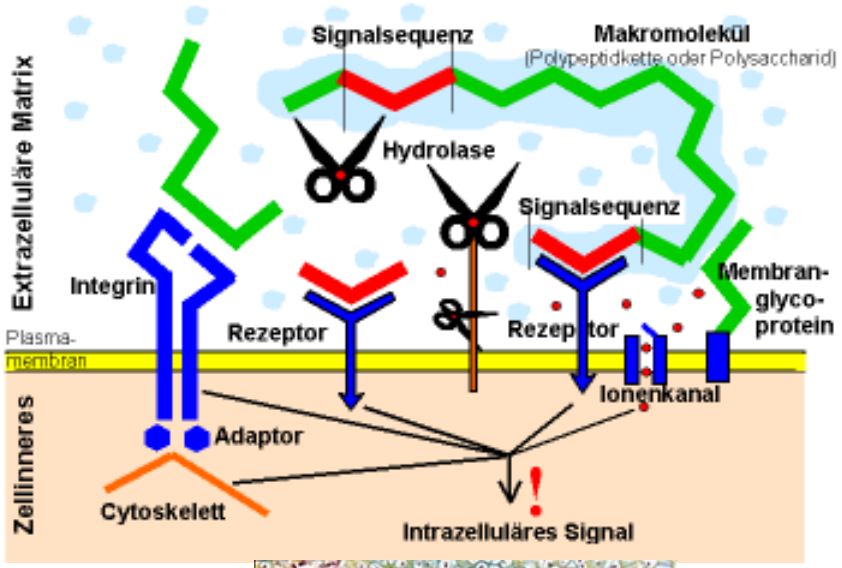

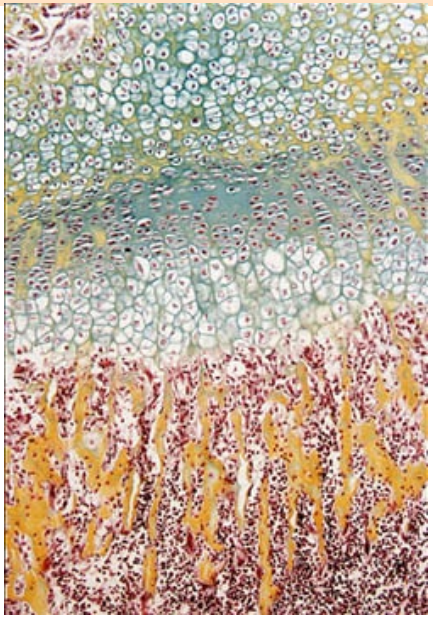

Integrin

An **integrin**, or **integrin receptor**, is an integral membrane protein in the plasma membrane of cells. It plays a role in the attachment of a cell to the extracellular matrix (ECM) and to other cells, and in signal transduction from the ECM to the cell. There are many types of integrin, and many cells have multiple types on their surface. Integrins are of vital importance to all metazoans, from humans to sponges.

Schematic drawing of a typical integrin dimer

Arrow shows the region where an I domain is inserted in some α subunits. Not all α subunits are posttranslationally cleaved. Internal disulphide bonds within subunits are not shown. Dark blue regions in the head segment of the α subunit represent homologous repeats. Those with the EF-hand consensus sequence are marked with red circles to denote binding sites for divalent metal ion.

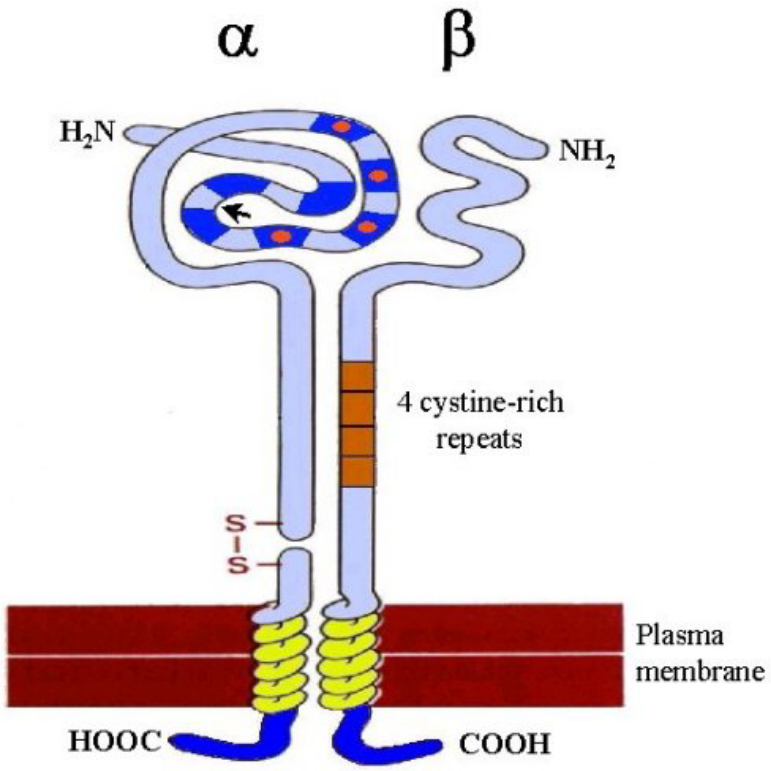

Endocytosis

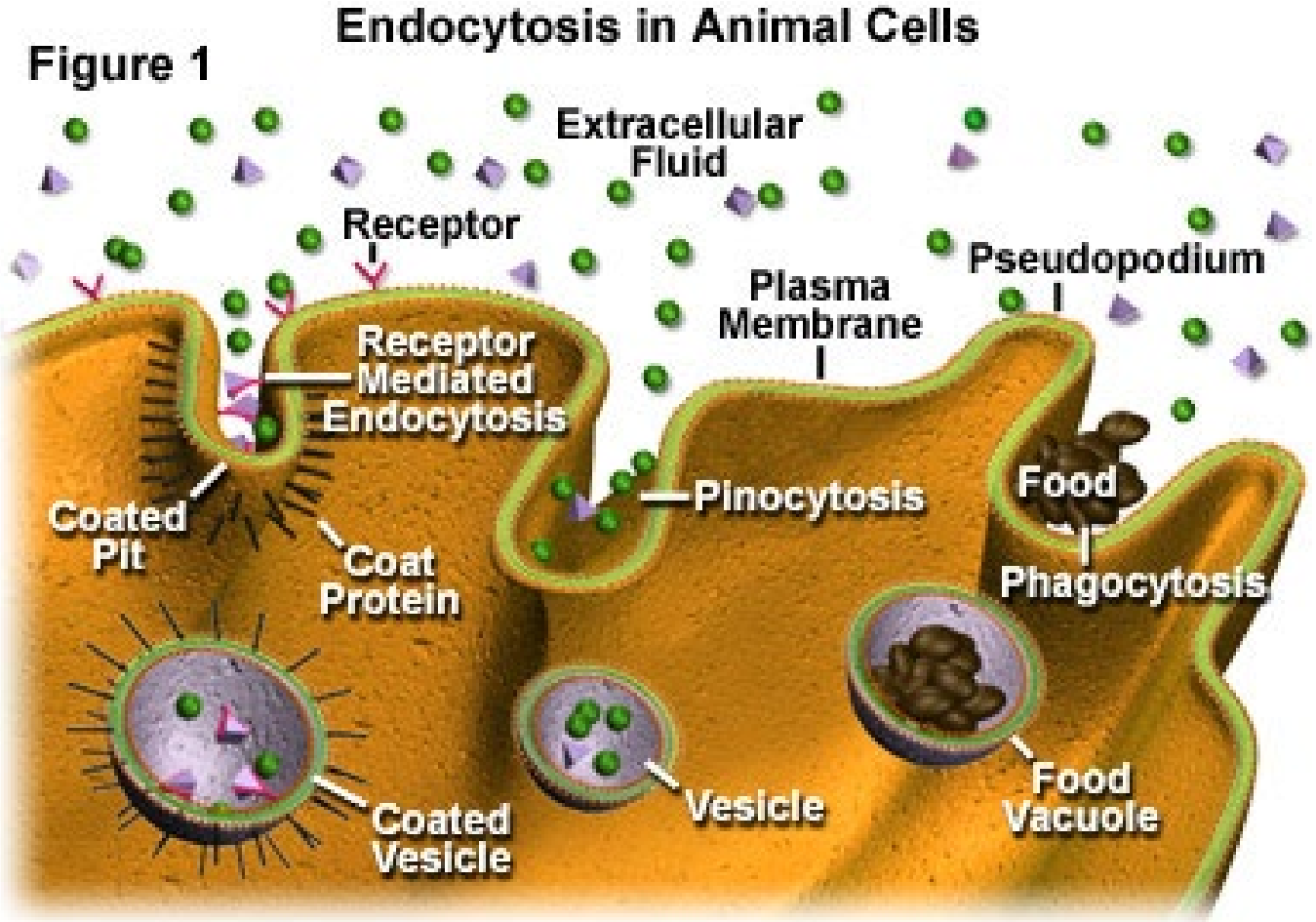

Super-Resolution Microscopy

Nanoscopy

The Nobel Prize in Chemistry 2014

Photo: Matt Staley/HHMI

Eric Betzig

Prize share: 1/3

© Bernd Schuller, Max-Planck-Institut

Stefan W. Hell

Prize share: 1/3

Photo: K. Lowder via Wikimedia Commons, CC-BY-SA-3.0

William E. Moerner

Prize share: 1/3

The Nobel Prize in Chemistry 2014 was awarded jointly to Eric Betzig, Stefan W. Hell and William E. Moerner *"for the development of super-resolved fluorescence microscopy"*.

Two separate principles are rewarded. One enables the method *stimulated emission depletion (STED) microscopy,* developed by Stefan Hell in 2000.

Eric Betzig and William Moerner, working separately, laid the foundation for the second method, *single-molecule microscopy*.

Microscope

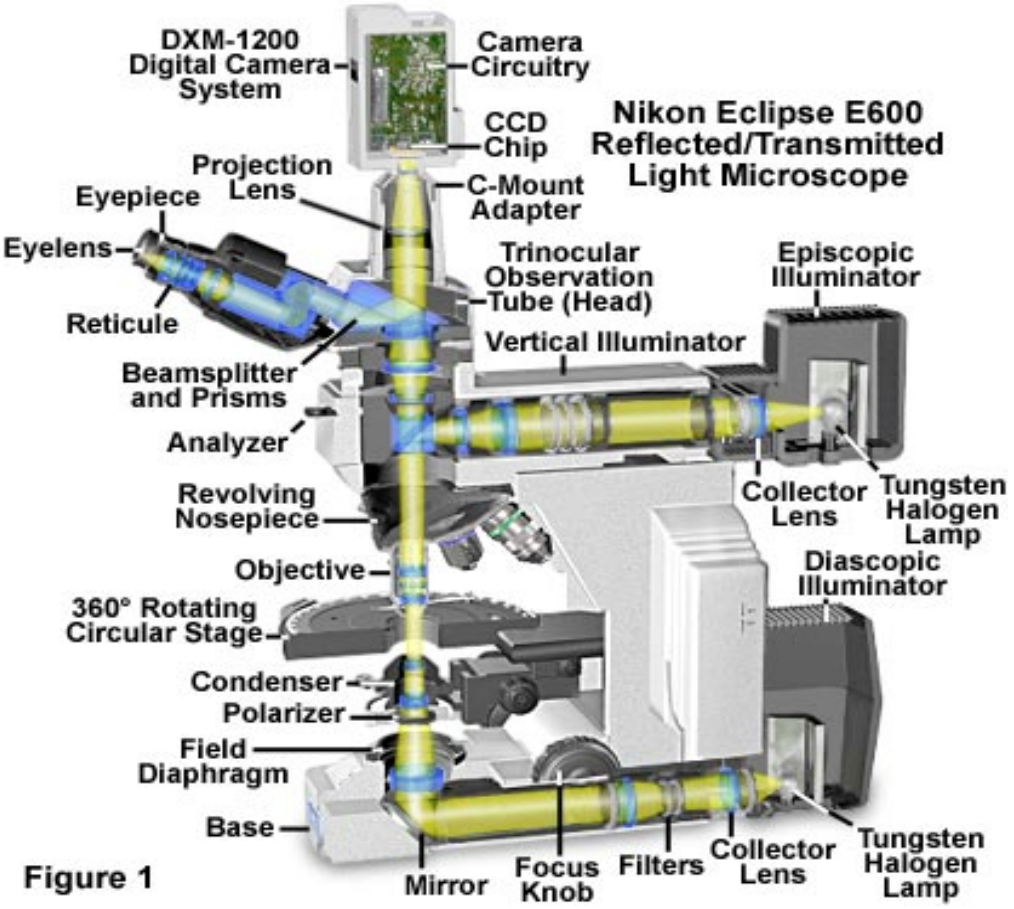

Figure 1

Resolution

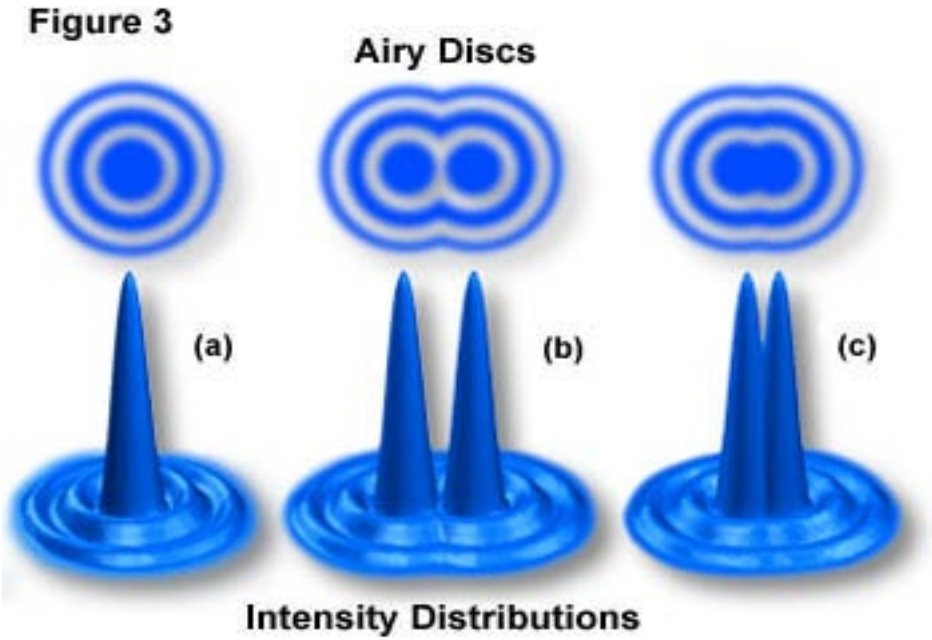

Resolution (r) = λ/(2NA) (1)

Resolution (r) = 0.61λ/NA (2)

Resolution (r) = 1.22λ/(NA(obj) + NA(cond)) (3)

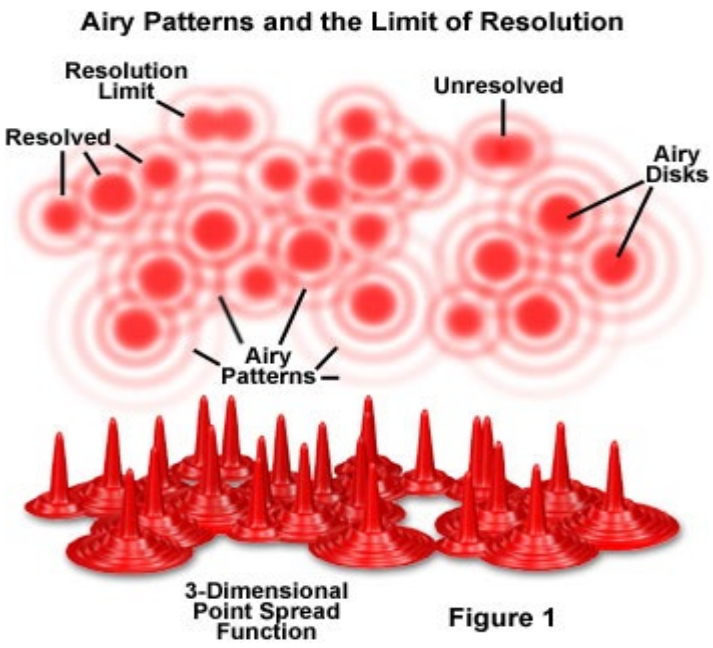

Figure 1

	Objective Type					
	Plan Achromat		Plan Fluorite		Plan Apochromat	
Magnification	N.A.	Resolution (µm)	N.A.	Resolution (µm)	N.A.	Resolution (µm)
4x	0.10	2.75	0.13	2.12	0.20	1.375
10x	0.25	1.10	0.30	0.92	0.45	0.61
20x	0.40	0.69	0.50	0.55	0.75	0.37
40x	0.65	0.42	0.75	0.37	0.95	0.29
60x	0.75	0.37	0.85	0.32	0.95	0.29
100x	1.25	0.22	1.30	0.21	1.40	0.20

N.A. = Numerical Aperture

Resolution versus Wavelength

Wavelength (Nanometers)	Resolution (Micrometers)
360	.19
400	.21
450	.24
500	.26
550	.29
600	.32
650	.34
700	.37

N.A. = 0.95

Diffraction Limit

$$d = \lambda/(2n \sin \alpha)$$

$$, k_0 = 2NA/\lambda_{em}$$

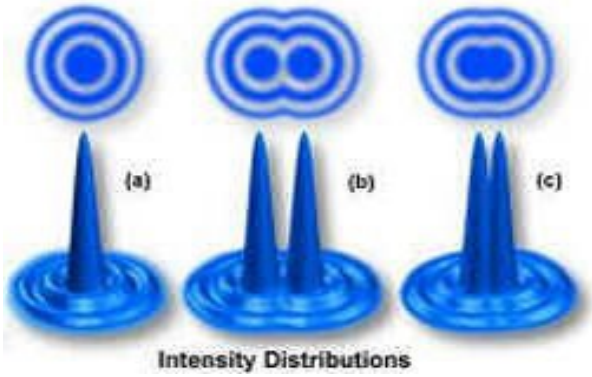

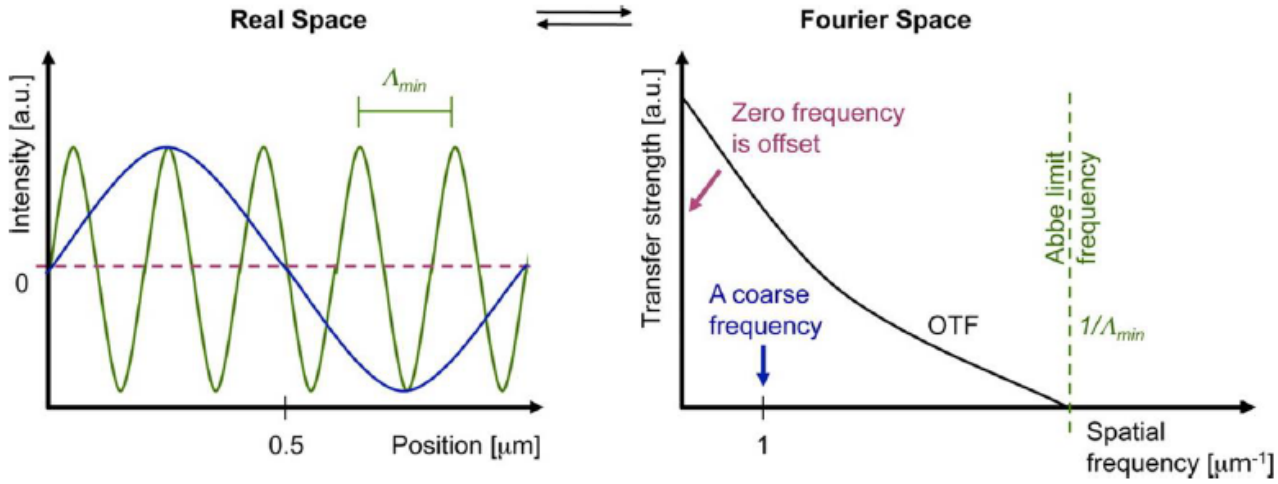

For a homogeneous medium, the solution to the homogeneous equation is of the form

$$H_\omega(k_r, z) = A^+(k_r)\,\mathrm{e}^{\mathrm{i}k_z z} + A^-(k_r)\,\mathrm{e}^{-\mathrm{i}k_z z} \tag{2.98}$$

with k_z being the vertical wavenumber,

$$k_z = \sqrt{k^2 - k_r^2}. \tag{2.99}$$

Since the inverse Hankel transform must be evaluated over a semi-infinite wavenumber domain, we have to choose a definition for the square root for $k_r > k$. We choose the definition

$$k_z = \begin{cases} \sqrt{k^2 - k_r^2}, & k_r \le k \\ \mathrm{i}\sqrt{k_r^2 - k^2}, & k_r > k. \end{cases} \tag{2.100}$$

Breaking the Diffraction Barrier: Super-Resolution Imaging of Cells

Bo Huang,[1] Hazen Babcock,[2] and Xiaowei Zhuang[2,3,*]

Cell *143*, December 23, 2010 ©2010 Elsevier Inc. 1047

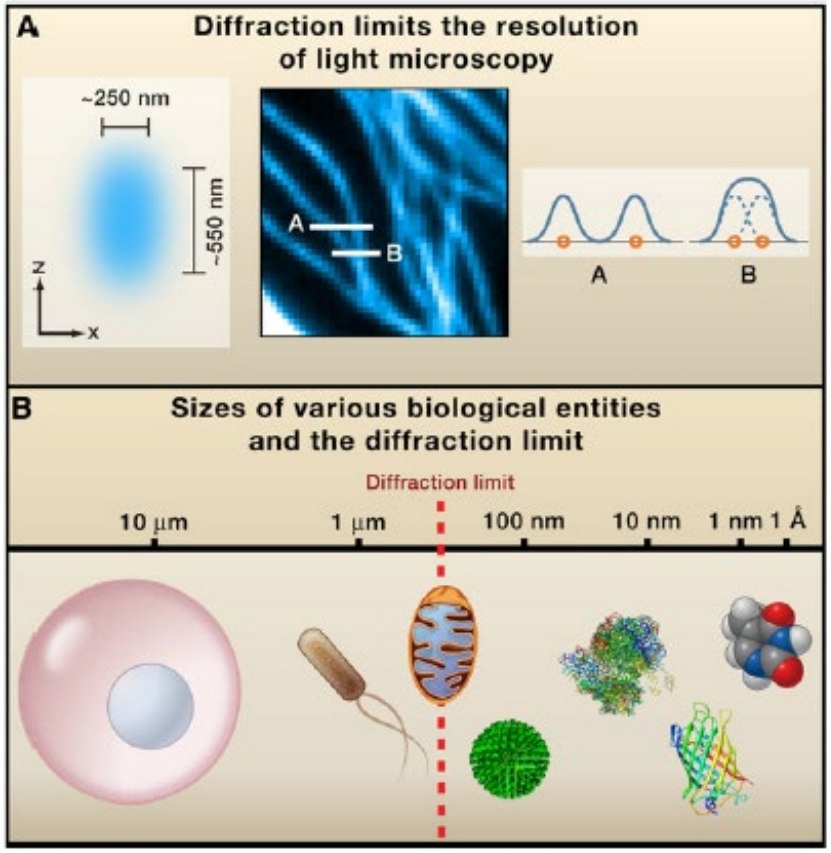

Figure 1. Diffraction-Limited Resolution of Conventional Light Microscopy

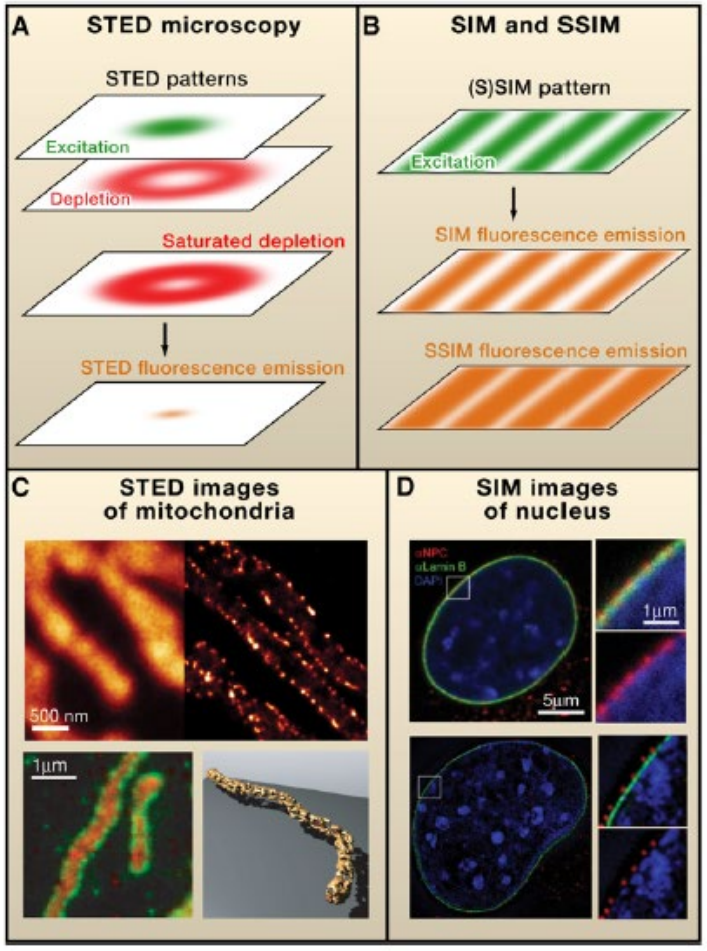

Figure 2. Super-Resolution Fluorescence Microscopy by Patterned Illumination

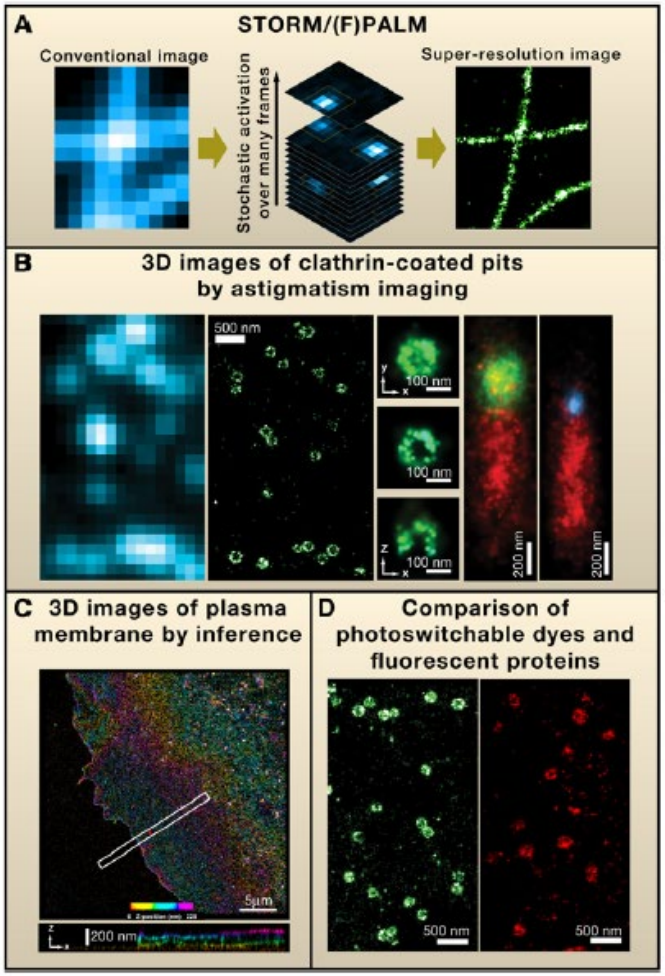

Figure 3. Super-Resolution Fluorescence Microscopy by Single-Molecule Switching

Super-Resolution Microscopy

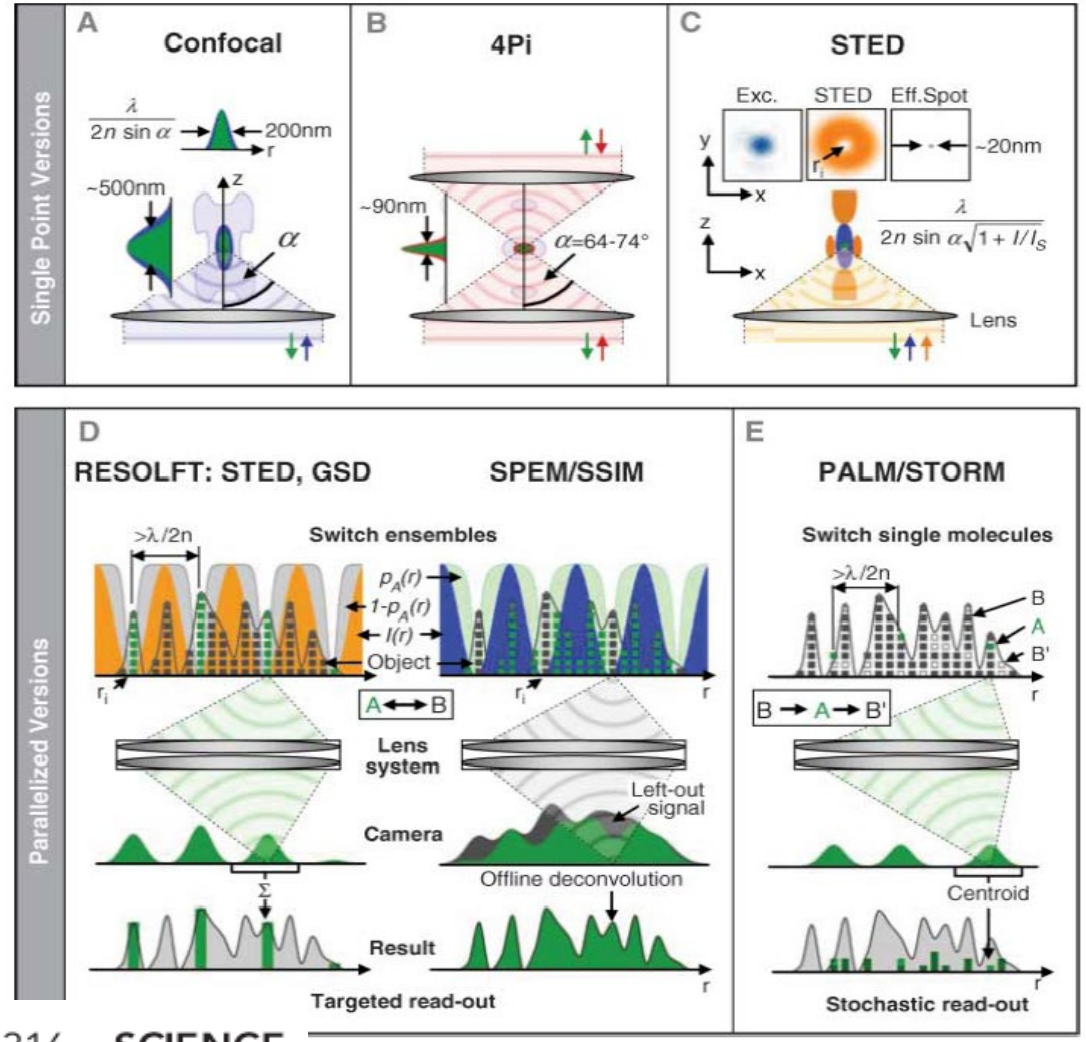

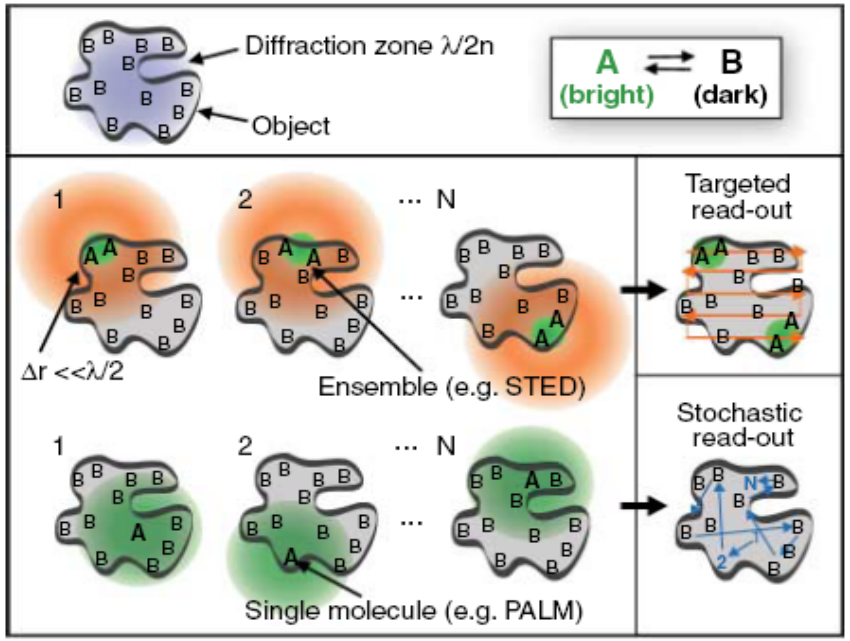

Fig. 2. Targeted versus stochastic time-sequential readout of fluorophore markers of a nanostructured object within the diffraction zone whose lower bound is given by $\lambda/2n$. A and B denote a bright and a dark state, respectively. In the targeted readout mode, one of the two states (here A) is established at a subdiffraction-sized spot at the position of a zero to read out an unknown number of fluorophore molecules. The image is assembled by deliberate translation of the zero. The zero can also be a groove. In the stochastic readout mode, a single switchable fluorophore from a random position within the diffraction zone is switched to a stable state A, while the other molecules remain in B. The coordinate is calculated from the centroid of the diffraction fluorescence spot measured by a pixelated detector. The coordinate pops up stochastically depending on where the interrogated marker molecule is located.

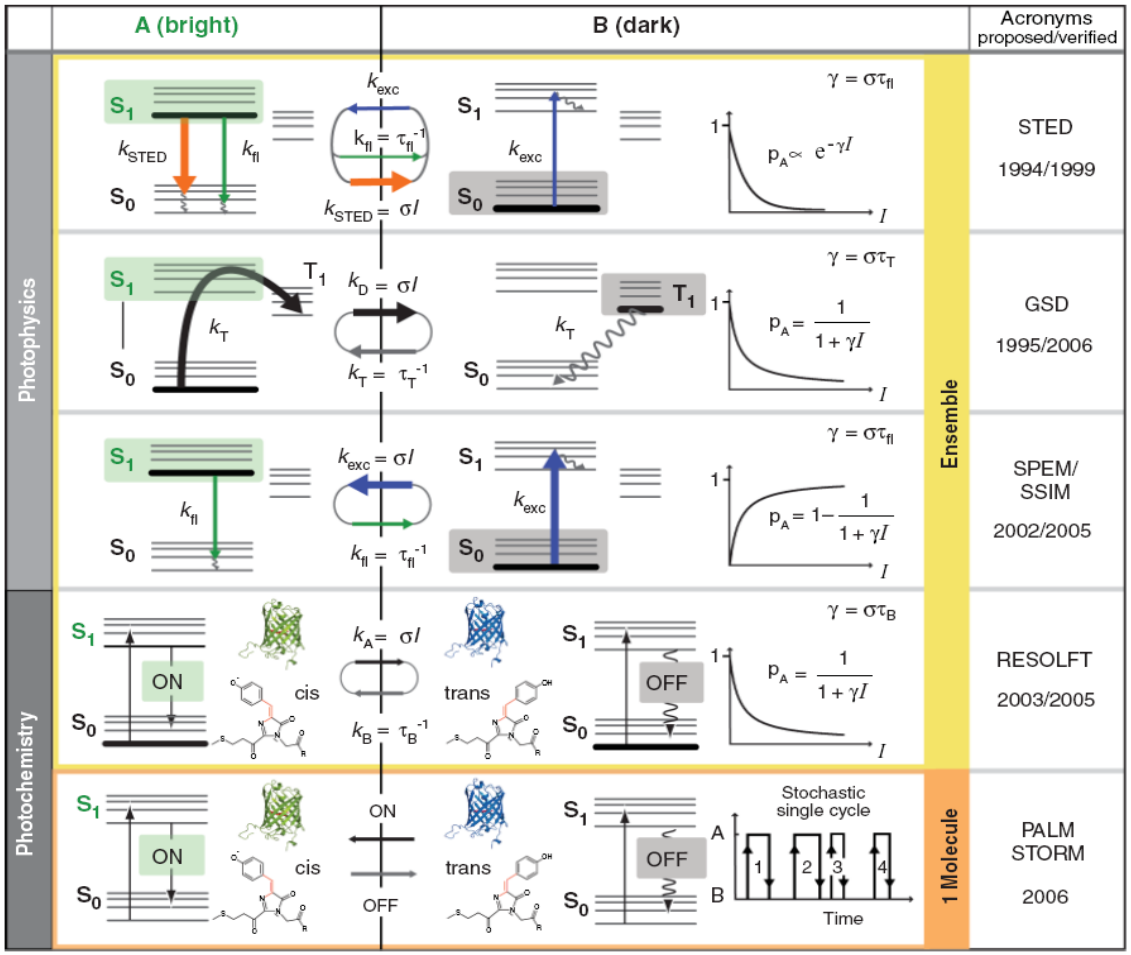

Fig. 3. Bright (**A**) and dark (**B**) molecular states used to break the diffraction barrier. Whereas STED, GSD, and SPEM utilize photophysical transitions, the photoswitching version of the RESOLFT scheme, as well as PALM and STORM, exploit photochemical transitions in which atoms are relocated or bonds formed and broken. PALM and STORM rely on measuring single (or at least identifiable) molecules at a time, whereas the other concepts, although compatible with single-molecule imaging, principally read out ensembles. Ensemble techniques rely on reversible transitions between A and B, as indicated by the rates k. The probability p_A of being in state A depends nonlinearly on the light intensity applied, as indicated by the equations, ensuring that either A or B is confined to a subdiffraction area at a targeted coordinate in space. The $e^{-\gamma I}$ and the $(1 + \gamma I)^{-1}$ dependence entail nonlinearities of infinite order $(\gamma I)^m$; $m \to \infty$. By increasing the lifetime of the chosen states, γ strengthens the nonlinear dependence of p_A, thus enabling huge nonlinearities at low I. This is radically different from m-photon processes that, depending on the concomitant action of m photons and hence just on I^m, are firmly limited to order m (*15*), which in practice is only $m < 4$. Because it operates with single molecules in a known state, the probability concept breaks down in PALM and STORM, but reminiscent of nonlinearity is the optical switching.

REversible **S**aturable **O**ptica**L** **F**luorescence **T**ransition s (RESOLFT)

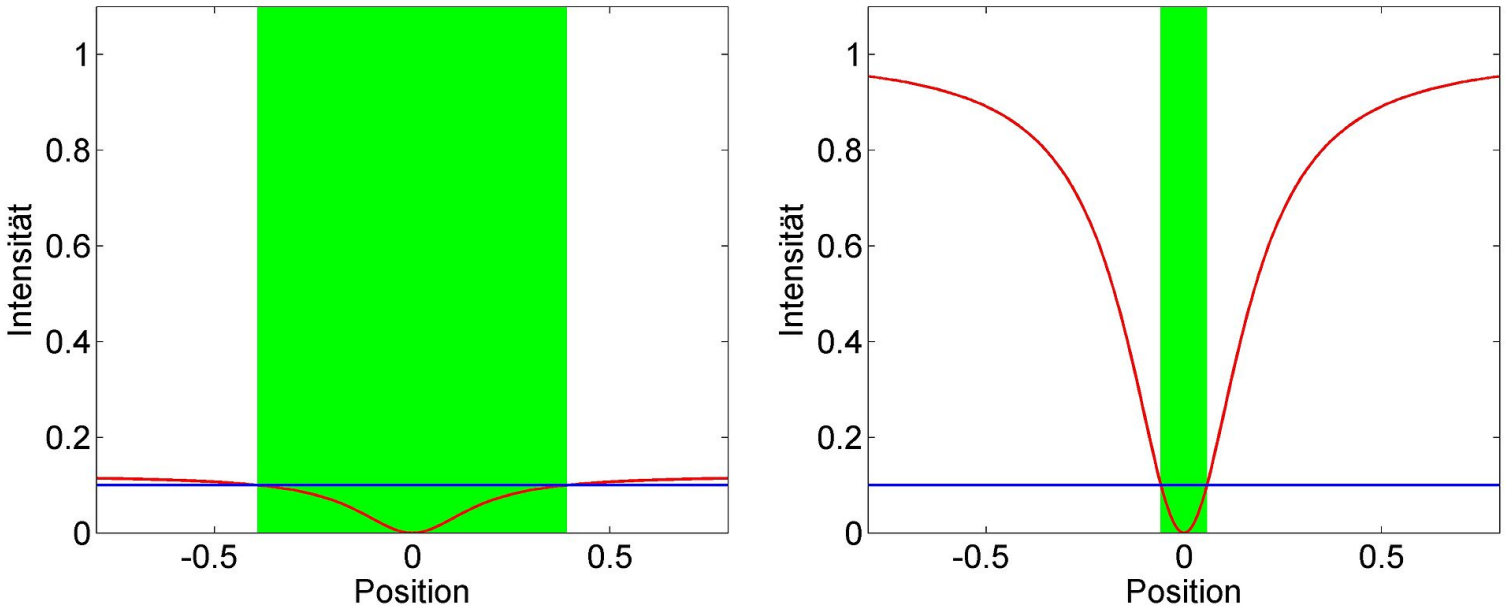

Principle of resolution increase in a RESOLFT microscope. Horizontally a spatial dimensions is drawn. The red line corresponds to the spatially variable intensity of the light beam which drives molecules from a certain state (green) to another state (white). The blue line describes the level of saturation for this transition. Increasing the brightness (right side) of the light beam one can restrict the area, where molecules can reside in their original state (green) to arbitrarily small volumes

Appl. Phys. B 60, 495–497 (1995)

Applied Physics B Lasers and Optics

Rapid communication

Ground-state-depletion fluorscence microscopy: a concept for breaking the diffraction resolution limit

S.W. Hell, M. Kroug

Department of Medical Physics, University of Turku, and Centre for Biotechnology, P.O. Box 123, FIN-20521 Turku, Finland
(Fax: +358-21/633-8000, E-mail: STEFAN.HELL@utu.fi)

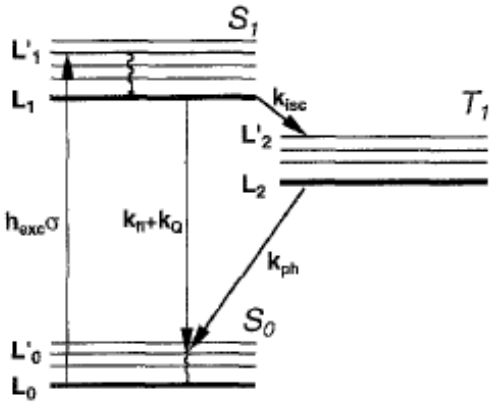

Fig. 1. Energy states of a typical dye: S_0 is the ground state, S_1 is the first singlet state, and T_1 the first triplet state

$$\frac{dn_0}{dt} = -h_{exc}\sigma n_0 + \left(k_{fl} + k_Q\right) n_1 + k_{ph} n_2 \ ,$$
$$\frac{dn_1}{dt} = +h_{exc}\sigma n_0 - \left(k_{fl} + k_Q\right) n_1 - k_{isc} n_1 \ ,$$
$$\frac{dn_2}{dt} = +k_{isc} n_1 - k_{ph} n_2 \ ,$$

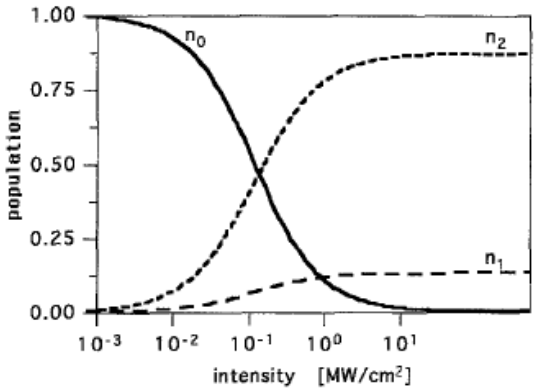

Fig. 2. The population probability of the ground state (n_0), the first singlet state (n_1), and the triplet state (n_2) as a function of the excitation intensity for fluoresceine

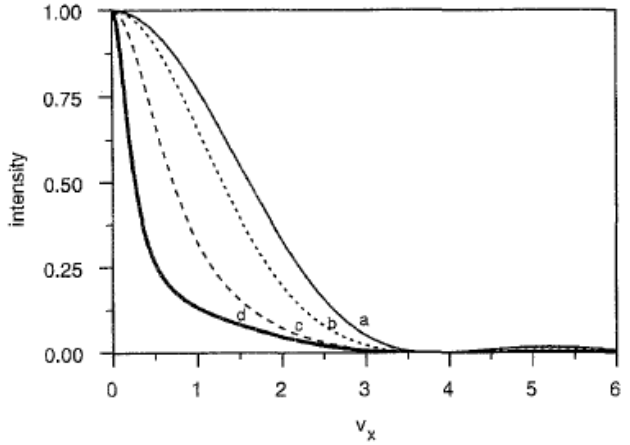

Fig. 4. Calculated effective point-spread function along the axis of the offset for peak intensities of (*b*) 0.01, (*c*) 0.1, and (*d*) 1 MW/cm^2 of the depletion beam as calculated for fluorescein, compared with the point-spread function of a classical scanning fluorescence microscope

tion, as shown in Fig. 5. A comparison of the point-spread-function obtained for a focal intensity of 1 MW/cm^2 with that of a classical scanning fluorescence microscope shows an increase in resolution by a factor of 11. Assuming an excitation wavelength of 400 nm and a numerical aperture of 1.4, one obtains a lateral FWHM of about 15 nm.

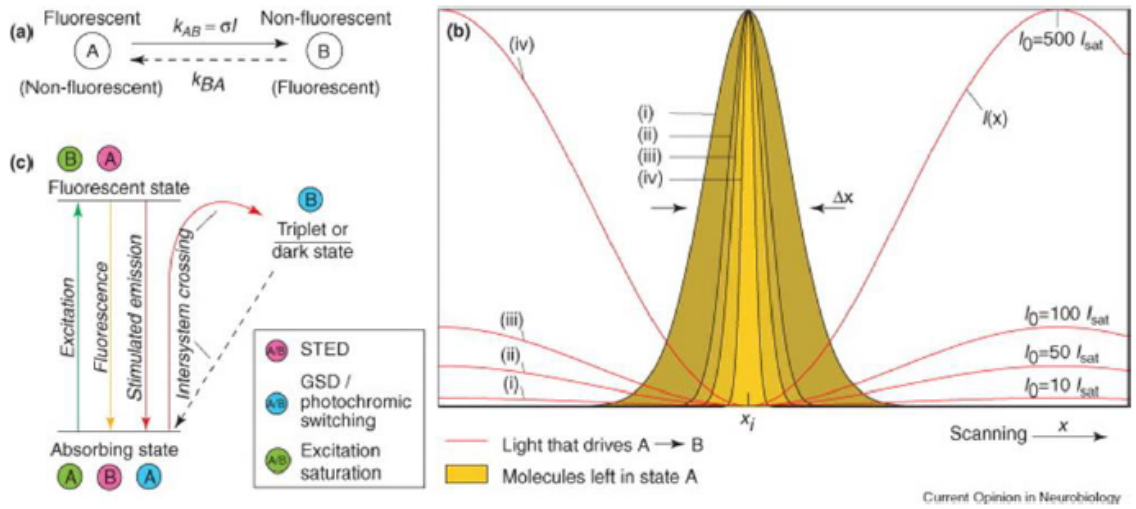

Figure 4: (Hell *et al.*, *Current Opinion in Neurobiology* 2004, 14:599–609). (a) Illustration of the fluorescence depletion principle. (b) Fluorescence density (yellow) as a function of the x-coordinate in the focal plane at STED intensities (I(x), red) with different maximal strengths (I_0). The fluorescence density (yellow) becomes sharper with increasing I_0.

Confocal

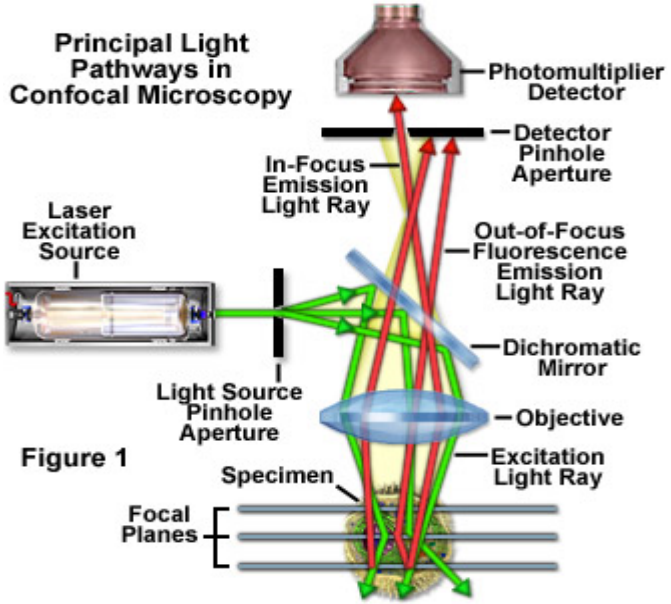

Figure 1

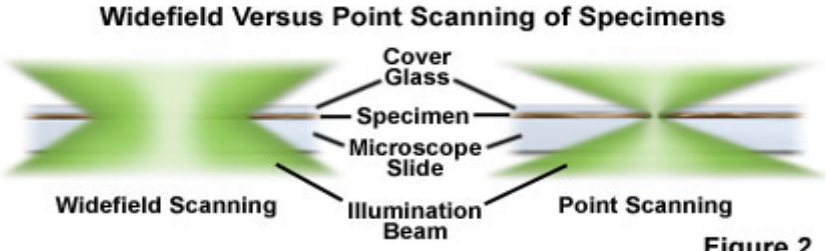

Figure 2

Tracking kinesin-driven movements with nanometre-scale precision

Jeff Gelles*, Bruce J. Schnapp† & Michael P. Sheetz*

NATURE VOL. 331 4 FEBRUARY 1988

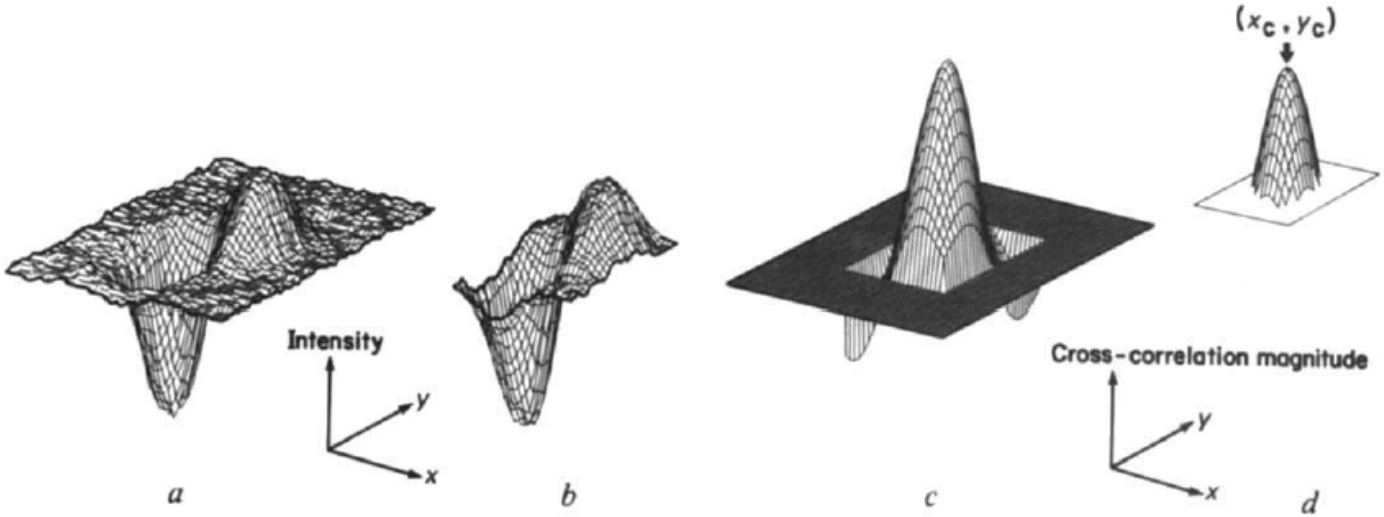

Fig. 1 Stages in the high-precision measurement of relative bead position in a video frame. *a*, Image; *b*, kernel; *c*, cross-correlation of image and kernel; *d*, centroid calculation. The illustrated sequence of computations derives positional information from the entire bead image rather than from an individual point or edge only, and thereby maximizes the precision of the measurement. *a*, A segment of a digitized video frame containing the video-enhanced DIC microscope image of a bead. The DIC image of a single bead consists of apposed bright and dark areas. The segment consists of a 49×63 rectangular matrix of integers, $\mathbf{I}(x, y)$, each of which represents the recorded light intensity at the point (x, y) in the image (x and y are integers). *b*, A 'kernel' segment $\mathbf{K}(x, y)$, consisting entirely of a single bead image. The centre of this segment is taken to be the point (0, 0). The kernel is used as a template or standard; the effect of the calculations below is to find the position in the frame segment shown in *a* for which the surrounding intensity distribution most closely matches that surrounding the centre of the kernel. When a sequence of consecutive video frames is analysed, a single kernel derived from one of the frames is used in the analysis of all of them. The x and y dimensions of the kernel are denoted α and β, respectively; for the case shown here, $\alpha = 27$ pixels and $\beta = 33$ pixels. *c*, Cross-correlation $\mathbf{C}(x, y)$ of the frame segment *a* with a scaled version of the kernel *b*. The cross-corelation calculation

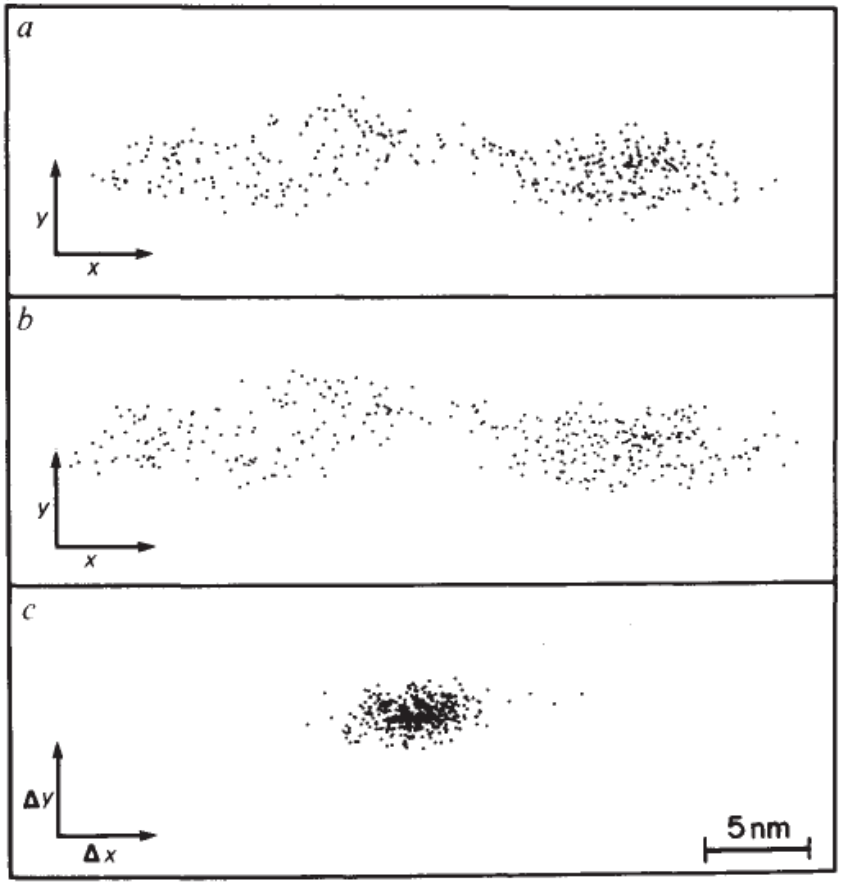
a
y
x
b
y
x
c
Δy
Δx
5 nm

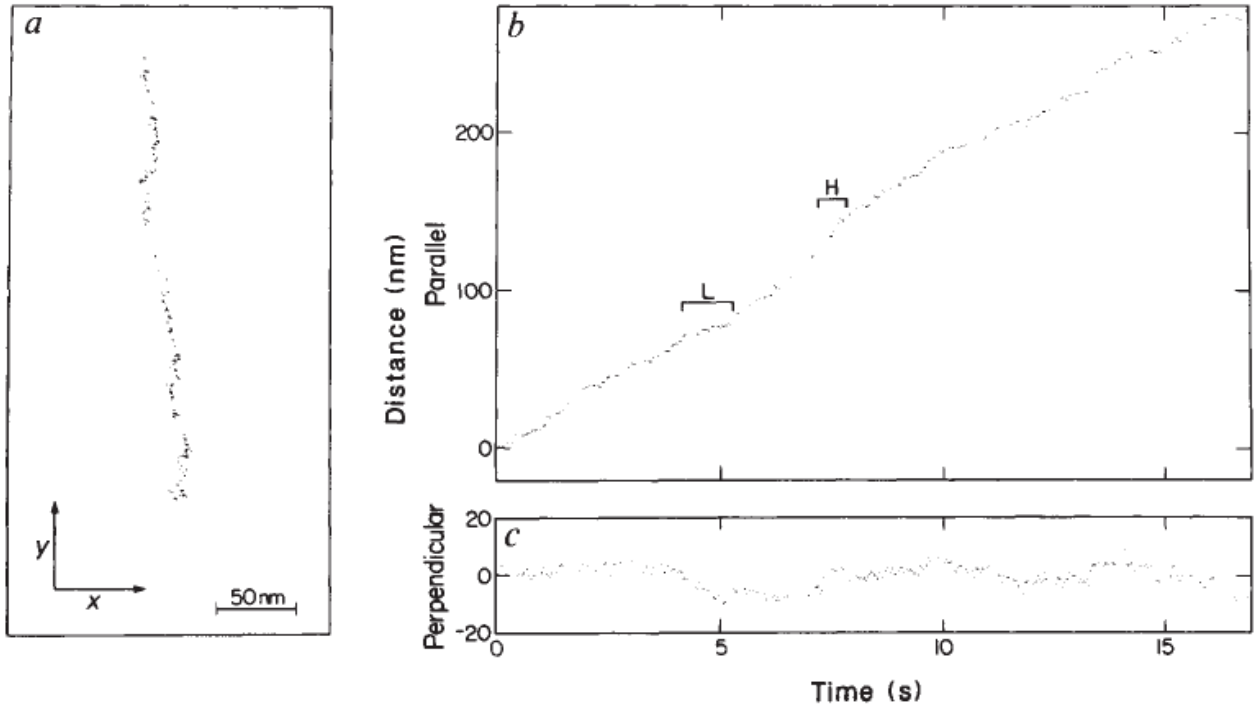

Fig. 3 Motion of a kinesin-coated bead along a microtubule in the presence of 10 μM ATP. *a*, The bead

Fig. 4 Motion of a kinesin-coated bead along a microtubule in the presence of 2.5 μM ATP. The plot shows the projection of the bead position along the microtubule axis as a function of time. The mean velocity along the microtubule axis over the period shown is 3.9 nm s^{-1} (~0.8% of maximal velocity). Forward movement in region A occurs smoothly with a mean velocity of 5.6 nm s^{-1}. Movement in region B occurs in four discrete jumps (arrows) of length 3.7 ± 1.7 nm (mean ± s.d.).

Methods. The sample was identical to that of Fig. 3, except for a lower ATP concentration (2.5 μM). The data-analysis procedure was identical to that of Fig. 3 except that microtubule orientation was determined manually from the positions of video cursors superimposed on the centre of the microtubule image at distances of 0.5 μm on either side of the microtubule segment on which the bead motion occurred.

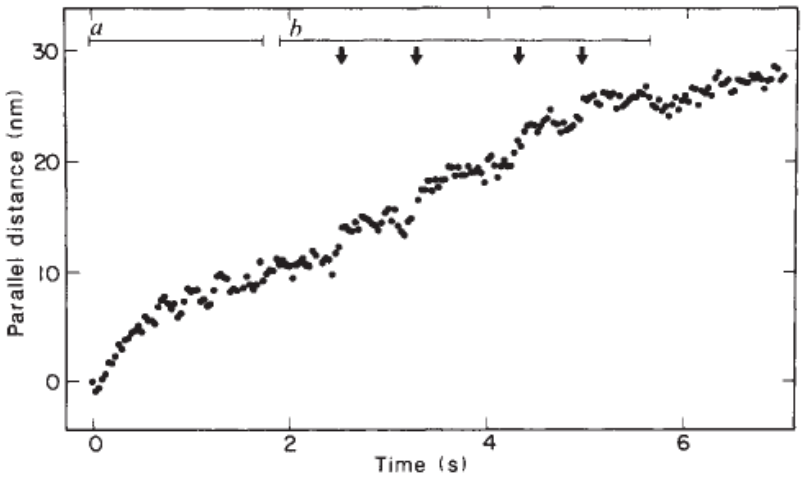

Localization

$$I(x, y) = I_{\text{background}} + A. \exp\left\{-1/2\left[\left(\frac{x - x_0}{s_x}\right)^2 + \left(\frac{y - y_0}{s_y}\right)^2\right]\right\},$$

$$\sigma^{\mu}_{x,y} = \sqrt{\frac{s^2_{x,y}}{N_{\text{photons}}} + \frac{a^2}{12.N_{\text{photons}}} + \frac{8.\pi.s^4_{x,y}.b^2}{a^2.N_{\text{photons}}}},$$

Fluorescence Imaging with One Nanometer Accuracy (FIONA)

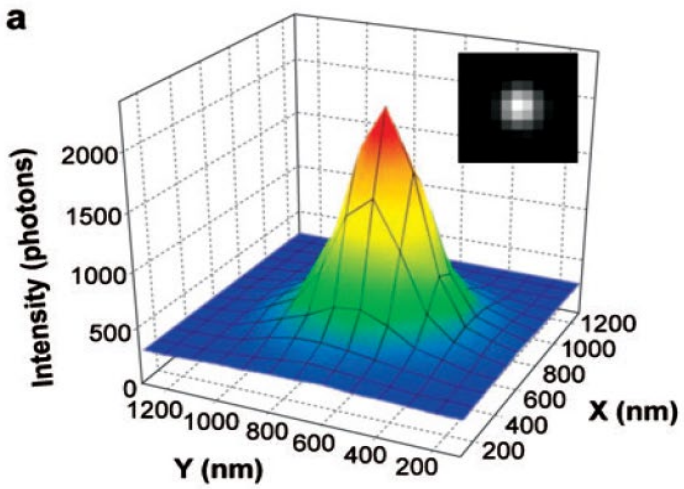

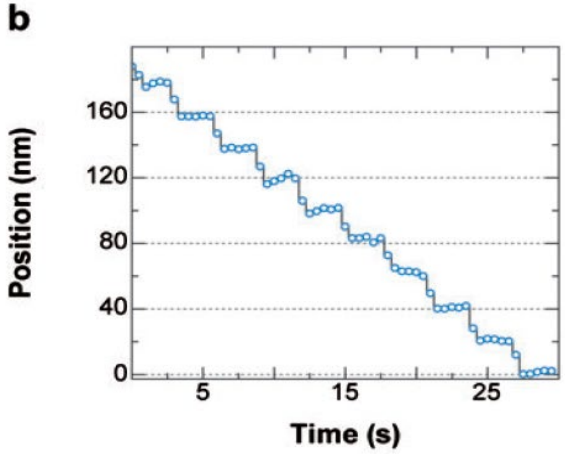

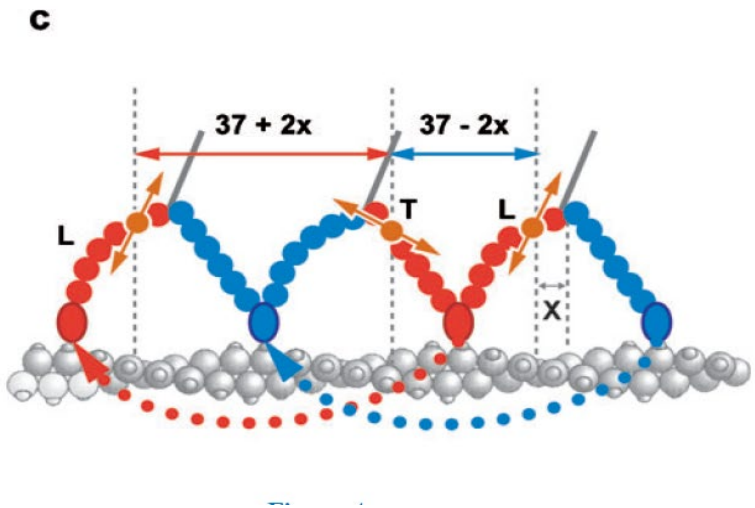

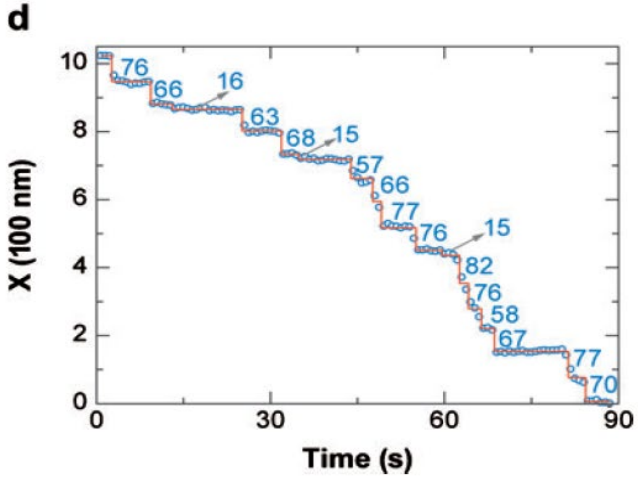

Fluorescence Imaging with One-Nanometer Accuracy (FIONA)

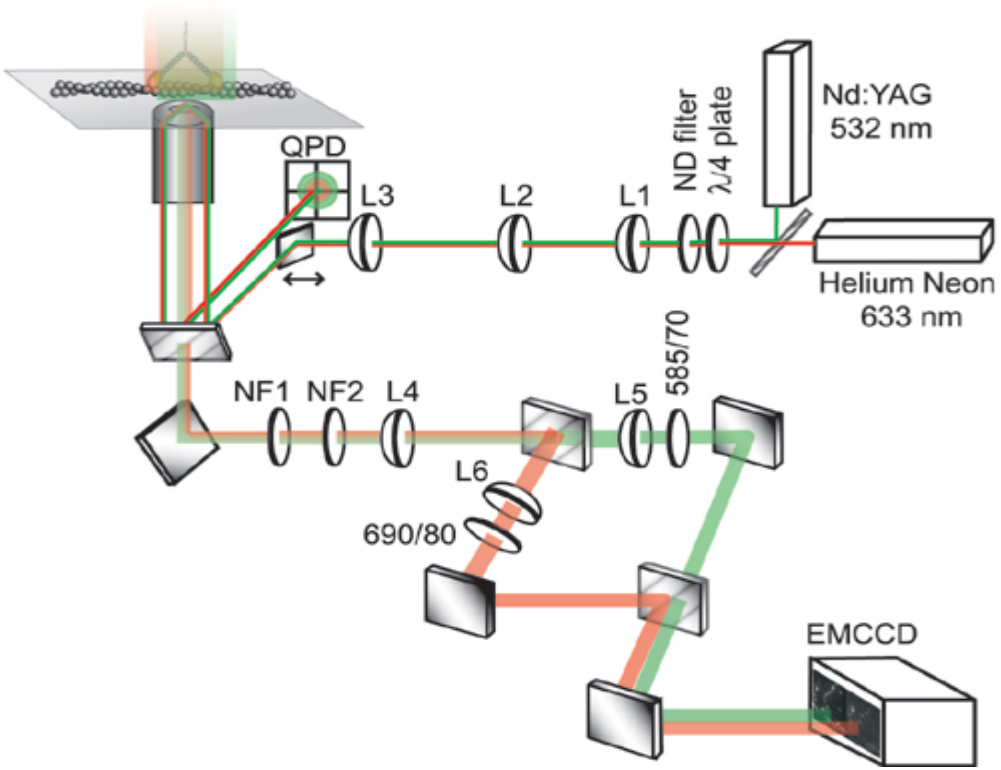

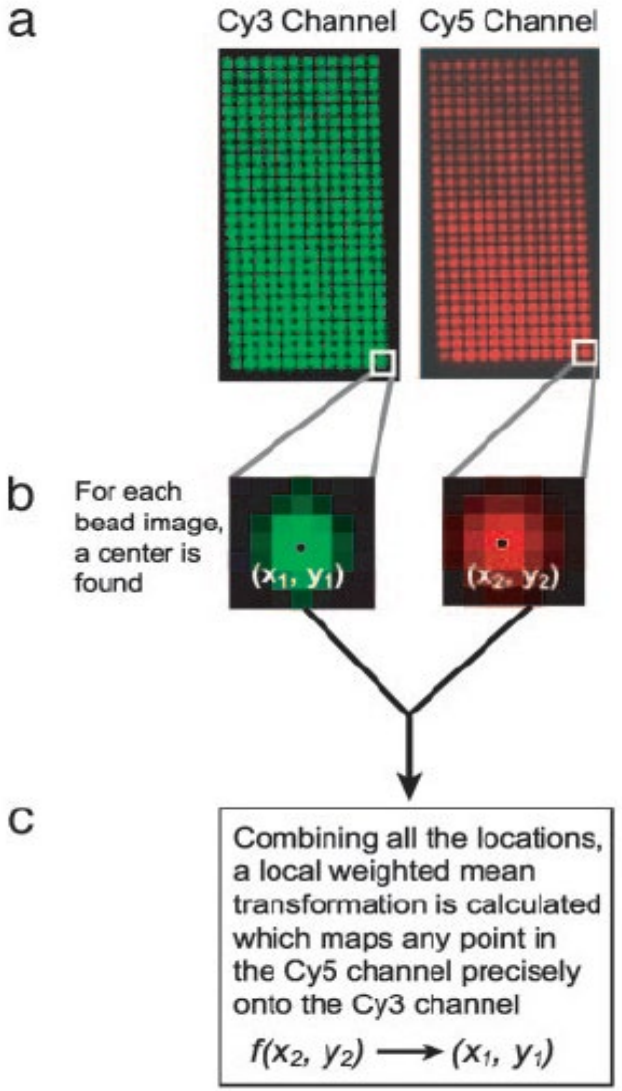

$$f(x, y) = z_0 + A \exp\left(\frac{1}{2}\left[\left(\frac{x - \mu_x}{\sigma_x}\right)^2 + \left(\frac{y - \mu_y}{\sigma_y}\right)^2\right]\right)$$

$$\sigma_\mu = \sqrt{(\sigma_x^2 + \sigma_y^2)} \Big/ \sqrt{N_\gamma - 1}.$$

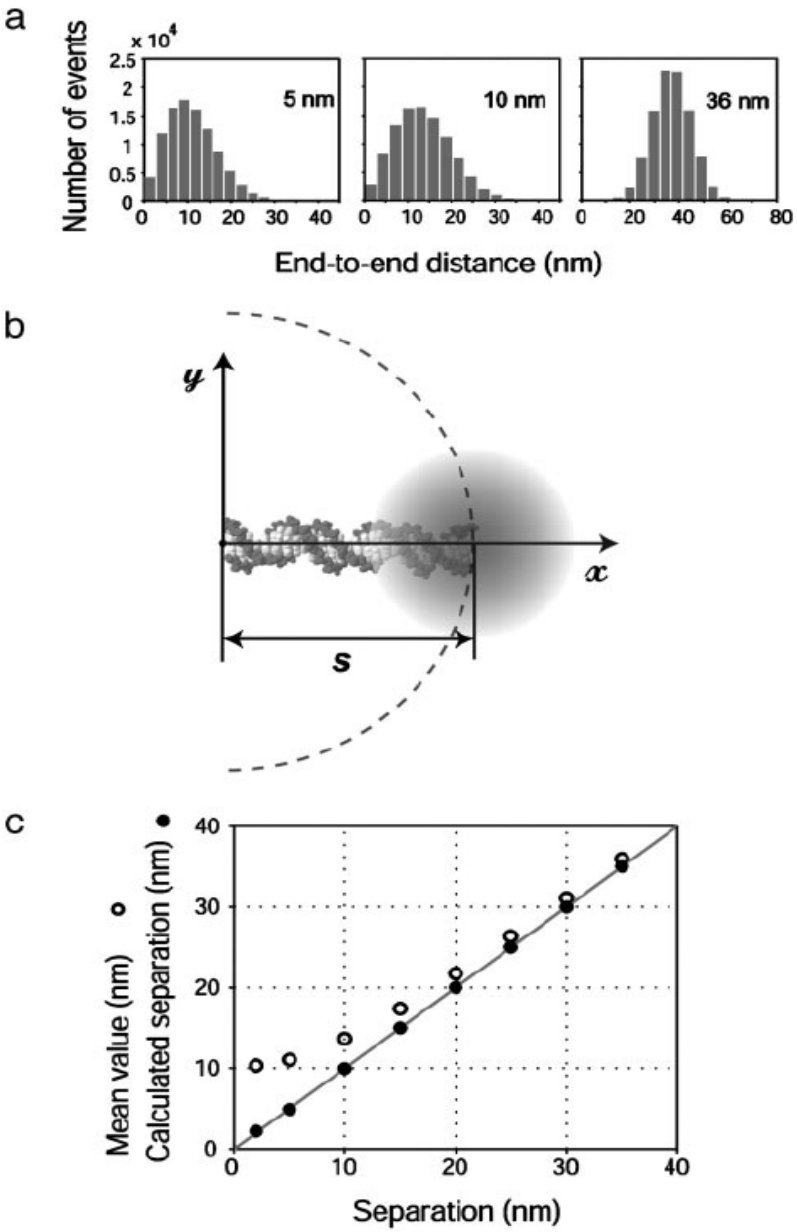

Fig. 2. Determining the accurate end-to-end distance from the skewed distribution of distance measurements. (*a*) The distance probability distribution was calculated by means of Monte Carlo simulations. (*b*) The skew in the histograms toward large values can be understood from a geometric argument. If one end of the DNA molecule is measured to reside at the origin, then only points lying on the circumference of a circle with radius *s* and origin (0, 0) will yield the true end-to-end distance. It is more likely that a point will lie outside of the dashed-line semicircle than inside it, which gives the distance distribution a long tail. (*c*) Despite the non-Gaussian nature of the distance distribution, the end-to-end separation can be calculated using the geometric mean, variance, and localization errors.

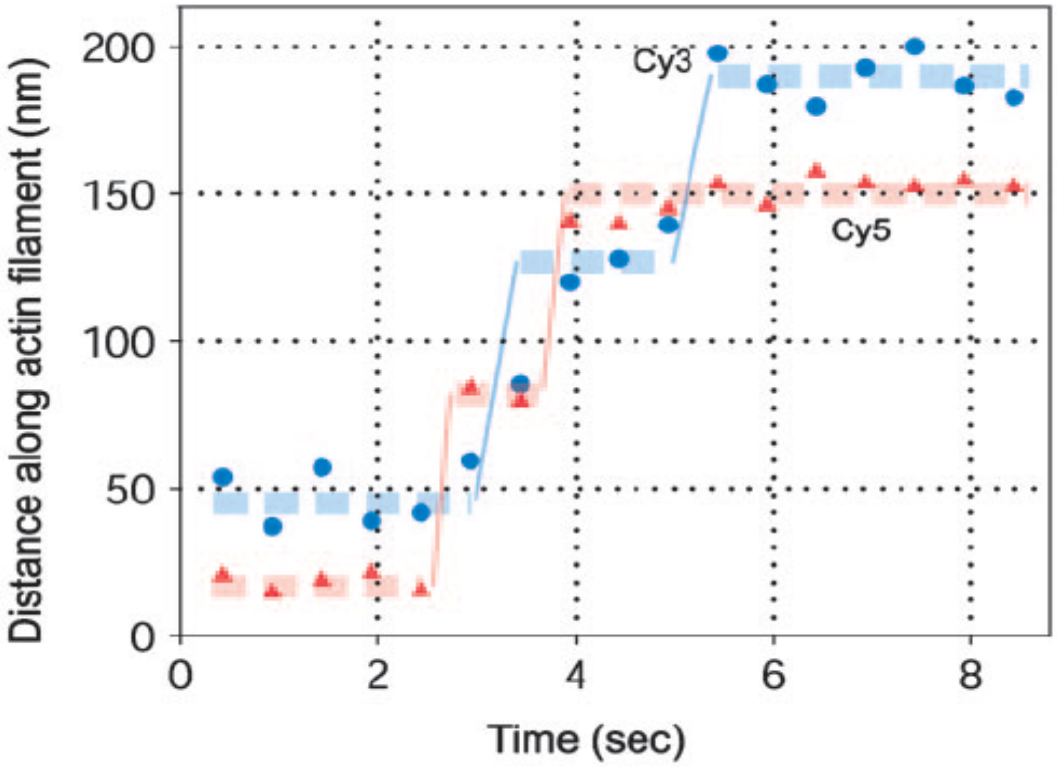

Fig. 4. Time trace of a differentially labeled myosin V molecule walking along an actin filament. The labels (Cy3 and Cy5) are covalently attached to calmodulins that were exchanged onto the myosin V molecule. In this trace, both of the fluorescent probe's locations are taking 72-nm steps, indicating that the calmodulins were exchanged close to the motor domain. The alternating positions of the probes provide a direct observation of myosin V's hand-over-hand walking mechanism.

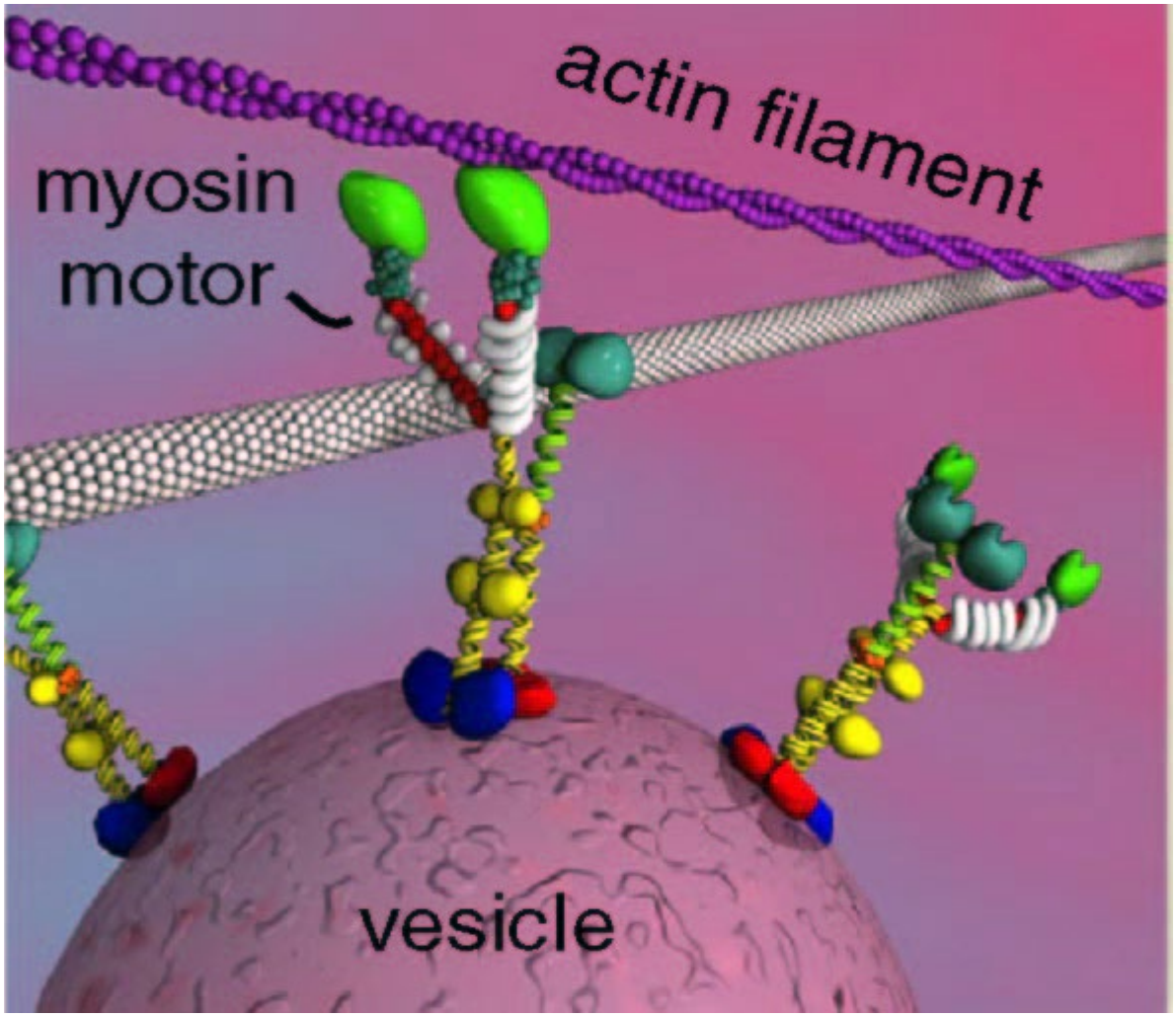
actin filament
myosin
motor
vesicle

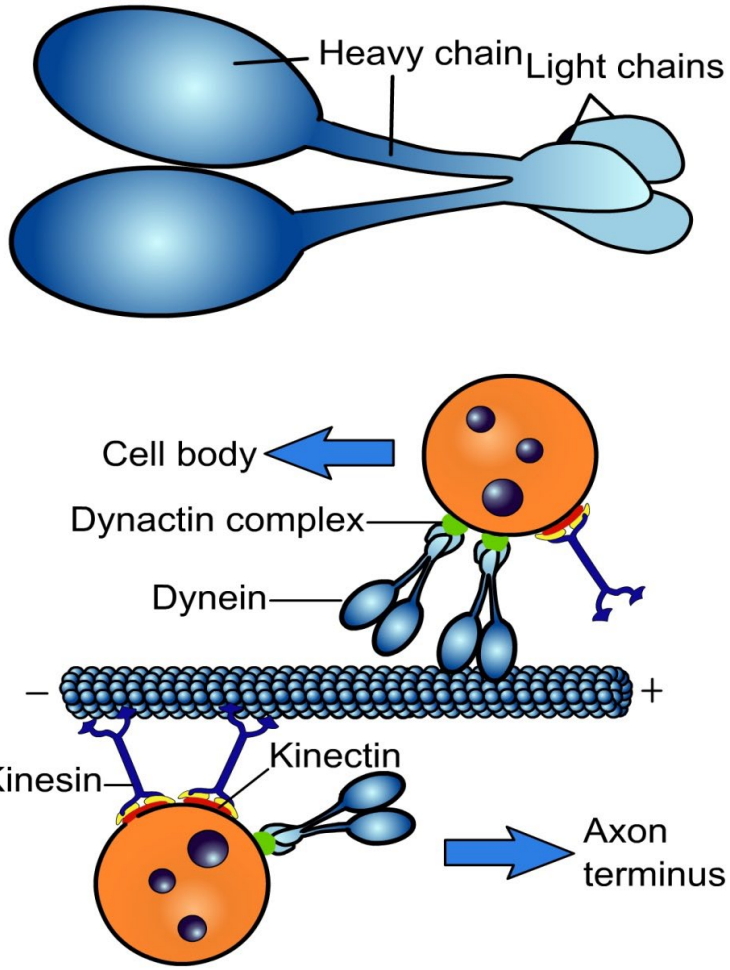
Heavy chain
Light chains
Cell body
Dynactin complex
Dynein
–
+
Kinesin
Kinectin
Axon
terminus

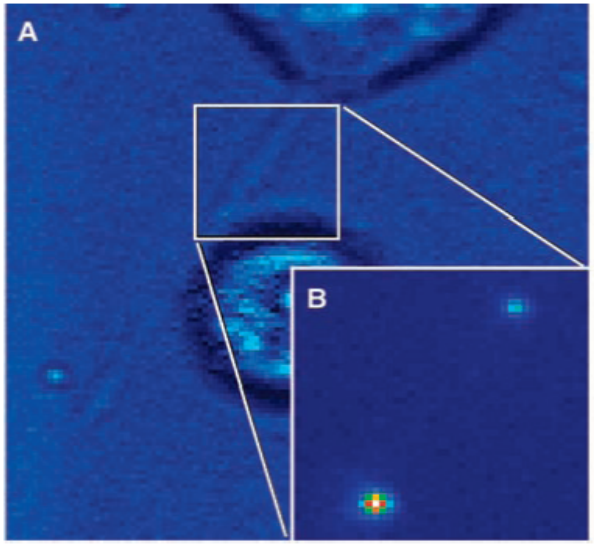

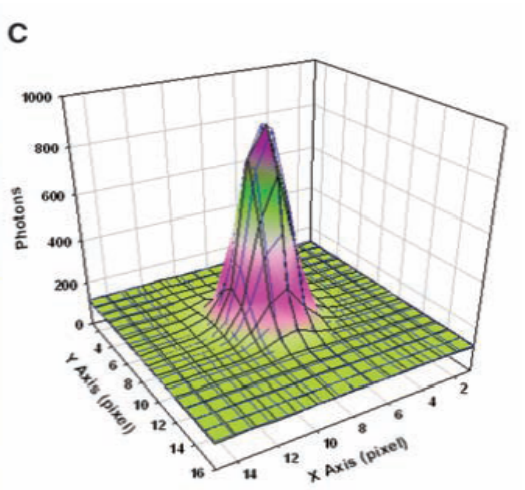

Fig. 1. (A) Bright-field image of a cytochalasin-D–treated S2 cell with a thin process. (B) Fluorescence image of the GFP-labeled peroxisomes within the process. (C) Fluorescence image of a peroxisome can be fit to a two-dimensional Gaussian (correlation coefficient $r^2 = 0.992$), enabling the center to be determined to 1.5 nm within 1.1 ms.

Kinesin and Dynein Move a Peroxisome in Vivo: A Tug-of-War or Coordinated Movement?

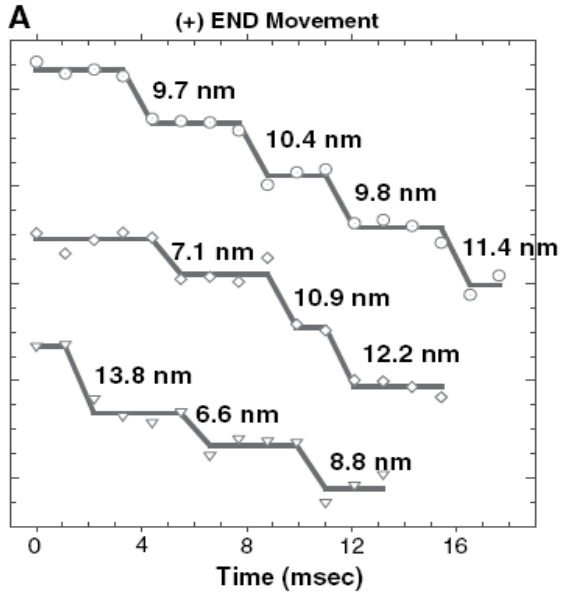

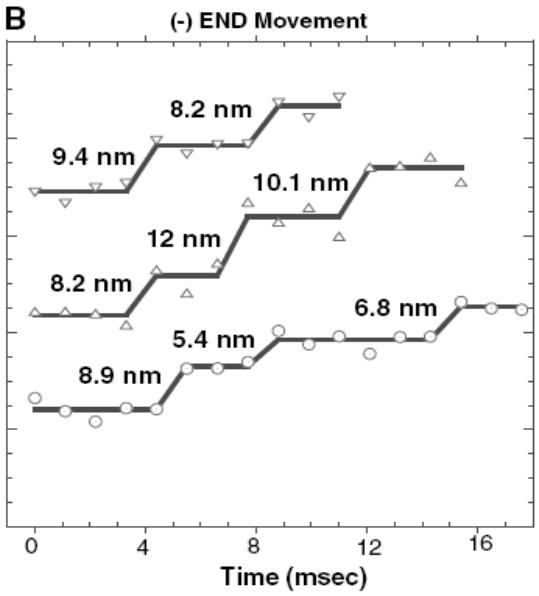

SCIENCE VOL 308 3 JUNE 2005

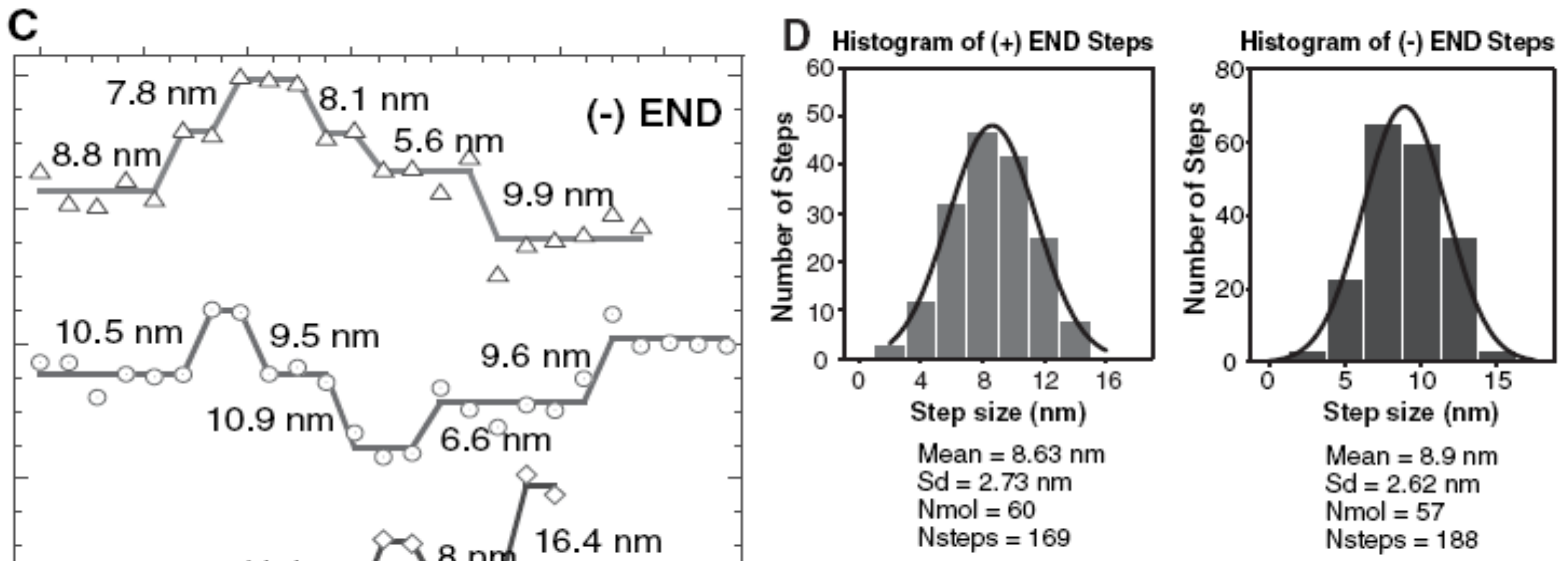

Fig. 2. Step-by-step movement of peroxisomes carried by (A) a single kinesin, (B) a single dynein, and (C) a coordination of kinesin and dynein. (D) Histograms of the individual steps of anterograde (kinesin) and retrograde (dynein) movement. A pairwise displacement of kinesin and dynein, showing the multiples of 8-nm displacement, is shown in fig. S6.

Single-molecule High-Resolution Colocalization (SHREC)

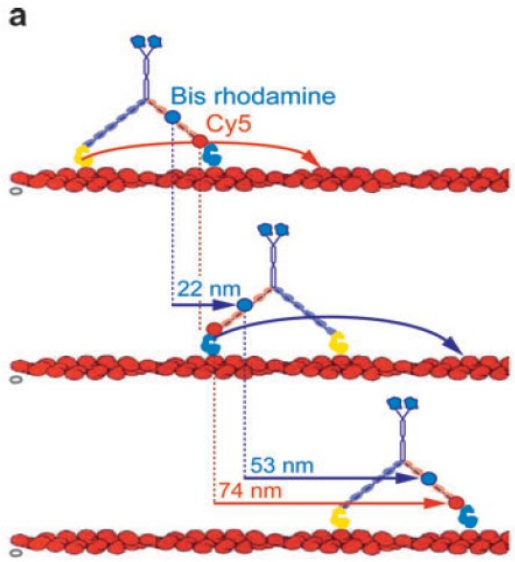

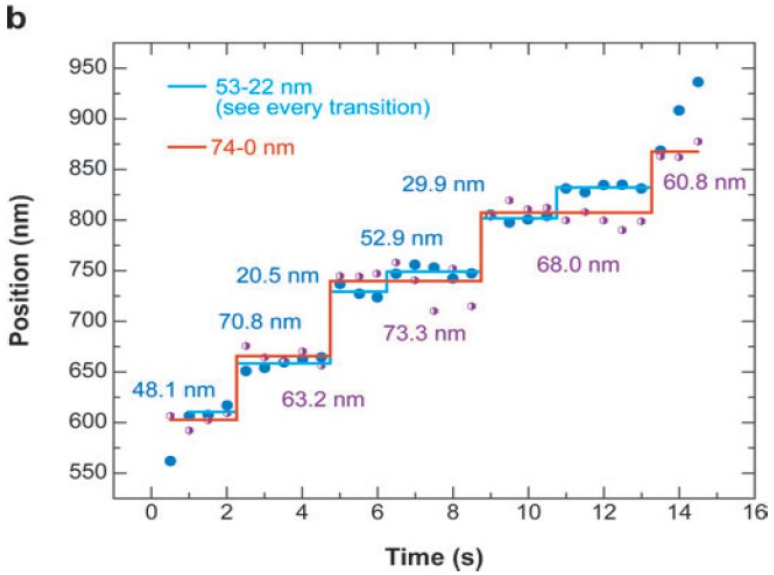

Proposed method for molecular optical imaging

E. Betzig

Here an alternative approach is proposed in which multiple discrete features within the same focal volume are spatially resolved in two steps (see Fig. 1). First, each feature is identified and isolated through one or more distinguishing optical characteristics. Second, each feature is localized; that is, its spatial coordinates are determined, on a scale that is small compared with the focal volume, either by measurement of the center of the point-spread function (PSF) associated with each feature[2] or by application of a spatial gradient,[3,4] as discussed below. The complete set of coordinates for all features can then be used to reconstruct the final image in which the relative positions of the features are shown.

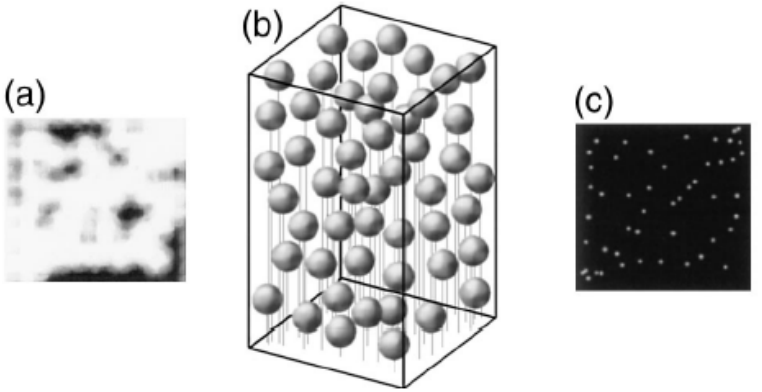

Fig. 1. (a) Field of discrete features as conventionally imaged in m spatial dimensions with a broad PSF. (b) Same features after isolation in $m + n$ dimensions on the basis of n distinguishing optical characteristics. (c) Final image reconstructed at resolution $\delta\mathbf{x}$ given by the uncertainty in the measured position of each isolated feature. In general, $|\delta\mathbf{x}| \ll$ PSF.

Photoactivation localization microscopy (PALM)

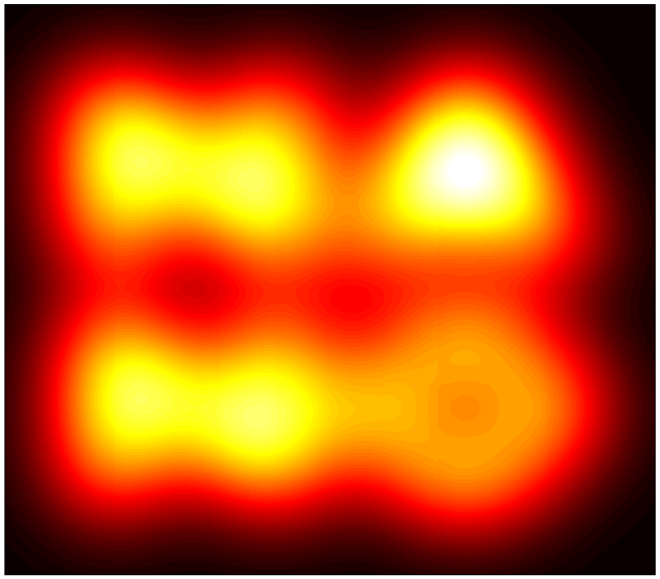

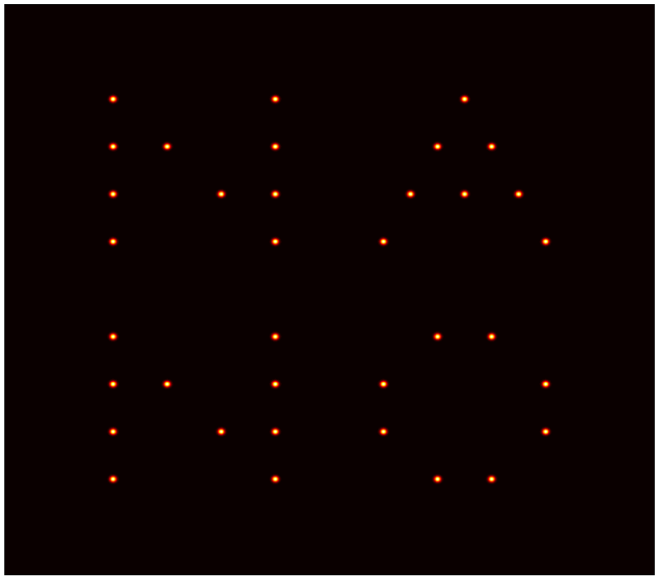

Diffraction-limited system:

Lateral resolution $\Delta xy \approx 0.61\,\lambda$ / N.A.
$\approx$ 200 nm

Axis resolution $\Delta z \approx 2\lambda$ / N.A.^{2}
$\approx$ 450 nm

Mean-squared position error:

$$\left(\sigma_{x,y}^2\right)_m \approx \frac{s^2 + a^2/12}{N_m} + \frac{4\sqrt{\pi}s^3 b_m^2}{aN_m^2}$$

s is the standard deviation of the PSF.
a is the pixel size in the image
N_m is the total number of photons measured from molecule *m*
b_m is the number of background photons collected in the fitting window

Russell E. Thompson, Daniel R. Larson, and Watt W. Webb, **Biophysical Journal** 82, 2775 (2002).
Eric Betzig, et al., **Science** 313, 1642 (2006).

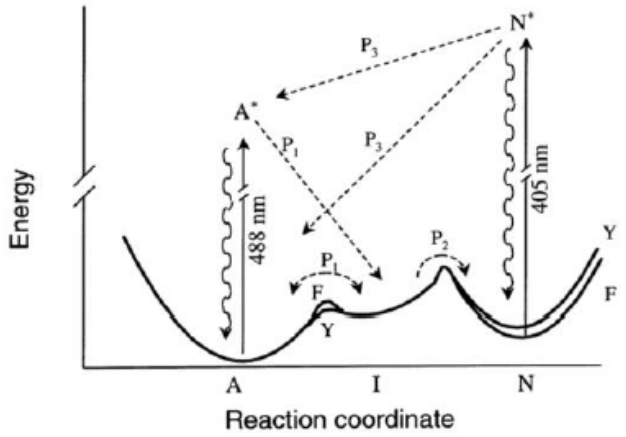

Figure 7: (Dickson *et al.*, 1997, *Nature* 388, 355-358). GFP in state A is excited to A* and returns to A upon photon emission. When I is reached from A, there is no fluorescence until I spontaneously moves to A: blinking. When I moves to N, there is no fluorescence until N is activated to N* by 405 nm excitation and GFP returns to A.